DYNAMIC FAILURE MECHANICS INVESTIGATION ON THE ADVANCED

MATERIALS WITH INTERFACES

By

PING WANG

Dissertation

Submitted to the Faculty of the

Graduate School of Vanderbilt University

in partial fulfillment of the requirements

for the degree of

DOCTOR OF PHILOSOPHY

in

Civil Engineering

December, 2008

Nashville, Tennessee

Approved:

Professor L. Roy Xu

Professor P. K. Basu

Professor Sankaran Mahadevan

Prefessor Dechao Zheng

To my beloved family, infinitely supportive

ACKNOWLEDGEMENT

The completion of this work would not have been possible without the financial support of the Naval Research Office and the National Science Foundation. I am especially indebted to Dr. L. Roy Xu, my adviser and chairman of my dissertation committee, who has been supportive of my research in Vanderbilt and provided me valuable guidances.

I am grateful to all of my committee members who have worked with me throughout the dissertation research process. Each of the members has provided me extensive personal and professional guidance and taught me a great deal about scientific research and life in general. I am also grateful for support provided by the department of Civil and Environmental Engineering.

Nobody has been more supportive of me in the pursuit of this degree than my family. I would like to thank my family for their unconditional love and support in every aspect of my life.

TABLE OF CONTENTS

LIST OF TABLES

LIST OF FIGURES

CHAPTER I

INTRODUCTION

Composite materials have many useful properties, such as lightweight, high strength, low thermal expansion, and excellent resistance to environment and corrosion. Applications of composite materials have been found in several engineering fields such as new Boeing 787 airplane. Because composite materials in aircraft structural components have allowed the design of lighter structures with better fatigue behavior compared to metal structures. However composite laminates show a poor response to impact loading, even at quite mild intensity, such as a bird hitting the structure, dropping of tools during fabrication. As a matter fact, this kind of impacts led to matrix cracking and delaminations which can considerably reduce the structural load carrying capabilities especially under compressive load. On the other hand, the ability of a structure to withstand impact by foreign objects is a necessary requirement for structural materials.

In Figure 1.1(a), impact failure on model sandwich structures was illustrated (Xu and Rosakis, 2002). Under impact loading, failure mode transitions between the inter-layer cracks and the intra-layer cracks are very complicated. When a crack propagates towards an interface in brittle solids, there may exist three situations (see Figure 1.1(b)). The first one is that the crack kinks/deflects out of its original plane and propagates along the interface; in the second situation the crack penetrates the interface

and continues to propagate into the other side within its original plane; and the third case

is that interface debonding occurs before the main crack reaches the interface. All these

phenomena were observed in recent experiments by Xu, et. al., (2003), and Xu and

Rosakis (2003).

(a)

(1) Crack deflection

$$\frac{G_{sk}}{G_I} \geq \frac{\Gamma_c^{IT}}{\Gamma_{IC}^{MA}}$$

(2) Crack penetration

$$\frac{G_{sk}}{G_I} < \frac{\Gamma_c^{IT}}{\Gamma_{IC}^{MA}}$$

(b)

(3) Debonding before deflection

?
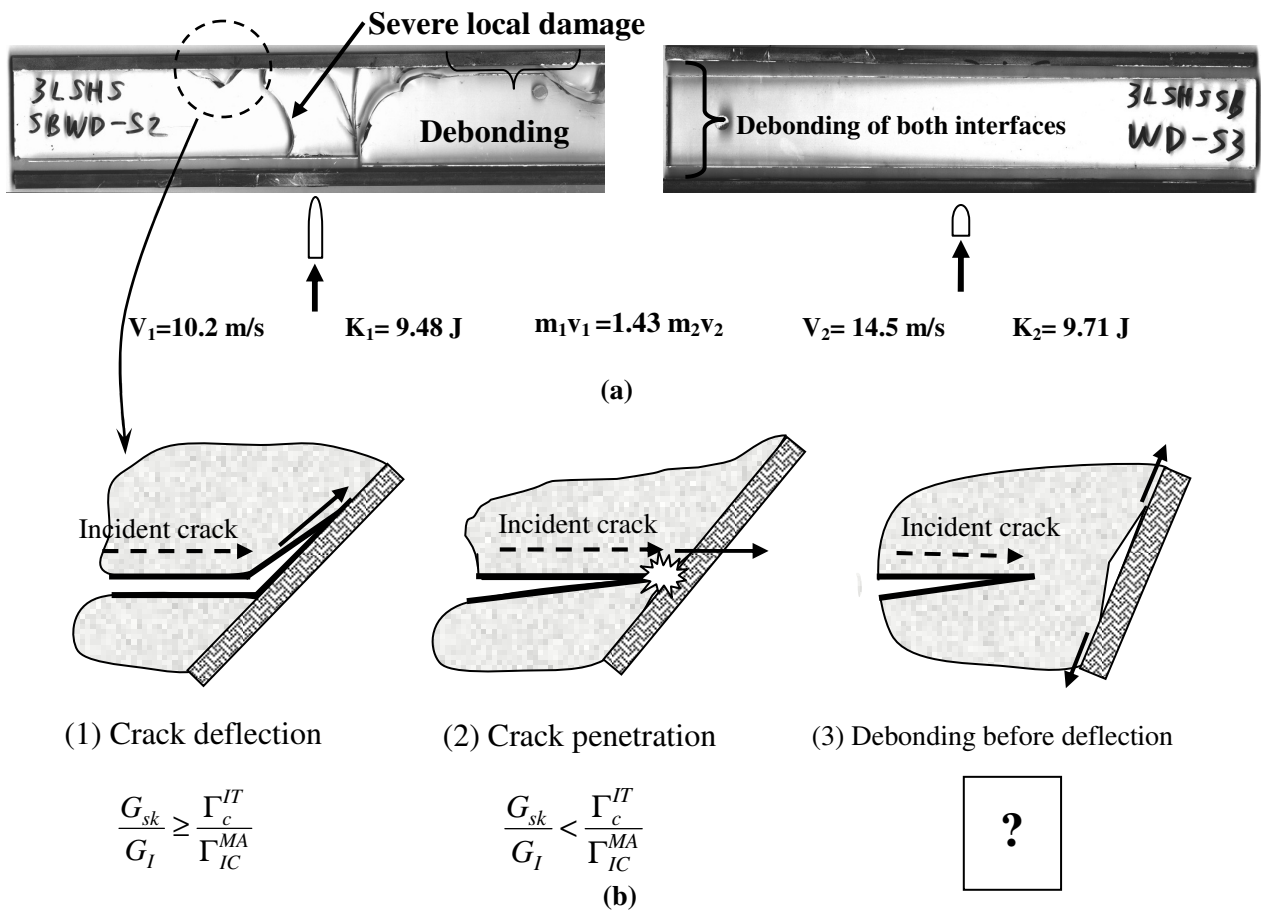
Figure 1.1, (a) Post-impact failure patterns of two identical sandwich specimens (Xu, 2002); (b) Common dynamic failure modes and corresponding criteria when a crack encountering an interface.

In the literature, most of the effort has been put to the first two cases-crack deflection

and crack penetration (He and Hutchinson, 1989; Hutchinson and Suo, 1992; Gupta et al.,

1992). For static loading, one successful criterion has been developed to identify the

competition of crack deflection/penetration (Evans and Zok, 1994; Martinez and Gupta,

1994; Ahn et al., 1998; Martin et al., 1998; Qin and Zhang, 2000). It is stated that the

critical conditions governing the competition of these two fracture modes are: $\frac{G_{sk}}{G_I} < \frac{\Gamma_c^{IT}}{\Gamma_{IC}^{MA}}$

for the continuous crack propagation along its original crack plane and $\frac{G_{sk}}{G_I} \geq \frac{\Gamma_c^{IT}}{\Gamma_{IC}^{MA}}$ for the

crack kinking at the interface, where G_{sk} and G_I are energy release rates of the putative

kinked crack and penetrated crack, respectively; Γ_c^{IT} and Γ_{IC}^{MA} are fracture toughnesses of

the interface and matrix materials, respectively. For dynamic crack propagation, Xu et al.

(2003) examined the deflection/penetration behavior of dynamic mode-I cracks

propagating at various speeds towards inclined weak interfaces of various strengths in

otherwise homogeneous isotropic plates. However, for dynamic crack kinking, no

analytical results are given to evaluate the relationship of dynamic fracture mechanics

parameters between the incident crack and the kinked interfacial crack.

On the other hand, there are some cases in which the energy-based criterion

mentioned above fails to predict interfacial deflection (Warrier et al., 1997; Kovar et al.,

1997) and interfacial penetration (Ahn et al., 1998). To explain such discrepancies,

various reasons have been proposed, among them, a different mechanism of crack

deflection was proposed (Cook and Gordon, 1964): before the main crack encounters the

interface, the interface failure occurs and the crack deflection results from linking between the interfacial crack and the primary crack. This mechanism has been experimentally evidenced and analyzed by many researchers (Lee et al., 1996; Warrier et al., 1997; Majumdar et al., 1998; Pagano, 1998; Leguillon et al., 2000; Baber et al., 2002). In previous dynamic fracture tests, Xu et al. (2003) also observed the dynamic equivalence of this phenomenon. However, when and where the interface debonding occurs ahead of a primary crack analytically remains unsolved.

In above analyses, accurate determination of interfacial properties is extremely important to study impact damage of dissimilar materials (Xu and Rosakis, 2002), especially for interface debonding ahead of an incident crack (see Figure 1.1(b)). Meanwhile, intrinsic interfacial strengths are key inputs for modern numerical simulations. However, macro-scale interfacial strength measurement is still a major challenge due to the free edge stress singularities at the dissimilar material interfaces (Reedy and Guess, 1993; Tandon et al., 1999; Akisanya and Meng, 2003). To accurately measure and improve mechanical properties of dissimilar material interfaces, the first task is to remove the free edge stress singularities. Xu et al. (2004a, b) developed a novel convex interfacial joint which can effectively eliminate the free edge stress singularities and dramatically improve the load capacity as shown in Figure 1.2. However, they only statically tested planar specimens, and the stress singularity along the thickness direction still exists. Further 3-D analysis and dynamic response of the novel design needs to be conducted for a complete understanding.
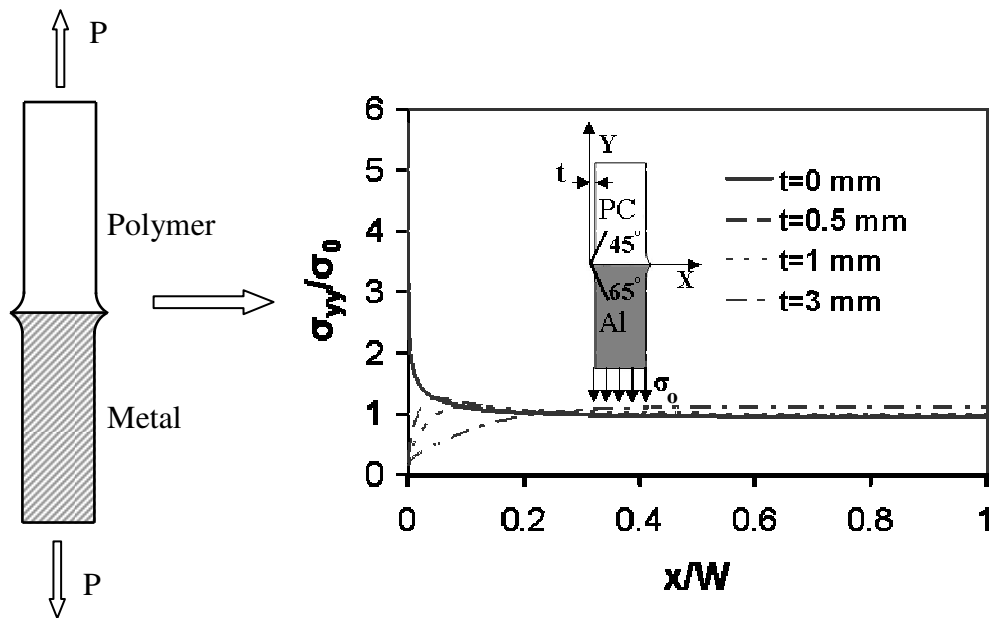
Figure 1.2, Novel joint design and stress distribution along the interface
(Xu et al., 2004 a, b).

Based on the above discussions, the layout of this study can be stated as follows:

1. Dynamic fracture mechanics analysis of failure mode transitions along weak interfaces in elastic solids; which was published by *Engineering Fracture Mechanics* in 2006

2. Analysis of interface debonding induced by a dynamic incident crack; which was published by *International Journal of Solids and Structures* in 2006

and 3. Intrinsic interfacial strength measurement of dissimilar material joints using a novel joint design; which was published by *Mechanics of Materials* in 2006

CHAPTER II

DYNAMIC FRACTURE MECHANICS ANALYSIS OF FAILURE MODE
TRANSITIONS ALONG WEAKENED INTERFACES IN ELASTIC SOLIDS

Introduction

When cracks propagate in homogenous and brittle solids, they can only do so under

locally mode-I conditions and at sub-Rayleigh wave speeds typically below the crack

branching speed (Freund, 1990; Gao, 1993; Broberg, 1999). Even if the applied loading

is asymmetric, the dynamically growing crack will curve and follow the path that will

result in locally opening (mode-I) conditions. The situation is entirely different if a crack

is constrained to propagate along a weak preferred path in an otherwise homogenous

solid. In this case and depending on the bond strength, the weak crack path or bond often

traps the crack, suppresses any tendency of branching or kinking out of the weak plane

and permits very fast crack growth much beyond the speeds observable in monolithic

solids (Rosakis et al., 1999; Ravi-Chandar et al., 2000). Indeed, when mode-I cracks

propagate in both isotropic and orthotropic solids containing weak crack paths

(Washabough and Knauss, 1994), they can reach speeds as high as the Rayleigh wave

speed of the solid. On the other hand, when mode-II cracks are made to propagate along

such weak paths, they tend to go at even faster speeds that are clearly within the

intersonic regime of the solid (Rosakis et al., 1999; Gao et al., 1999). Although the

extreme mode-I and mode-II cases have recently been studied experimentally and

theoretically, very little is known about the dynamic mixed-mode crack growth along weak paths, a situation that has only recently been analyzed by Geubelle and Kubair (2001) about the transition of an incident dynamic mode-I crack into a mixed-mode crack as it encounters a weak plane or interface. Recently, Xu et al. (2003) examined the incidence of dynamically growing cracks at inclined interfaces of various strengths. Interesting phenomena on mixed-mode crack growth along an interface were observed. They tested weakly bonded systems composed of identical constituents so that the resulting material remains constitutively homogenous. However, the existence of a weak bond (bond of lower fracture toughness) made this material inhomogeneous regarding its fracture resistance behavior. Therefore, the complication of the stiffness property and wave speed mismatch across the interface was avoided while retaining the essential properties of a weak interface or bond whose strength could be experimentally varied and analytically modeled.

As shown in Figure 2.1(a), a novel wedge-loaded Homalite-100 plate is employed to produce a single, straight dynamic crack propagating towards the weakly bonded, inclined interface. The specimen sizes were large enough such that the major stress waves reflected from free boundaries entered the field of view, 20 μs after the incident crack reached the interface. Inclined interfaces included several characteristic interfacial angles of 10, 30, 45, 60 and 90 degrees. To provide different interfacial strengths and fracture toughnesses, two kinds of adhesives were used to bond the interfaces and to create weak interfaces of toughness less than that of monolithic Homalite (brittle polymer with

well-known dynamic fracture behavior, see Kobayashi and Mall, 1978). Figure 2.1 shows

a series of dynamic photoelasticity images of the crack deflection process at a weak

interface (interfacial angle 30 degrees). The vertical line appearing in every image is the

camera streak line, which was used for positioning and reference purposes. Another

inclined thin line reveals the position of the interface.   A dark circular spot, at the

left-hand bottom, is a scaling mark.   In Figure 2.1(b), a dynamic mode-I crack (featuring

symmetric fringe patterns) is seen to propagate towards the interface. Around 164 μs after

impact, we notice that the crack tip fringe pattern has already lost some of its symmetry.

Around 170 μs (Figure 2.1(d)), this mode-I incident crack has already transitioned into a

mixed-mode crack at the interface, whose fringe pattern at the crack tip is clearly

asymmetric with respect to its propagation direction. In fact, a close look at this pattern

reveals that its line of symmetry was still parallel to the horizontal line although the crack

propagates along the inclined weak interface. Also, the caustic (or shadow spot

surrounding the crack tip, see Kalthoff, 1983; Guduru et al, 2001) size at the crack tip is

significantly reduced in comparison to the caustic sizes in Figures 2.1(b) and (c). As the

interfacial crack quickly moved out of the field of view, the horizontal crack faces of the

original mode-I crack were seen to experience clear frictional contact as evidenced from

the Figure 2.1(f). The abruptness of the transition behavior between a mode-I incident

crack and a mixed-mode interfacial crack could be graphically witnessed by the

impressive jump in crack speeds across the interface. Figure 2.2(a) shows the total crack

length history as the incident mode-I crack developed and transitioned into a mixed-mode

interfacial crack. The interfacial crack length used in Figure 2.2(a) is defined as the total instantaneous arc length measured along the non-straight crack path. Differentiation of the crack length record furnished the tangential crack tip speeds before and after crack deflection. Since the differentiation process is based on a three-point-fitting of the crack length history, the exact crack speed at the interface could not be obtained. Before crack deflection, the crack tip speed was approximately 400 m/s, which was a speed very close to the branching speed of Homalite-100. After crack deflection, the speed jumped to as much as 800-1000 m/s and then decreased as it propagated further along the interface.

However, other dynamic fracture mechanics parameters such as the dynamic stress intensity factors and the mode mixity of the kinked interfacial crack were not further analyzed in these experiments. In this investigation, we will fit the isochromatic fringe patterns around the incident dynamic crack to obtain the dynamic stress intensity factors, and the non-singular T stress. Then, the relation of the stress intensity factors for the kinked crack and the incident crack will be developed. As validation, experimental fringe patterns of the kinked interface crack will be directly compared to the theoretical patterns predicted using dynamic fracture mechanics theory. Moreover, the change of important mode-mixity of the kinked crack will be analyzed. Such results will be very useful to investigate complicated dynamic failure mode transition in bi-materials and composite materials such as the transition of matrix cracking and delamination (Liu et al., 1993; Deng, 1994; Singh and Shukla, 1996; Siegmund et al., 1997; Arata et al., 2000; Xu and Rosakis, 2002).
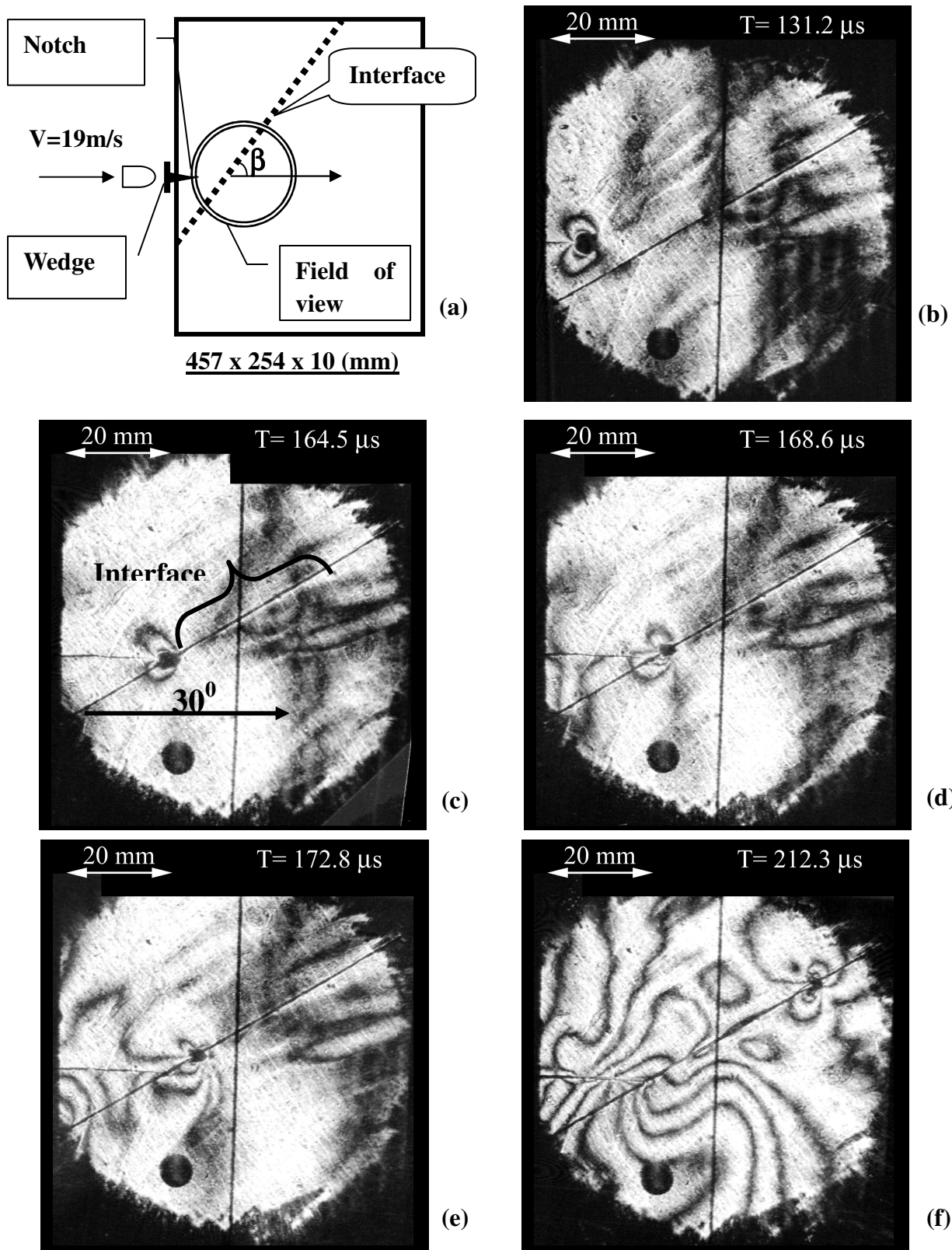
Figure 2.1, Dynamic crack deflection process at a weak interface (interfacial angle 30 degrees, from Xu, Huang and Rosakis, 2003).

cdp30i384-3

(a)

Plot: Crack length (mm) vs Time (microseconds)
- ◆ Mode I incident crack
- ☐ Mixed-mode interfacial crack

cdp30i384-3

(b)

Plot: Crack speed (m/s) vs Time (microseconds)
- ◆ mode I incident crack
- ☐ mixed-mode interfacial
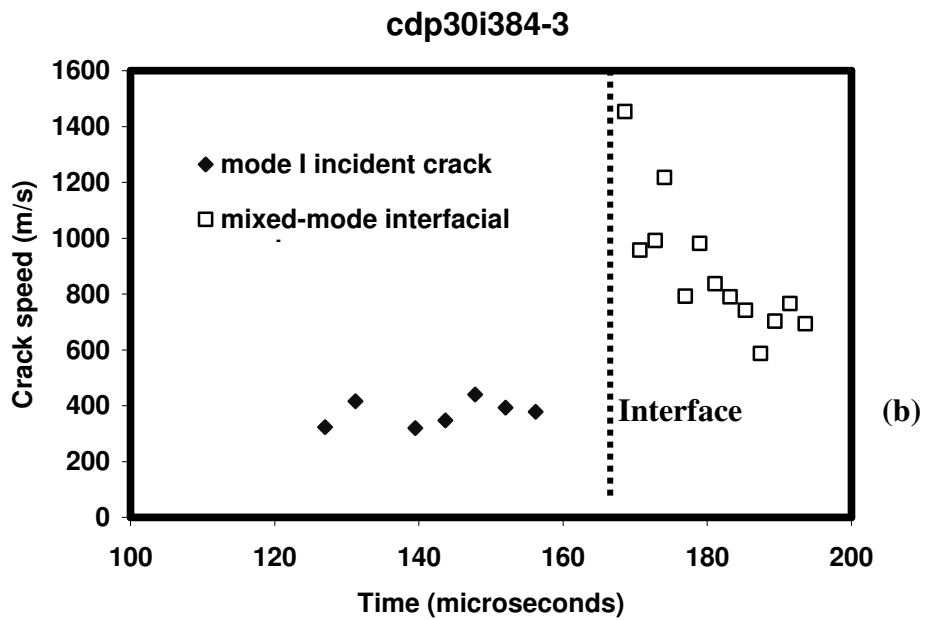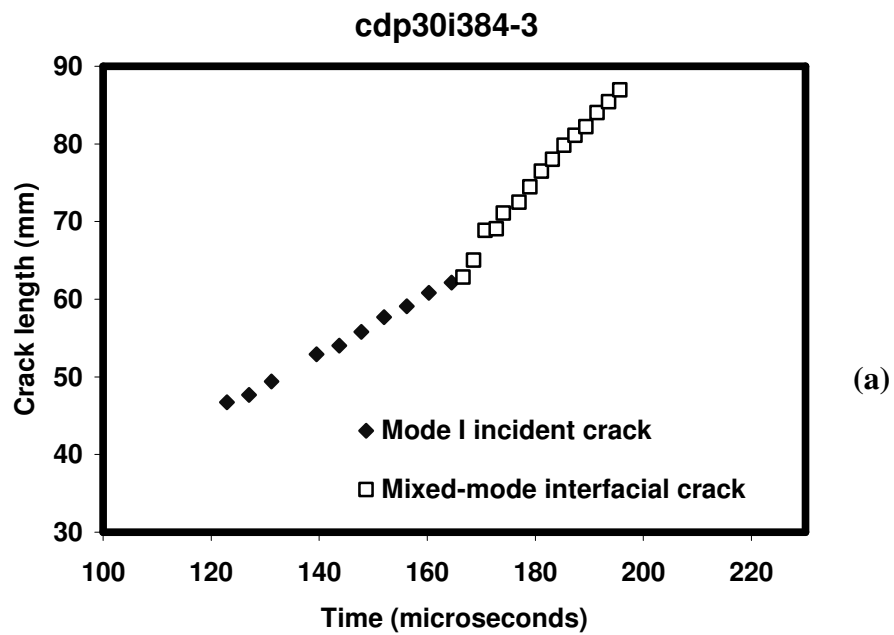
Interface

Figure 2.2,   Crack length history (a) and crack speed history (b) before and after crack deflection at a weak interface (specimens' code cdp30i384-Crack Deflection experiments using Photo-elasticity, interfacial angle 30 degrees; Interfacial bonding using Loctite 384 adhesive).
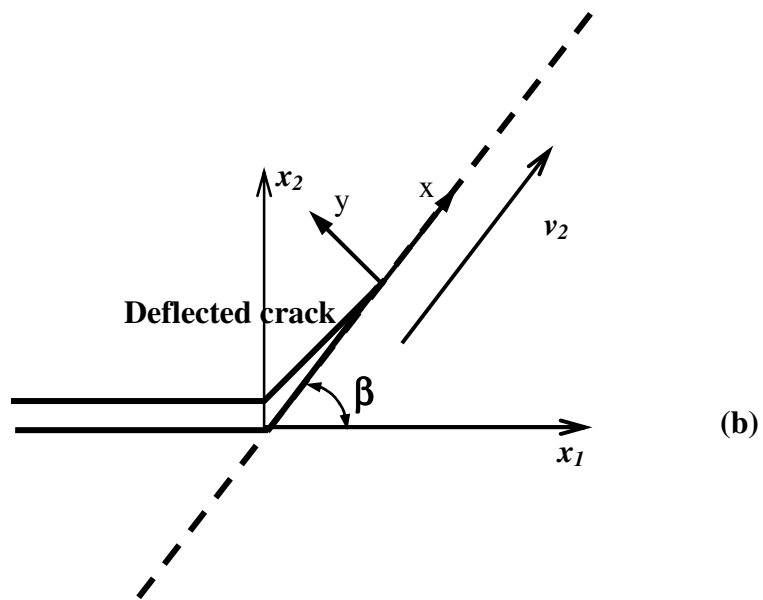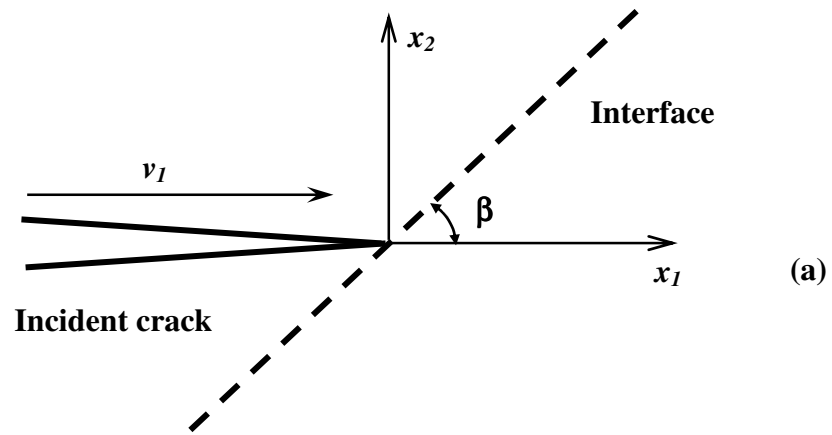
Figure 2.3, Schematic diagram showing a mode-I crack arriving (a) and subsequently deflecting at a weak interface between two identical homogenous solids (b).

Dynamic fracture mechanics analysis

Figure 2.3 shows a schematic diagram describing the geometry relevant to the dynamic crack deflection/kinking problem. Two identical homogeneous and isotropic elastic solids are bonded along an interface indicated here by the dashed line. The Young's and shear moduli, Poisson's ratio and mass density are denoted by E,μ, υ and ρ respectively. Before reaching the interface, a dynamic steady mode-I crack propagates within a homogenous and elastic solid as shown in Figure 2.3(a). The angle between the incident crack plane and the inclined interface is denoted by β. In this investigation, we mainly analyze the dynamic failure mechanics governing the transition of an incident mode-I crack to a mixed-mode interfacial crack as shown in Figure 2.3(b).

Stress field around the tip of a dynamically propagating mode I crack

Stress field of a steady mode I crack is given by a well-known form (see Ramulu and Kobayashi, 1985; Freund, 1990):

$$\sigma_{ij}^{I} = \frac{K_I(t)}{\sqrt{2\pi r}} \Sigma_{ij}^{I}(\theta, v) + T\delta_{i1}\delta_{j1} + O(1) \qquad (2.1)$$

where $K_I(t)$ is the dynamic stress intensity factor of the mode I crack as a function of time t; T is a non-singular term, which is called "the T-stress" or σ_{ox} (Dally, 1979) ; $O(1)$ represents higher order terms; the functions $\Sigma_{ij}^{I}(\theta, v)$ that represent the angular variation of stress components for an instantaneous crack tip speed v are listed in the appendix.

Stress field around the tip of a dynamically propagating mixed mode crack

Similarly, the asymptotic stress field of a steady mode II crack can be expressed by

$$\sigma_{ij}^{II} = \frac{K_{II}(t)}{\sqrt{2\pi r}} \Sigma_{ij}^{II}(\theta, v) + O(1) \tag{2.2}$$

$K_{II}(t)$ is the dynamic stress intensity factor of the mode II crack as a function of time t. There is no T-stress involved in a pure mode-II crack stress expression. The functions $\Sigma_{ij}^{II}(\theta, v)$ that represent the angular variation of stress components for an instantaneous crack tip speed v are given in the appendix.

Based on equation (2.1) and equation (2.2), the stress field of a mixed-mode crack can be obtained using linear superposition principle:

$$\begin{aligned}
\sigma_{ij} &= \sigma_{ij}^{I} + \sigma_{ij}^{II} \\
&= \frac{K_I(t)}{\sqrt{2\pi r}} \Sigma_{ij}^{I}(\theta, V) + T\delta_{i1}\delta_{j1} + \frac{K_{II}(t)}{\sqrt{2\pi r}} \Sigma_{ij}^{II}(\theta, V) + O(1) \tag{2.3}
\end{aligned}$$

In order to evaluate these stress fields, photoelasticity technique is employed to generate isochromatic fringe patterns, which are directly related to the dynamic stress fields.

Isochromatic fringe patterns of dynamic cracks

Recall the maximum in-plane shear stress τ_m is related to the three in-plane stress components by

$$\tau_m^2 = (\frac{\sigma_{11} - \sigma_{22}}{2})^2 + \sigma_{12}^2 \tag{2.4}$$

And the governing equation for the isochromatic fringe pattern is (Kobayashi, 1987):

$$\tau_m = \frac{Nf_\sigma}{2h} \tag{2.5}$$

where N is the fringe order, f_σ is the material fringe constant and h is the specimen thickness. From equation (2.4) and equation (2.5), we get

$$(\frac{Nf_\sigma}{2h})^2 - (\frac{\sigma_{11} - \sigma_{22}}{2})^2 - \sigma_{12}{}^2 = 0 \qquad (2.6)$$

Substitution of equation (2.3) into equation (2.6) leads to an equation, which describes the shape of the dynamic isochromatic pattern (Sanford and Dally, 1979):

$$(\frac{Nf_\sigma \sqrt{2\pi r}}{2h})^2 - (K_I B_1 B_2 + K_{II} B_4 B_5 + \frac{T\sqrt{2\pi r}}{2})^2 - (K_I B_1 B_3 + K_{II} B_6)^2 = 0 \qquad (2.7)$$

where $B_1, B_2, B_3, B_4, B_5, B_6$ are functions defined by

$$B_1 = \frac{1 + \alpha_s^2}{D} \qquad\qquad B_2 = (1 + \alpha_d^2)\frac{\cos\frac{1}{2}\theta_d}{\sqrt{\gamma_d}} - \frac{4\alpha_s \alpha_d}{1 + \alpha_s^2}\frac{\cos\frac{1}{2}\theta_s}{\sqrt{\gamma_s}} \qquad (2.8)$$

$$B_4 = -2\alpha_s / D \qquad\qquad B_3 = 2\alpha_d \left\{ \frac{\sin\frac{1}{2}\theta_d}{\sqrt{\gamma_d}} - \frac{\sin\frac{1}{2}\theta_s}{\sqrt{\gamma_s}} \right\} \qquad (2.9)$$

$$B_5 = (1 + \alpha_d^2)\frac{\sin\frac{1}{2}\theta_d}{\sqrt{\gamma_d}} - (1 + \alpha_s^2)\frac{\sin\frac{1}{2}\theta_s}{\sqrt{\gamma_s}} \quad B_6 = \frac{1}{D}(4\alpha_s \alpha_d \frac{\cos\frac{\theta_d}{2}}{\sqrt{\gamma_d}} - (1 + \alpha_s^2)^2 \frac{\cos\frac{\theta_s}{2}}{\sqrt{\gamma_s}}) \quad (2.10)$$

The $N - K$ relation given in equation (2.7) is non-linear in terms of the three unknown parameters K_I, K_{II} and T. There are several approaches to solve the nonlinear equation. In this investigation, we mainly use the over-deterministic method (Sanford and Dally, 1979) to obtain K_I, K_{II} and T. From equation (2.7), we can define a governing function as follows:

$$f(K_I, K_{II}, T) = (\frac{Nf_\sigma \sqrt{2\pi r}}{2h})^2 - (K_I B_1 B_2 + K_{II} B_4 B_5 + \frac{T\sqrt{2\pi r}}{2})^2 \quad \text{(2.11)}$$

$$- (K_I B_1 B_3 + K_{II} B_6)^2 = 0$$

For a specific fringe order N, we can measure several data points as long as their distances to the crack tip are more than half specimen thickness as suggested by Rosakis and Ravi-Chandar (1986). Substituting these data points into equation (2.11), we can get a series of equations to determine three unknown parameters K_I, K_{II}, T using the least squares method.

For a crack kinking problem, the T-stress is quite important. As noted by Cotterell and Rice (1980), static crack kinking or deflection is directly related to the sign of the T-stress. In order to compare the relative values of the T-stress for different cases, a so-called "biaxial ratio" was introduced by Leevers and Radon (1982):

$$BR = \frac{T\sqrt{\pi a}}{K_I} \quad \text{(2.12)}$$

Although the biaxial ratio was initially employed for static cracks only, it will be used to characterize the dynamic crack case in this investigation using the dynamic stress intensity factors, the T-stress values and the crack lengths. In the following sections, the history of the dynamic stress intensity factors and the T stress as well as the biaxial ratio of the incident crack will be analyzed.

Relation of an incident mode I crack and a kinked mixed-mode crack

As seen in Figure 2.1, an incident crack is mode-I dominated, as evidenced by its symmetric fringe patterns, while the kinked interfacial crack is indeed a mixed-mode crack with un-symmetric patterns. The interesting fringe pattern transition is a result of the stress intensity factor and mode-mixity changes at the interface. Figure 2.3 shows a schematic diagram describing the geometry relevant to the dynamic crack deflection/kinking problem.

Under certain circumstances, the dynamic crack stress intensity factor K_I^d can be related to its static counterpart K_I^s through a "universal function of crack tip speed," $k_I(v)$ (Freund, 1990)

$$K_I^d = k_I(v) K_I^s \tag{2.13}$$

Similarly,

$$K_{II}^d = k_{II}(v) K_{II}^s \tag{2.14}$$

where

$$k_I(v) \cong \frac{1 - v/c_R}{\sqrt{1 - v/c_d}}, \qquad k_{II}(v) \cong \frac{1 - v/c_R}{\sqrt{1 - v/c_s}} \tag{2.15}$$

On the other hand, let K_I^{sk}, K_{II}^{sk} denote static mode-I and mode-II stress intensity factors for the deflected (kinked) mixed-mode crack, and they are related to the static stress intensity factors of the incident dynamic cracks as a function of the kinking angle β (see Hutchinson and Suo, 1992; Anderson, 1995):

$$K_I^{sk} = c_{11} K_I^s + c_{12} K_{II}^s \qquad (2.16)$$

$$K_{II}^{sk} = c_{21} K_I^s + c_{22} K_{II}^s \qquad (2.17)$$

where the coefficients are:

$$c_{11} = (\frac{3}{4}\cos\frac{\beta}{2} + \frac{1}{4}\cos\frac{3\beta}{2}) \qquad c_{12} = -\frac{3}{4}(\sin\frac{\beta}{2} + \sin\frac{3\beta}{2}) \qquad (2.18)$$

$$c_{21} = (\frac{1}{4}\sin\frac{\beta}{2} + \frac{1}{4}\sin\frac{3\beta}{2}) \qquad c_{22} = (\frac{1}{4}\cos\frac{\beta}{2} + \frac{3}{4}\cos\frac{3\beta}{2}) \qquad (2.19)$$

Let v_2 denote the speed of the deflected crack tip at the instant right after deflection, and let K_I^{dk}, K_{II}^{dk} be dynamic mode-I and mode-II stress intensity factors for the deflected (kinked) mixed-mode crack. We still assume that the universal relation between the dynamic and static stress intensity factors also holds for the deflected crack tip, i.e.,

$$K_I^{dk} = k_I(v_2) K_I^{sk} \qquad (2.20)$$

$$K_{II}^{dk} = k_{II}(v_2) K_{II}^{sk} \qquad (2.21)$$

where v_2 is the crack tip speed of the kinked crack. Based on the above relations, if we know the dynamic stress intensity factors, the crack tip speed of the incident crack, the kink angle as well as the crack tip speed of the kinked crack, we can get the dynamic stress intensity factors of the kinked crack and hence the crack tip stress fields around the deflected crack using equation (2.3). Also, based on equations (2.4) and (2.5), we can predict the fringe patterns of the interfacial crack. It should be noticed that the above relations are only applicable to a special situation: an interfacial crack initiated right after the incident crack reached the interface. In some situations, the interfacial crack initiated before the incident crack reached the interface as recorded by Xu and Rosakis (2003). Then, different fracture theory should be employed.

Besides the crack tip stress fields of the mixed-mode interfacial crack, mode mixity is one of the most important parameters in interface fracture mechanics analysis (Hutchinson and Suo, 1992), which is defined by the non-dimensional ratio of the dynamic mode II stress intensity factor over its mode I counterpart:

$$tg\Phi = \frac{K_{II}^{dk}}{K_{I}^{dk}} = \frac{k_{II}(v_2)K_{II}^{sk}}{k_{I}(v_2)K_{I}^{sk}}$$

(2.22)

Substituting equations (2.15), (2.16) and (2.17) into equation (2.22), we obtain:

$$tg\Phi = \frac{\sqrt{1 - v_2/c_d}(\sin\frac{\beta}{2} + \sin\frac{3\beta}{2})}{\sqrt{1 - v_2/c_s}(3\cos\frac{\beta}{2} + \cos\frac{3\beta}{2})}$$

(2.23)

It is not surprising to see that the dynamic mode mixity is a function of the kinking angle and the crack tip speed, which is different from the static crack kinking or deflection.

Here we should pay great attention to the T stress change after crack kinking. The T-stress is the non-singular, constant term in William's series solutions. It acts along the crack surface and is determined only by the far-field load (Yang and Ravi-Chandar, 1999; Jayadevan et al., 2001; Chen et al, 2001; Paulino and Kim, 2004). According to the stress tensor decomposition principle, there will be three non-singular constant stress components acting on the path of kinked crack. Indeed, there were no convincing results on the T-stress change at crack kinking in previous investigations (Gao, and Chiu, 1992; Selvarthinam and Goree, 1998). However, the effect of the T-stress on crack kinking is quite significant (Yang and Yuan, 2000; Becker et al. 2001; Chen and Dillard, 2001; Chao et al., 2001; Maleski et al., 2004). Very recently, Li and Xu (2006)

extensively discussed the T-stresses across static crack kinking. Analytical results on the T-stress change across dynamic crack kinking are still not available.

Results and discussion

Stress intensity factors and the T-stress for the incident crack

In this section, we mainly analyze the dynamic fracture parameters of the crack deflection experiments reported by Xu et al. (2003). Figure 2.1 shows a series of dynamic photoelasticity images of the incident crack propagating towards the inclined interface (interfacial angle 30^0). The incident crack speed was approximately 400m/s. Using the over-deterministic method to fit these fringes led to the history of the stress intensity factor and the T stress of the incident crack as shown in Figure 2.4 and Figure 2.5. K_I is approximately 0.5 MPa*m$^{1/2}$. It is not surprising to see that K_{II} is close to zero since the incident crack was indeed a mode I crack. The above results verified the wedge-loading mechanism for controlling an opening crack (Xu, et al., 2003). However, the change of the T stress with time and crack length was quite large (see Figure 2.5) and the T stress ranged from 0.5 to 1.5 MPa. For the same material and interface bond, another experiment was conducted using a higher projectile impact speed. Figure 2.6 and Figure 2.7 show the history of the stress intensity factors and the T stress for this case. Comparing Figure 2.4 with Figure 2.6, it was obvious that a high impact speed led to a high mode I stress intensity factor (from 0.5 MPa*m$^{1/2}$ to 0.8 MPa*m$^{1/2}$) and the T-stress (related to the stress along the crack path). Figure 2.8 compares the history of two biaxial

ratios for these two cases. The biaxial ratio is related to the normalized T stress and it is

expected to be a geometry-independent parameter. Obviously, for different load cases but

the same material and interface, it is hard to find common features in Figure 2.8.

Figure 2.4,   Dynamic stress intensity factors (SIFs) as functions of (a) time and
(b) crack length of the incident crack (interfacial angle 30 degrees).

cdp30i384-3

(a)

cdp30i384-3

(b)

Figure 2.5, Non-singular T-stress as functions of (a) time and (b) crack length of the incident crack (interfacial angle 30 degrees).

k30hm384-1

k30hm384-1
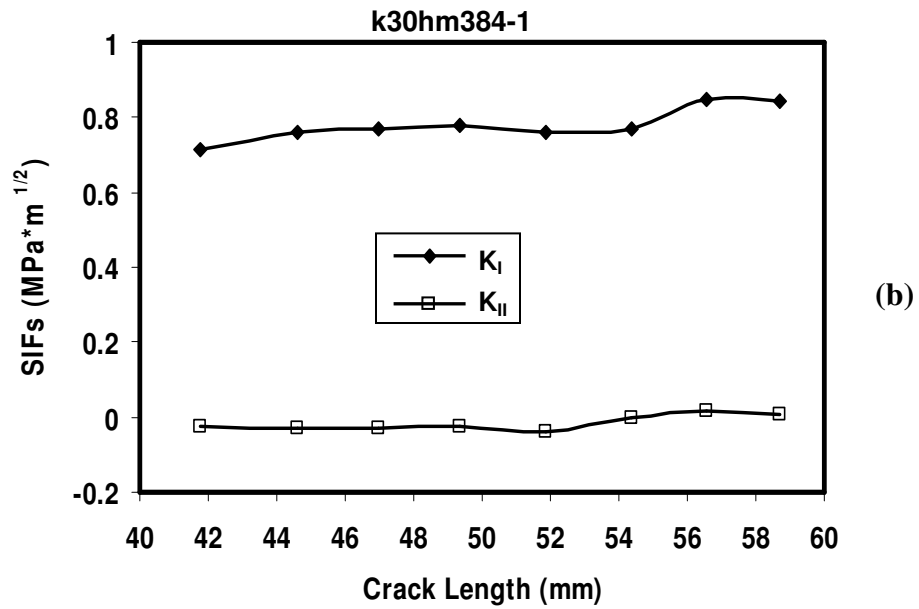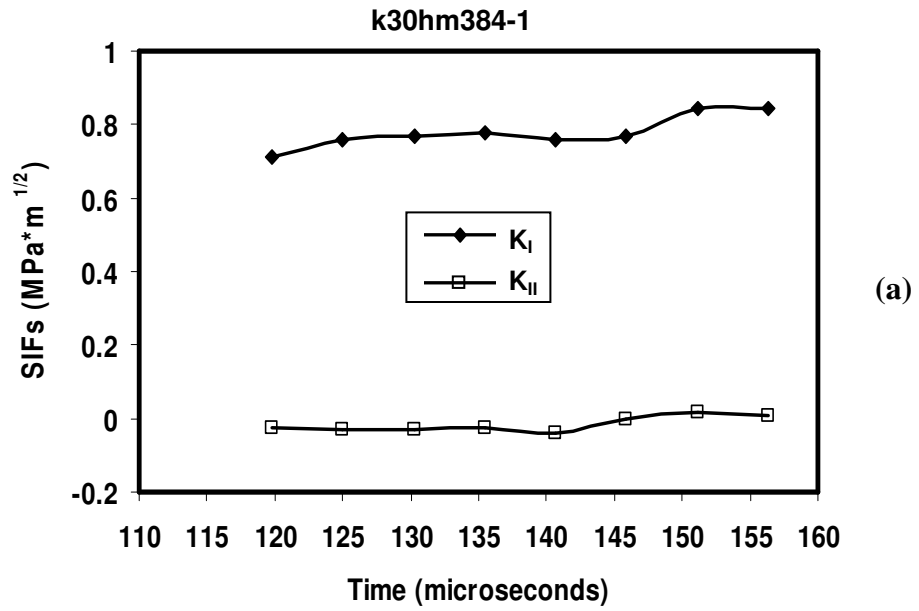
Figure 2.6, Dynamic stress intensity factors (SIFs) as functions of (a) time and (b) crack length of the incident crack from a higher speed impact (interfacial angle 30 degrees).
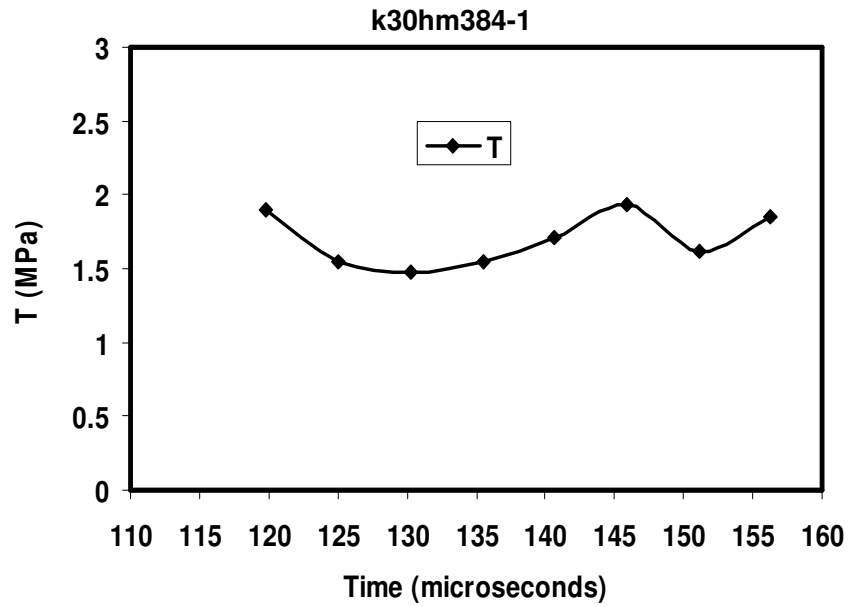
Figure 2.7, T-stress as functions of time of the incident crack from a higher speed impact (interfacial angle 30 degrees).
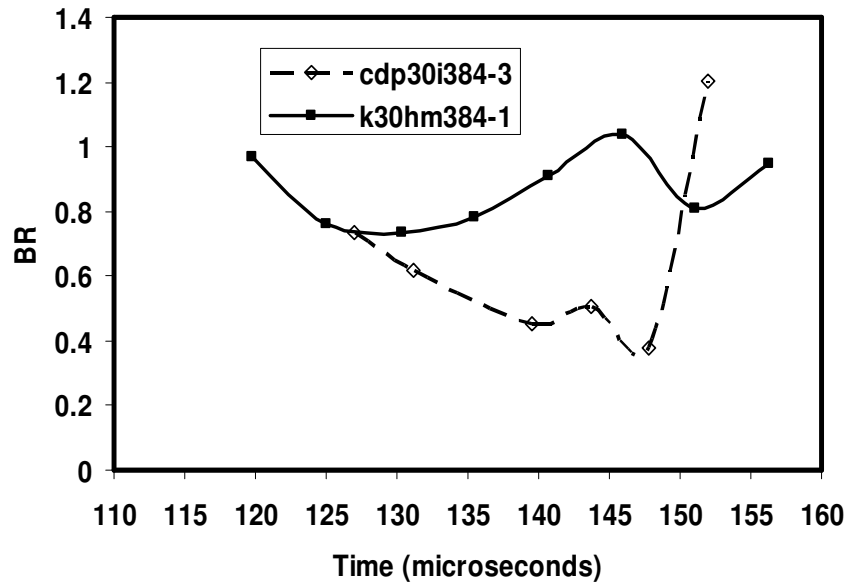
Figure 2.8, Biaxiality ratio as functions of time of the incident crack for different speed impact (interfacial angle 30 degrees).

One interesting issue is the influence of the T stress on the crack path stability. According to Cotterell and Rice (1980), the crack growth is stable if T<0 and unstable if T >0. For the present dynamic crack propagation case, our results indicate that this statement might be modified. In our dynamic experiments as shown in Figure 2.8, the T stress was always greater than zero for the incident mode I cracks, but their crack paths (as indicated by curves macroscopically) were pretty stable as shown in Figure 2.1. Recently, some researchers also show the sign of the T-stress was not enough to judge the crack stability and other parameters should be introduced. Melin (2002) showed that when T>0, the crack path was still stable. Richardson and Goree (1993) also observed that in PMMA specimens of different dimensions, the crack did not kink immediately if the T stress became positive.

In order to verify the fitting process, we plotted one recovered fringe pattern using the fitted stress intensity factors and compared with the experimental pattern. As shown in Figure 2.9, it can be seen that two fringes agreed well. Similarly, Figure 2.10 and Figure 2.11 showed history of the stress intensity factors and the T stress for the case of interfacial angle 45^0. For the case of interface angle 60^0, we analyzed two different interfacial bonding strengths, and the history of the stress intensity factors and the T stresses were shown in Figure 2.12. Based on the history of the stress intensity factors and the T stresses in different load and interface cases, we find that the same impact speed leads to the same level of dynamic stress intensity factors for the mode I incident crack. Furthermore, for different interfacial angles, the stress intensity factors of incident

cracks are almost the same since the interfacial angle only affects the kinked crack. All these results indicated that the wedge loading mechanism was a good way to produce a stable mode I crack and control the crack tip speed.
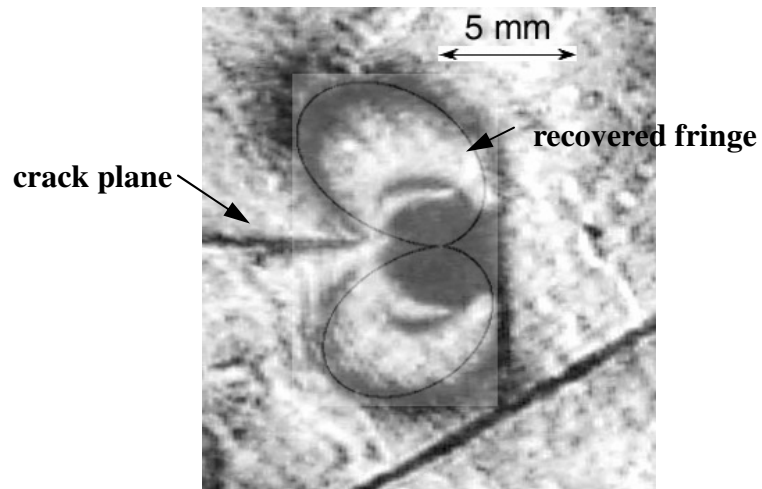
Figure 2.9, Comparison of the experimental fringe and recovered fringe.

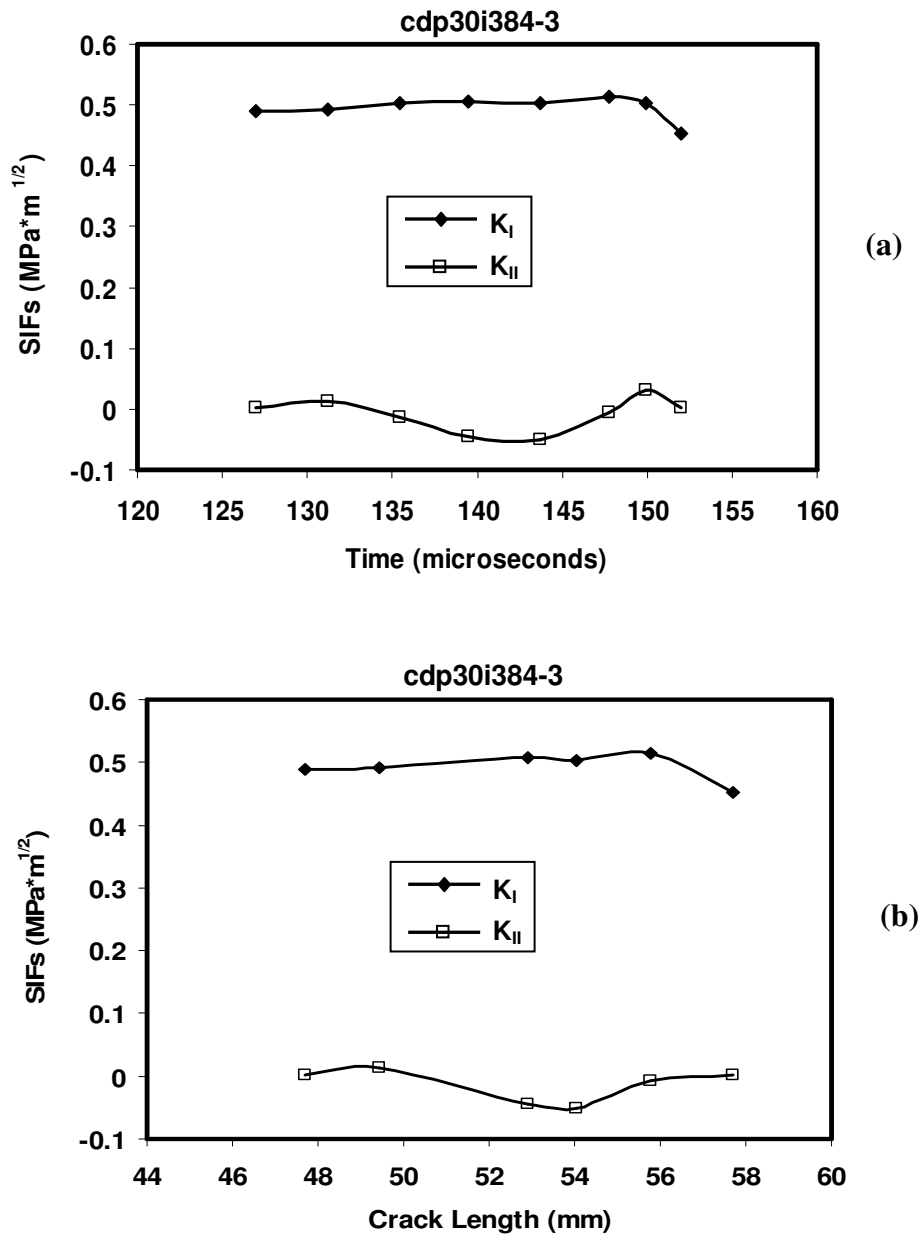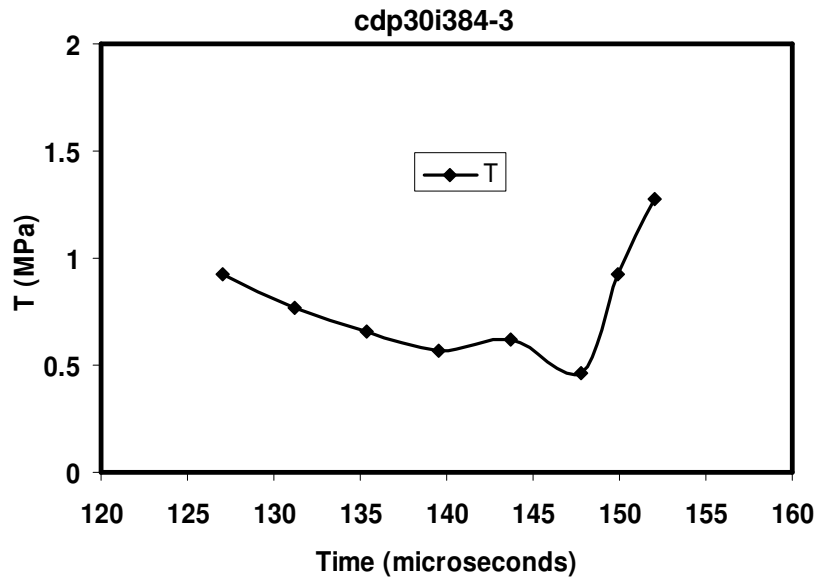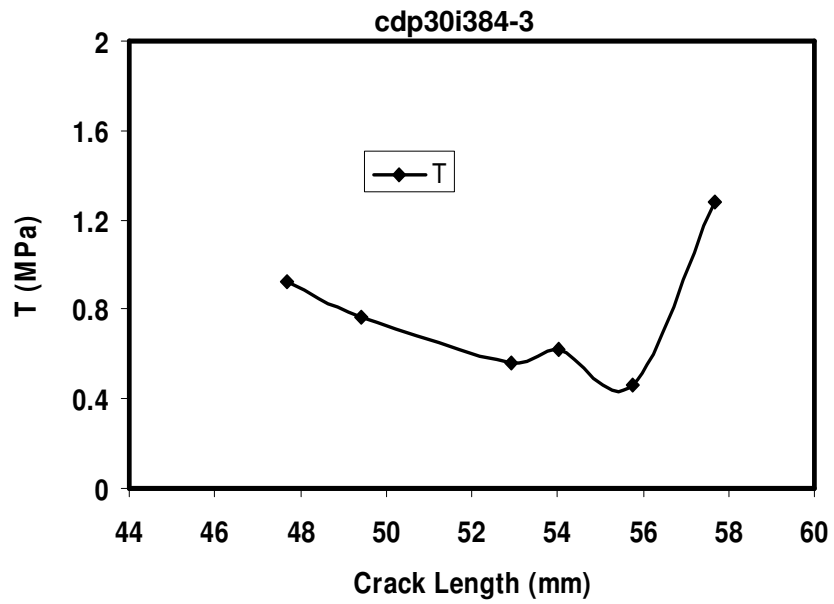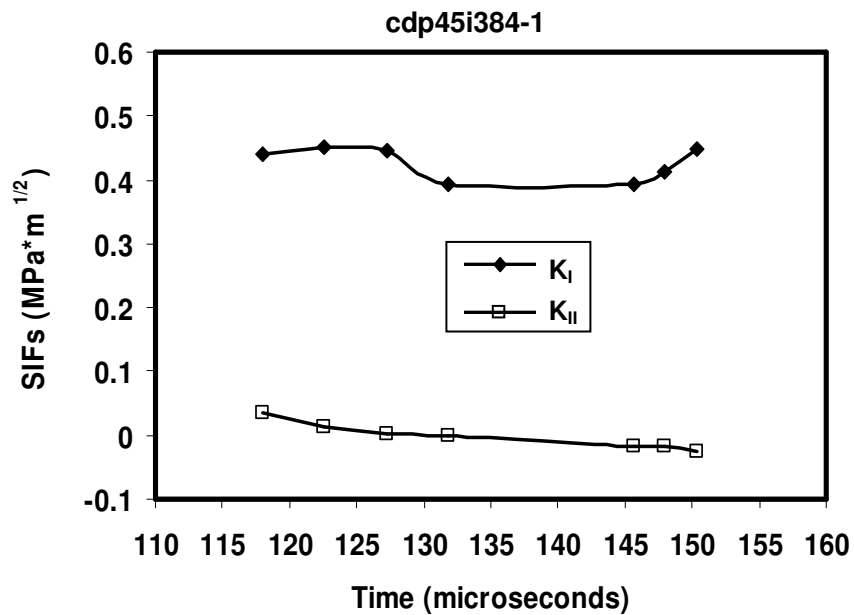Figure 2.10, Dynamic stress intensity factors (SIFs) as functions of time of the incident crack (interfacial angle 45 degrees).

cdp45i384-1
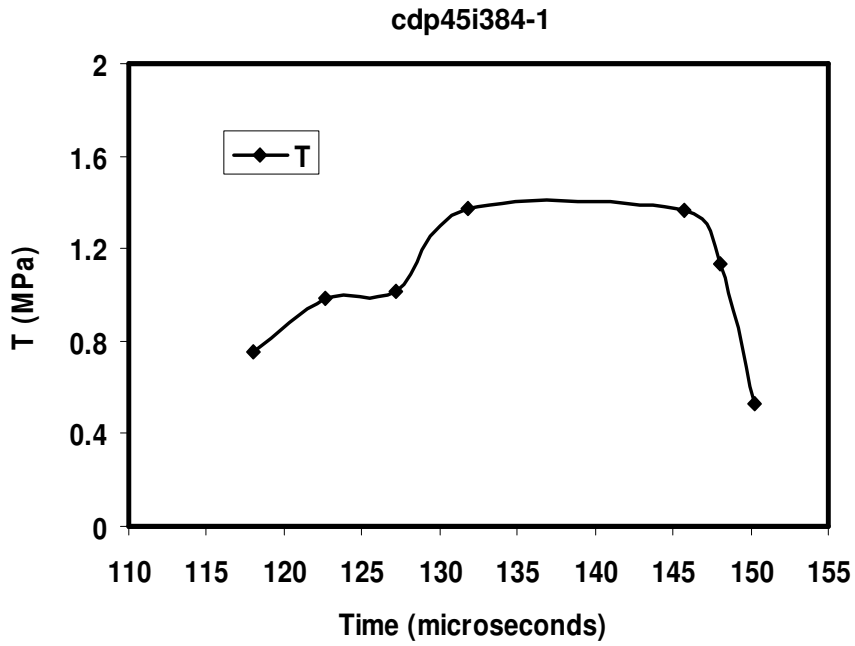
Figure 2.11, Non-singular T-stress as functions of time of the incident crack (interfacial angle 45 degrees).

cdp60i384 & cdp60iwd10

K_I (Strong Interface)

K_I (Weak Interface)

K_{II} (Strong Interface)

K_{II} (Weak Interface)

(a)
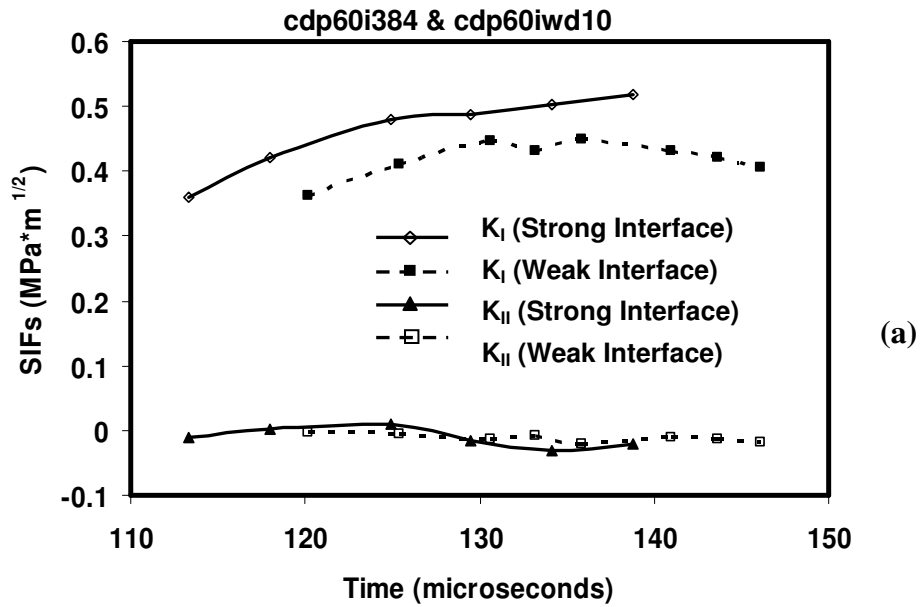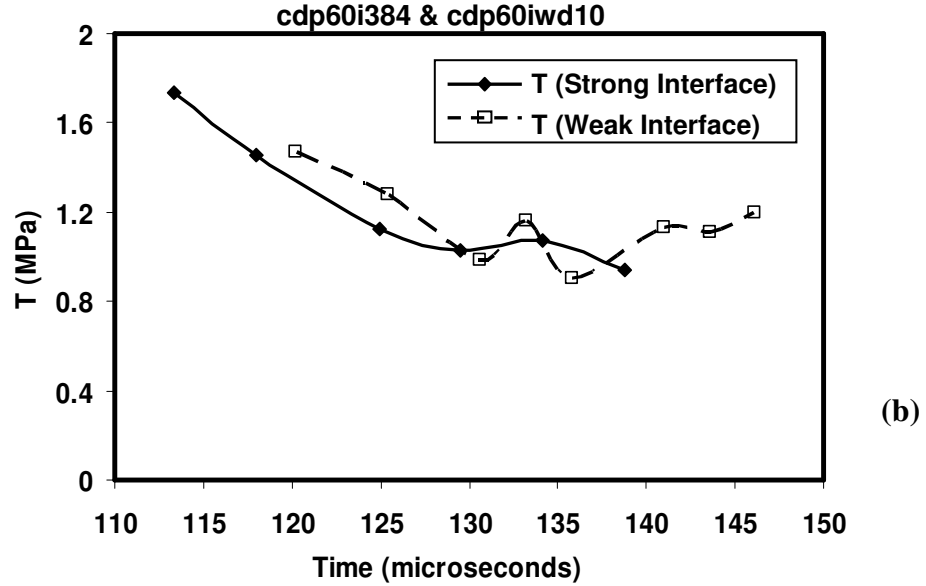
Figure 2.12,   History of (a) the stress intensity factors (SIFs) and (b) the T stress of two incident cracks (interfacial angle 60 degrees).

Predicted fringe patterns of the kinked interfacial crack

After fitting the stress intensity factors K_I^d, K_{II}^d and the T stress of the incident crack, we can predict the kinked interfacial crack using fracture mechanics theory.   Our first step is to obtain the static counterparts of the dynamic stress intensity factors using equation (2.13). After crack deflection, the dynamic stress intensity factors of the kinked crack can be calculated using equations (2.16), (2.17) and equations (2.20), (2.21). Then, the fringe patterns of the interfacial crack at the moment of crack deflection can be predicted using equations (2.3) and (2.5).   Because it is very hard to record the exact moment of crack kinking at the interface in dynamic fracture experiments, average values

of the stress intensity factors of the incident crack were used to calculate the stress intensity factors of the kinked interfacial crack.

Figure 2.13 showed the predicted fringe pattern of a kinked interfacial crack (interfacial angle 30^0). The coordinate origin is located at the intersection point of the incident crack and the kinked crack, and its x-axis is along the interface. For this case, the crack tip speed of the incident crack was around $400 m/s$. Right after crack kinking, the interfacial crack tip speed was about $800 m/s$ (Xu et al., 2003). Since the T-stress of the incident crack is around 1 MPa, and there are no convincing results for the T-stress of the kinked crack, the T-stress of the kinked crack was assumed to be zero in all our predictions.   In order to highlight our comparison of the predicted and experimental fringe patterns, only fringe order 1 was plotted. Figure 2.13(a) presented the experimental fringe showing the transition from an incident crack to an interface crack (the horizontal line was the interface). Figure 2.13(b) showed the predicted fringe and the two kinds of photoelasticity fringes were very similar. Figure 2.14 and Figure 2.15 showed the experimental and predicted fringe patterns for interfacial angles of 45^0 and 60^0, respectively. All these cases indicated that the predicted fringes and the experimental fringes generally agreed well and they demonstrated that our dynamic fracture mechanics modeling and assumptions were reasonable. However, some discrepancy is also noticed because (a) it is very hard to take one photo at the right time and right position as the theoretically predicted one. (b) T stress has significant influence on these fringe patterns. But no one reported the T-stress after dynamic crack kinking.

One interesting observation is the large concave wedge effect. As seen in Figure 2.15(a), two caustic spots (one caused by the kinked crack tip and the other due to a large concave wedge) were clearly observed when a mode-I incident crack kinked along a weak interface with a large kinking angle (60° degrees). In most previous crack kinking analyses, researchers only considered the singular stress field due to a kinked daughter crack and ignored the singular stress field of a concave wedge. Interestingly, William's classical solution of wedge stress singularities (1952) is the foundation of the full-field stress field of a traction-free crack in Linear Elastic Fracture Mechanics (Williams, 1957). Indeed, Cotterell and Rice's (1980) classical work mainly deals with a slightly kinked crack, not a large kinking angle case. To authors' knowledge, only Azhdari and Nemat-Nasser (1996) provided a simple explanation to this phenomenon for a static crack kinking case.
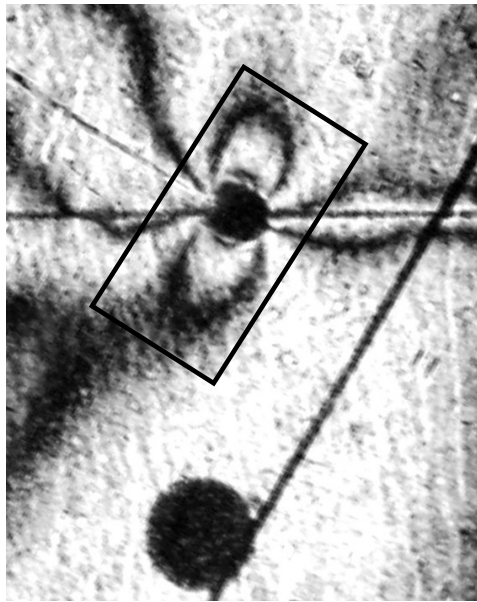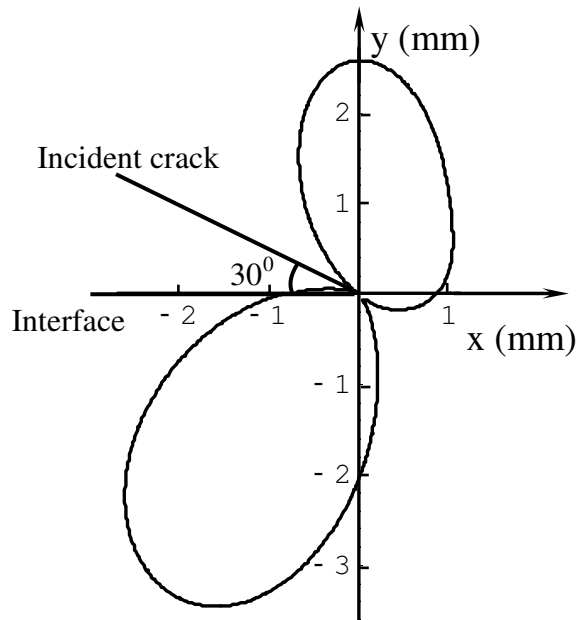
Figure 2.13, Comparison of (a) experimental fringe (strong interface) and (b) predicted fringe pattern ($v_1 = 400m/s$, $v_2 = 766m/s$, $N = 1$) for interfacial angle 30 degrees.
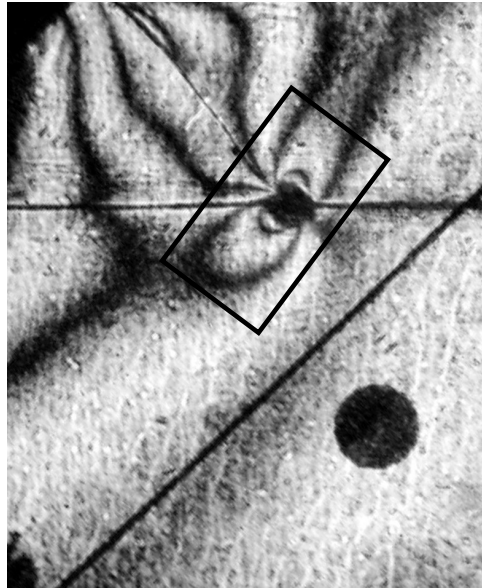
(a)
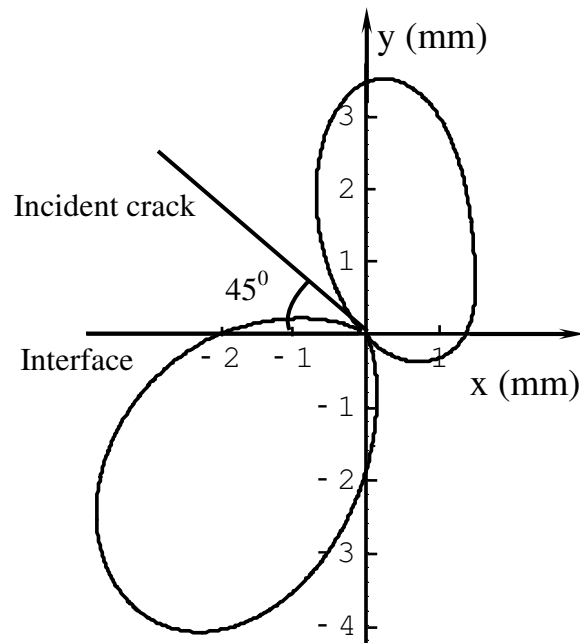
(b)

Figure 2.14, Comparison of (a) experimental fringe (strong interface) and (b) predicted fringe pattern ($v_1 = 400m/s$, $v_2 = 800m/s$, $N = 1$) for interfacial angle 45 degrees.
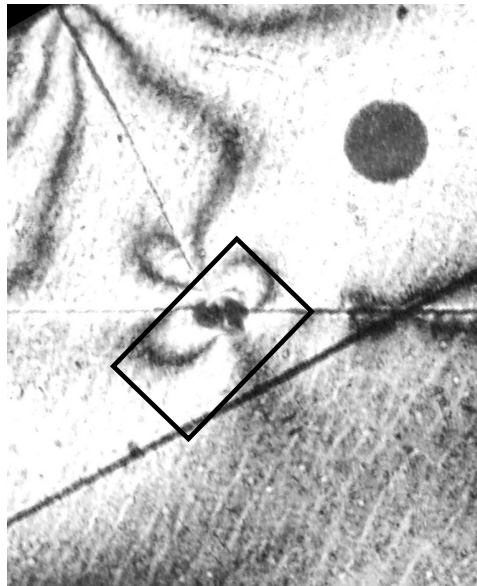
(a)
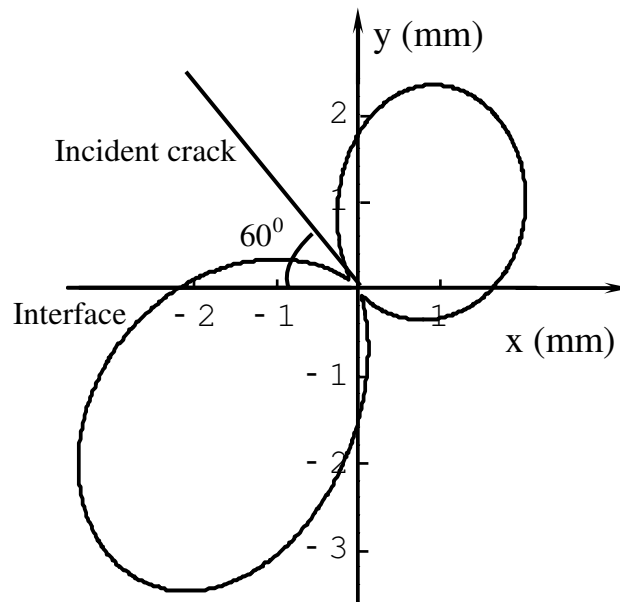
(b)

Figure 2.15, Comparison of (a) experimental fringe (strong interface) and (b) predicted fringe pattern ($v_1 = 400m/s$, $v_2 = 700m/s, N = 1$) for interfacial angle 60 degrees.

Mode mixity of the kinked interfacial crack

Mode mixity is an important parameter in interface fracture analysis. It is the ratio measure of the mode II stress intensity factor/energy release rate over its mode I counterparts. There were numerous studies on mode mixity in static fracture cases but very few results were reported in dynamic fracture investigation (He and Hutchinson, 1989; Gupta et al., 1992; Ravi-Chandar et al., 2000). Indeed, mode mixity is a key parameter in controlling failure mode transitions along interfaces.   In this investigation, when the incident mode I crack reached the interface, it kinked along the interface and became one mixed mode crack.   Based on equation (2.23), for the kinked interfacial crack, its mode mixity depends on the kinked crack tip speed and the interfacial or kinking angle. Obviously, the dependence on the dynamic mode mixity on the crack tip speed is a special phenomenon in dynamic fracture mechanics.

The variations of the mode mixity with the interfacial angle and the kinked crack tip speed are plotted in Figure 2.16. It is not surprising to see that when the crack tip speed of the interfacial crack remained constant, mode mixity increased with the increase of the kinking angle.   In other words, the larger of the interfacial angle, the larger is the mode II component for the mixed mode crack. This result is similar to the common conclusion in static crack kinking analysis (Anderson, 1995). As a special feature of dynamic crack kinking, the mode mixity increases with the increasing kinked crack speed if the interface angle is fixed.   In Figure 2.16(a), for a fixed kinking or interfacial angle 50°, the mode mixity for a high crack tip speed (90% of the shear wave speed of the matrix material) is

almost doubled compared to the mode mixity for a static kinked crack. Here, we should notice that the crack tip speed of the kinked crack is related to the interfacial bonding strength (Xu et al., 2003). A weak interface will lead to a fast interfacial crack tip speed and a high mode-II component as a result. Figure 2.16(b) shows the mode mixity dependence on the crack tip speed for different kinking angles.   It is interesting to see that each curve has a similar shape and is shifted by some amount for a different kinking angle.   In this investigation, the kinking or interfacial angle is limited to 0-90 degrees. Recently, Rousseau and Rosakis (2003) examined important crack kinking behavior for very large interfacial angle (greater than 90 degrees). One important difference is that their incident crack was an inter-sonic shear crack along a weak path rather than a slow mode-I crack as in our investigation. In order to suppress possible crack branching, our incident crack speed was controlled to be less than the crack branching speed (around 30-40% of the shear wave speed for Homailte-100).   Chalivendra and Rosakis (2004) used the same wedge-induced crack but along a weak path such that the incident mode-I crack was close to the Rayleigh wave speed (around 90% of the shear wave speed, see Lee and Knauss (1989)).   In all these investigations, the mode mixity of the kinked interfacial crack was found to depend on not only the kinking angle but also on the crack tip speed.

(a)

(b)
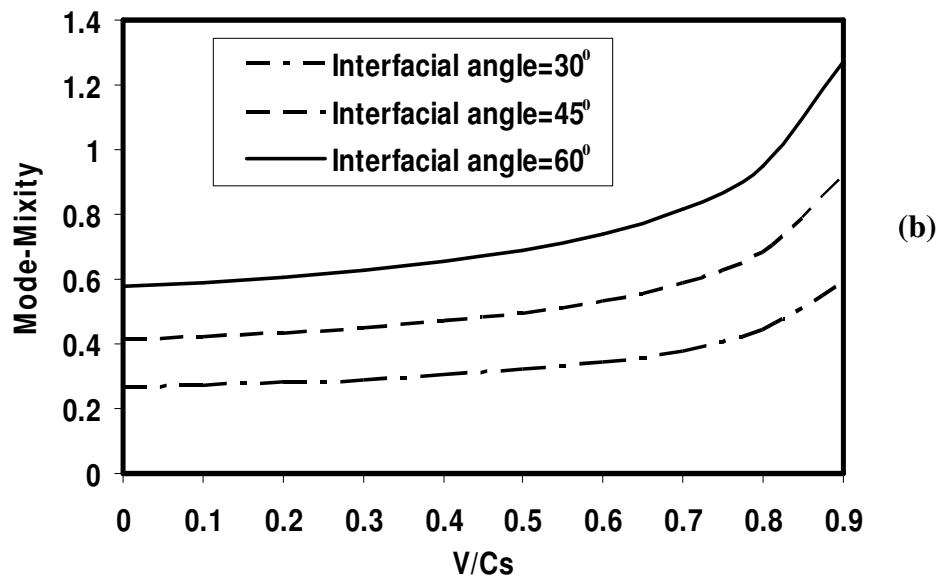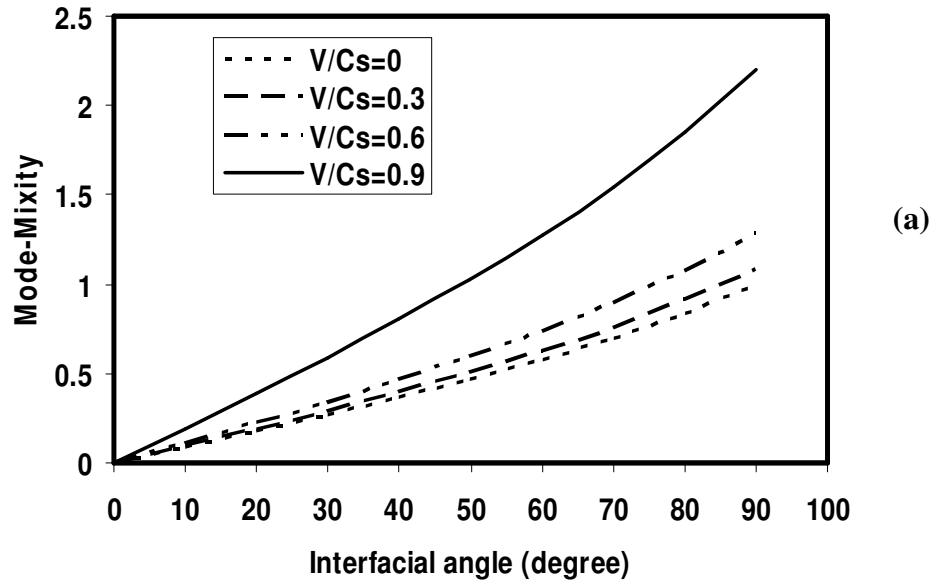
Figure 2.16, Dynamic facture mode mixity as functions of (a) interfacial angle and (b) crack tip speed.

CHAPTER III

DYNAMIC INTERFACIAL DEBONDING INITIATION INDUCED BY AN
INCIDENT CRACK

Introduction

When a crack propagates in elastic solids and encounters an interface, one of the

three situations may occur as seen in Figure 1.1(b) in chapter I: (a) after the crack reaches

the interface, it kinks out of its original path and continues to propagate along the

interface. This phenomenon is often called "crack kinking or deflection" (Martinez and

Gupta, 1994; Prakash et al., 1995; Kerans and Parthasarathy, 1999; Davis et al., 2000;

Leguillon et al., 2001); (b) the crack penetrates the interface and continues to propagate

along its original path, i.e., crack penetration (He et al., 2000; Xu et al., 2003; Roham et

al., 2004); (c) early interface debonding initiates before the incident crack reaches the

interface, or it refers to the "Cook and Gordon mechanism" (Cook and Gordon, 1964;

Lee et al., 1996;   Warrier et al., 1997; Majumdar et al., 1998;   Pagano, 1998; Leguillon

et al., 2000; Korsunsky,   2001; Baber et al., 2002;   Xu and Rosakis, 2003). In the open

literature, efforts have been primarily focused on analyzing the first two cases, crack

kinking and crack penetration (He and Hutchinson, 1989; Hutchinson and Suo, 1992;

Gupta et al., 1992). The energy release rate ratios of the incident and kinked interfacial

cracks, and the fracture toughness ratios of the matrix material and the interface are

identified as major parameters to govern crack deflection/penetration (Evans and Zok,

1994; Martinez and Gupta, 1994; Ahn et al., 1998; Martin et al., 1998).   Recently, Xu et al. (2003) experimentally and analytically studied the dynamic crack deflection/penetration phenomena. They also presented an energy-based criterion to investigate the competition between the dynamic crack penetration and deflection. However, in order to apply the energy-based criterion, putative crack deflection and crack penetration lengths are needed to evaluate the corresponding energy release rates. Several researchers (Ahn et al., 1998; He et al., 2000; Martin et al., 2001; Lee et al., 2004) have demonstrated that the two putative lengths have a significant effect on the energy release rate ratios, and sometimes the energy-based criterion fails to predict the crack deflection or crack penetration. For these cases, "Cook and Gordon mechanism" provides an alternative explanation since a crack may not kink right after it reaches the interface as shown in Figure 1.1(b). The case (interface debonding before kinking) shown in Figure 1.1(b) is quite possible. However, in case (c), correlations of the fracture mechanics parameters of the kinked interfacial crack and the incident crack are not easy to obtain. Therefore, in order to model the "Cook and Gordon mechanism", we tend to use a strength-based criterion to predict interfacial debonding initiation only (rather than crack growth) induced by an incident crack. In terms of the dynamic "Cook and Gordon mechanism", only Needleman and co-workers (see Siegmund et al., 1997; Arata, et al., 2000; Xuan et al., 2003) have simulated this problem using a cohesive element model. In their model, an artificial initial flaw was introduced so they assumed some material properties for predictions. In our investigation, a strength criterion with direct interfacial

strength measurements will be used to predict the critical distance r_c of the incident crack tip to the intersection point of the incident crack path and the interface, as defined in Figure 3.1(a). Indeed, our work will be complementary to Needleman's work, since our work aims to predict interfacial debonding initiation, while their efforts were focused on simulating the late interfacial crack propagation after crack initiation.

So our objective in this investigation is to understand the mechanics and material insight of interfacial debonding initiation induced by a dynamic incident mode-I crack. In order to avoid complicated stress waves across a bimaterial interface, and to simplify dynamic fracture mechanics modeling, two kinds of bonded brittle polymers (PMMA or Plexiglas and Homalite) will be used to conduct dynamic fracture experiments. Meanwhile, dynamic fracture mechanics modeling incorporating an interfacial strength criterion will be developed to predict interfacial debonding initiation and compared with experimental observations.

Determination of the stress field around a dynamic crack

We consider weakly bonded systems composed of identical constituent solids so that the resulting material remains constitutively homogeneous except for fracture toughness or strength along the interface. By doing so the complication of material properties and wave speed mismatch across the interface is avoided, while the essential properties of a weak path or bond are retained. Figure 3.1(a) shows a schematic diagram describing the

geometry relevant to interface debonding ahead of an incident crack. Two identical homogeneous and isotropic elastic solids are bonded along an interface indicated here by the dashed line. The Young's and shear moduli, Poisson's ratio and mass density are denoted by E, μ, υ and ρ. A dynamic crack is propagating towards the inclined interface between the bonded solids. The angle between the crack path and the interface is denoted by β (interfacial angle).

The stress field around a general dynamic crack and the governing equation of photo-elasticity are described in Chapter II. Here, we omit all the details.

Interfacial debonding initiation ahead of an incident crack

Strength-based criteria

As shown in Figure 3.1(b), let $\sigma_{11}(r_i,\theta_i), \sigma_{22}(r_i,\theta_i)$ and $\sigma_{12}(r_i,\theta_i)$ denote the interfacial stress components at the point (r_i,θ_i) in the main coordinate system whose origin is located at the incident crack tip; $\sigma'_{11}, \sigma'_{22}$ and σ'_{12} denote these stresses acting at the same location but their local coordinate system has an angle β with the main coordinate system. According to the stress transformation law, we get

$$\sigma'_{11} = \sigma_{11}(r_i,\theta_i)\cos^2\beta + \sigma_{22}(r_i,\theta_i)\sin^2\beta + 2\sigma_{12}(r_i,\theta_i)\sin\beta\cos\beta \qquad (3.1)$$

$$\sigma'_{22} = \sigma_{11}(r_i,\theta_i)\sin^2\beta + \sigma_{22}(r_i,\theta_i)\cos^2\beta - 2\sigma_{12}(r_i,\theta_i)\sin\beta\cos\beta \qquad (3.2)$$

$$\sigma'_{12} = \sigma_{12}(r_i,\theta_i)\cos 2\beta + (\sigma_{22}(r_i,\theta_i) - \sigma_{11}(r_i,\theta_i))\sin\beta\cos\beta \qquad (3.3)$$
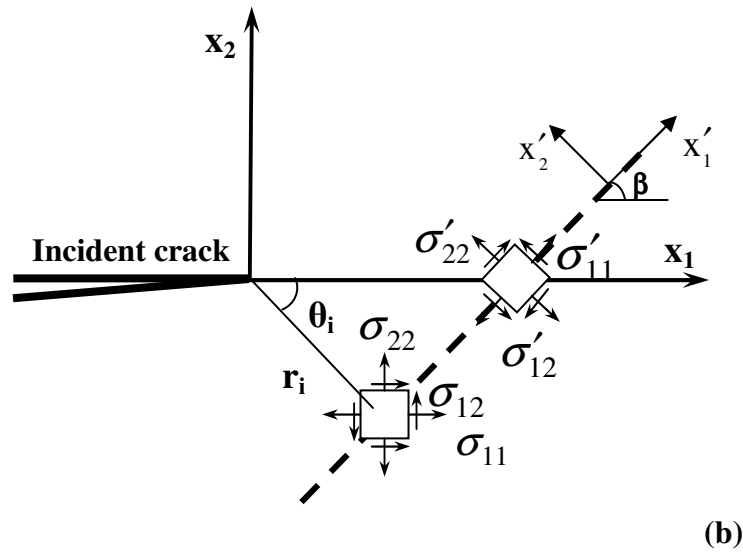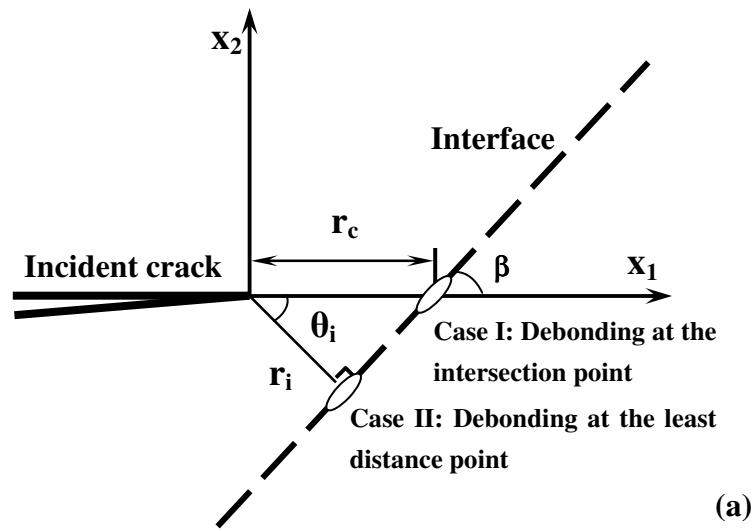
Figure 3.1, Schematic diagrams of (a) debonding initiation at two different points; and (b) stress transformation relation at the interface.

With these stress components in hand; two strength-based criteria are given below

$$\left(\frac{\sigma'_{22}}{\sigma_t}\right) + \left(\frac{\sigma'_{12}}{\tau_s}\right) = 1 \qquad (3.4)$$

and

$$\left(\frac{\sigma'_{22}}{\sigma_t}\right)^2 + \left(\frac{\sigma'_{12}}{\tau_s}\right)^2 = 1 \qquad (3.5)$$

where σ_t and τ_s are the tensile and shear strengths of the interface, respectively. The basic idea behind these two criteria is that once the local tensile stress or shear stress at the interface reaches its critical value (tensile or shear strength), local interfacial debonding initiation will occur. The difference between these two criteria is the exponents of these strength ratios. What makes the strength-based criteria more preferable is that, in this investigation, we focus on interfacial debonding initiation rather than interfacial crack propagation. Our purpose is to find a better criterion to explain physical insight, and to avoid fitting parameters in model predictions. Similarly, Rousseau and Rosakis (2003) used one strength criterion to predict a mode-II interfacial crack initiation.

For convenience, we use criterion I to represent equation (3.4) and criterion II to represent equation (3.5). We will use these criteria to predict two possible cases of crack-interface interaction. In the first situation, the debonding initiation position is the intersection point of the incident crack path and the interface as shown in Figure 3.1(a). This phenomenon was observed by Xu and Rosakis (2003). In their experiments, when

two bonded homalite layers were subjected to transverse impact loading, an incident crack initiated and propagated perpendicularly to the interface. Before the incident crack reached the interface, interface debonding initiated at the intersection point. In the second case, we assume that interfacial debonding initiation will occur at the least distance point if the interface is inclined to the incident crack (see Figure 3.1(a)). Here, the least distance refers to the distance from the incident crack tip (point) to the interface (line).

Case I-Debonding initiation at the intersection point of the incident crack path and the interface

If interface debonding initiates at the intersection point between the incident crack path and the interface as shown in Figure 3.1(a), it implies $\theta_i = 0$ in equation (2.3). So the stress components at the debonding point can be expressed by

$$\sigma_{11}(r_c,0) = \frac{K_I}{\sqrt{2\pi r_c}} \frac{1}{D}\left\{(1+\alpha_s^2)(1+2\alpha_d^2-\alpha_s^2)-4\alpha_s\alpha_d\right\}+T \tag{3.6}$$

$$\sigma_{12}(r_c,0) = \frac{K_{II}}{\sqrt{2\pi r_c}} \frac{1}{D}\left\{4\alpha_s\alpha_d-(1+\alpha_s^2)^2\right\} \tag{3.7}$$

$$\sigma_{22}(r_c,0) = -\frac{K_I}{\sqrt{2\pi r_c}} \frac{1}{D}\left\{(1+\alpha_s^2)^2-4\alpha_s\alpha_d\right\} \tag{3.8}$$

where D, α_s and α_d are defined in the Appendix. Substituting the above expressions into equations (3.1)~(3.3) in combination with equation (3.4) and equation (3.5) leads to

$$\left(\frac{\frac{K_I}{\sqrt{2\pi r_c}}f_1}{\sigma_t}-\frac{\frac{K_{II}}{\sqrt{2\pi r_c}}f_2\sin 2\beta}{\sigma_t}+\frac{T\sin^2\beta}{\sigma_t}\right)+\left(\frac{\frac{K_I}{\sqrt{2\pi r_c}}f_3}{\tau_s}+\frac{\frac{K_{II}}{\sqrt{2\pi r_c}}f_2\cos 2\beta}{\tau_s}-\frac{T\sin\beta\cos\beta}{\tau_s}\right)=1 \tag{3.9}$$

and

$$\left(\frac{\dfrac{K_I}{\sqrt{2\pi r_c}}f_1}{\sigma_t} - \frac{\dfrac{K_{II}}{\sqrt{2\pi r_c}}f_2\sin 2\beta}{\sigma_t} + \frac{T\sin^2\beta}{\sigma_t}\right)^2 + \left(\frac{\dfrac{K_I}{\sqrt{2\pi r_c}}f_3}{\tau_s} + \frac{\dfrac{K_{II}}{\sqrt{2\pi r_c}}f_2\cos 2\beta}{\tau_s} - \frac{T\sin\beta\cos\beta}{\tau_s}\right)^2 = 1 \quad (3.10)$$

where

$$f_1 = \frac{1}{D}\left\{(1+\alpha_s^2)(1+2\alpha_d^2-\alpha_s^2) - 4\alpha_s\alpha_d\right\}\sin^2\beta - \frac{1}{D}\left\{(1+\alpha_s^2)^2 - 4\alpha_s\alpha_d\right\}\cos^2\beta \quad (3.11)$$

$$f_2 = \frac{1}{D}\{4\alpha_s\alpha_d - (1+\alpha_s^2)^2\} \quad (3.12)$$

$$f_3 = -\frac{2}{D}\left\{(1+\alpha_s^2)(1+\alpha_d^2) - 4\alpha_s\alpha_d\right\}\sin\beta\cos\beta \quad (3.13)$$

If the dynamic stress intensity factors, T stress and crack tip speed of the incident crack,

and interfacial tensile and shear strengths are known, based on equations (3.9) and (3.10),

we can predict the critical distance r_c between the incident crack tip and the intersection

point. If the incident crack is a pure mode I crack, equations (3.9) and (3.10) are further

reduced to

$$\left(\frac{\dfrac{K_I}{\sqrt{2\pi r_c}}f_1}{\sigma_t} + \frac{T\sin^2\beta}{\sigma_t}\right) + \left(\frac{\dfrac{K_I}{\sqrt{2\pi r_c}}f_3}{\tau_s} - \frac{T\sin\beta\cos\beta}{\tau_s}\right) = 1 \quad (3.14)$$

and

$$\left(\frac{\dfrac{K_I}{\sqrt{2\pi r_c}}f_1}{\sigma_t} + \frac{T\sin^2\beta}{\sigma_t}\right)^2 + \left(\frac{\dfrac{K_I}{\sqrt{2\pi r_c}}f_3}{\tau_s} - \frac{T\sin\beta\cos\beta}{\tau_s}\right)^2 = 1 \quad (3.15)$$

Case II-Debonding initiation at the least distance point of the incident crack to the interface

If interface debonding occurs at the least distance point, it implies $\theta_i = -(\frac{\pi}{2} - \beta)$ as seen in Figure 3.1(a). Let r_i denote the least distance between the incident crack tip and the debonding initiation point, so we can express the original interfacial stress field using equation (2.3), and further get transferred stress field similar to the previous case. Then, based on the proposed strength criteria, we get

$$\left(\frac{\frac{K_I}{\sqrt{2\pi r_i}} f_1'}{\sigma_t} + \frac{\frac{K_{II}}{\sqrt{2\pi r_i}} f_2'}{\sigma_t} + \frac{T\sin^2\beta}{\sigma_t} \right) + \left(\frac{\frac{K_I}{\sqrt{2\pi r_i}} f_3'}{\tau_s} + \frac{\frac{K_{II}}{\sqrt{2\pi r_i}} f_4'}{\tau_s} - \frac{T\sin\beta\cos\beta}{\tau_s} \right) = 1 \quad (3.16)$$

and

$$\left(\frac{\frac{K_I}{\sqrt{2\pi r_i}} f_1'}{\sigma_t} + \frac{\frac{K_{II}}{\sqrt{2\pi r_i}} f_2'}{\sigma_t} + \frac{T\sin^2\beta}{\sigma_t} \right)^2 + \left(\frac{\frac{K_I}{\sqrt{2\pi r_i}} f_3'}{\tau_s} + \frac{\frac{K_{II}}{\sqrt{2\pi r_i}} f_4'}{\tau_s} - \frac{T\sin\beta\cos\beta}{\tau_s} \right)^2 = 1 \quad (3.17)$$

where

$$f_1' = \sum_{11}^{I}(\theta_i, v)\sin^2\beta + \sum_{22}^{I}(\theta_i, v)\cos^2\beta - \sum_{12}^{I}(\theta_i, v)\sin 2\beta \qquad (3.18)$$

$$f_2' = \sum_{11}^{II}(\theta_i, v)\sin^2\beta + \sum_{22}^{II}(\theta_i, v)\cos^2\beta - \sum_{12}^{II}(\theta_i, v)\sin 2\beta \qquad (3.19)$$

$$f_3' = \sum_{12}^{I}(\theta_i, v)\cos 2\beta + (\sum_{22}^{I}(\theta_i, v) - \sum_{11}^{I}(\theta_i, v))\sin\beta\cos\beta \qquad (3.20)$$

$$f_4' = \sum_{12}^{II}(\theta_i, v)\cos 2\beta + (\sum_{22}^{II}(\theta_i, v) - \sum_{11}^{II}(\theta_i, v))\sin\beta\cos\beta \qquad (3.21)$$

If the incident crack is a mode I crack, substituting $K_{II} = 0$ into above equations leads to

$$\left(\dfrac{\dfrac{K_I}{\sqrt{2\pi r_i}} f_1'}{\sigma_t} + \dfrac{T\sin^2\beta}{\sigma_t} \right) + \left(\dfrac{\dfrac{K_I}{\sqrt{2\pi r_i}} f_3'}{\tau_s} - \dfrac{T\sin\beta\cos\beta}{\tau_s} \right) = 1 \qquad (3.22)$$

and

$$\left(\dfrac{\dfrac{K_I}{\sqrt{2\pi r_i}} f_1'}{\sigma_t} + \dfrac{T\sin^2\beta}{\sigma_t} \right)^2 + \left(\dfrac{\dfrac{K_I}{\sqrt{2\pi r_i}} f_3'}{\tau_s} - \dfrac{T\sin\beta\cos\beta}{\tau_s} \right)^2 = 1 \qquad (3.23)$$

After obtaining the least distance r_i from the above equations, one can get the critical

distance

$$r_c = \dfrac{r_i}{\sin\beta} \qquad (3.24)$$

The reason to use the critical distance is that, it is easy to measure in dynamic

experiments.

Experimental investigation

Two kinds of polymeric materials were used in conjunction with two kinds of

optical diagnostic techniques. Homalite–100 was chosen for the photoelasticity

experiments while PMMA (Plexiglas) was used in the Coherent Gradient Sensing (CGS)

experiments (Rosakis et al., 1998). Dynamic photoelasticity is related to the maximum

in-plane shear stresses in a specimen during the loading and failure process. The CGS

technique records the gradient of the first in-plane stress invariant. One wedge-loaded

specimen was used to produce a single, straight dynamic crack as shown in Figure 3.2.

An aluminum wedge was inserted into a pre-notch and impacted by a projectile, causing the wedge to open the notch faces thus producing a single mode I crack. The notch tip was cut using a diamond afering blade (Buehler, Series 15 LC). A strain gauge was bonded onto the wedge to trigger a high-speed camera and laser system. During experiments, a projectile fired from a gas gun was used to apply the impact loading through the wedge. The high-speed camera was employed to record the fringe patterns in real time. More experimental details can be found in Xu et al. (2003).

Results and discussion

Experimental observations and mechanics parameter variations

Figure 3.2 shows a series of CGS images of an incident crack propagating towards an inclined interface (interfacial angle 45 degrees). A vertical line appearing in every image is the camera streak line, which is used for positioning purposes. Another inclined line reveals the position of the interface. A dark circular spot at the upper location is a scaling mark. Interface debonding initiates between 119-122 μs after impact and below the horizontal incident crack path as seen in Figures 3.2(c)(d). This evidence supports the least distance assumption discussed in section 3.3.3. This interfacial crack further propagates along the interface but its upper and right tip is much faster than the lower and left tip, because the energy release rate of the upper tip is higher than that of the lower tip (Xuan et al., 2003). Also, the incident crack features symmetric fringe patterns since it is a mode-I crack, but the fringe patterns of the interfacial crack are not symmetric due to its

mixed-mode nature. Figure 3.3 shows a series of dynamic photoelasticity images of an incident crack propagating towards an inclined interface (interfacial angle 30 degrees). In Figure 3.3(b) a dynamic mode-I crack is seen to propagate towards the interface. Around $t = 161.5\,\mu s$ before the incident crack reaches the interface, we can see interface debonding clearly below the horizontal incident crack path. The interfacial crack continues to propagate on both sides indicated by two small dark dots. Figure 3.4(a) shows crack speed history of the incident crack and the kinked interfacial crack. The mode I incident crack speed is approximately 460 m/s, while the interfacial crack speed is around 800 m/s and is not stable. Fitting photoelasticity fringes leads to history of the stress intensity factors and the T stress of the incident crack, as shown in Figures 3.5(b) and 3.6. We find that K_I is approximately 0.8 $MPa\sqrt{m}$ and it is not surprising to see that K_{II} is close to zero since the incident crack is indeed a mode I crack. We also notice that and the T stress ranges from 1.5 to 2.0 MPa but the path of the incident crack is still stable.
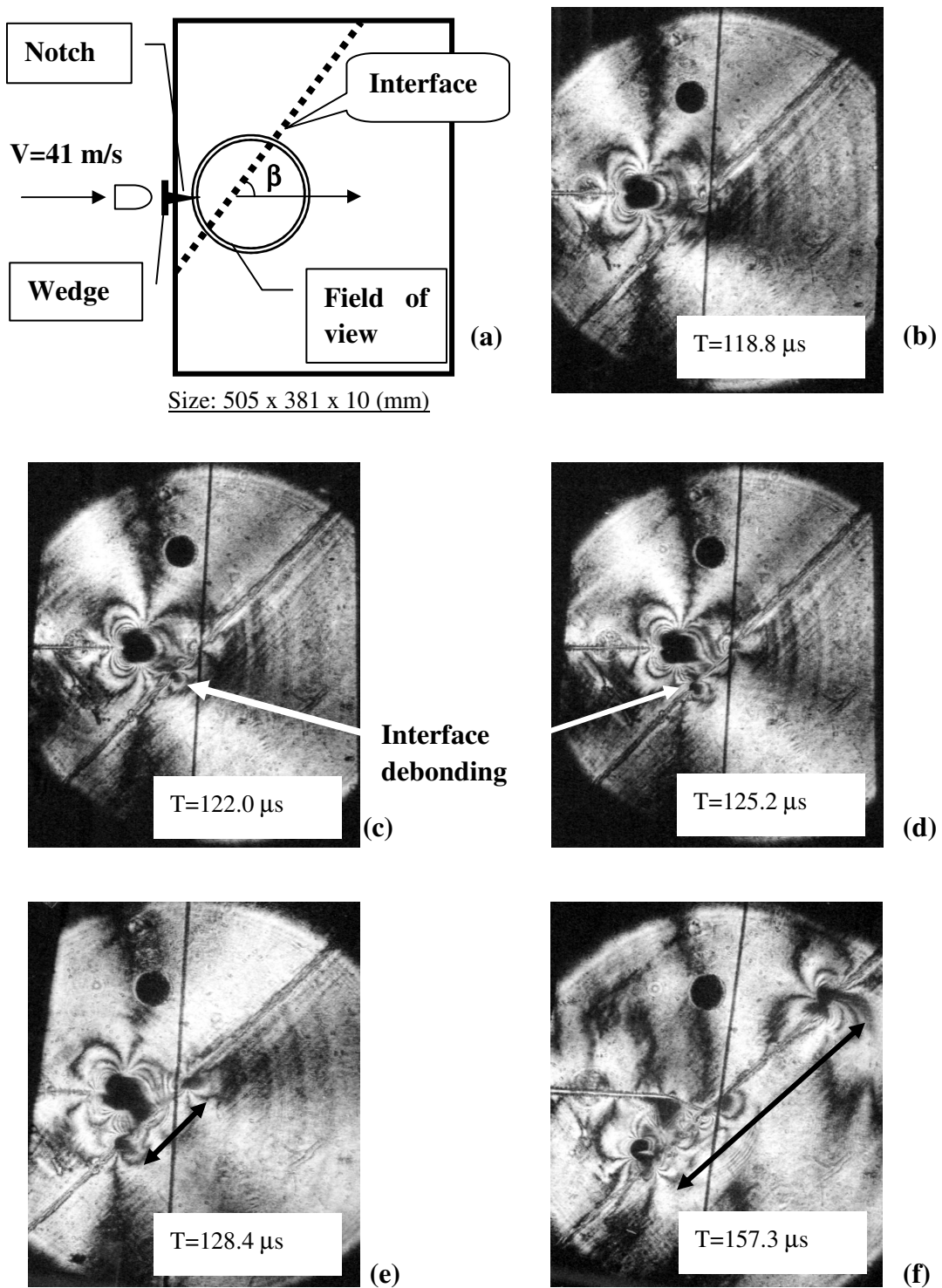
Figure 3.2, Interface debonding in a bonded PMMA plate with an interfacial angle 45^0 (K45PM384-1). Interfacial crack initiates in (c) and (d) and propagates along the interface in (e) and (f). The upper and right tip moves much faster than the lower one.

(a) Size: 505 x 381 x 10 (mm)

Notch

Interface

V=41 m/s

Wedge

Field of view

β

(b) t = 130.3 μs   20mm

Incident crack

30^0

(c) t = 151.1 μs   20mm

r_1
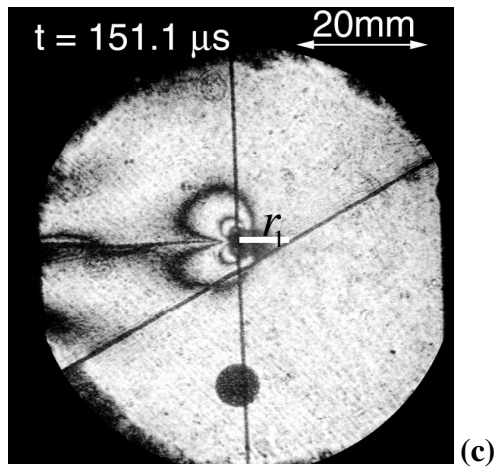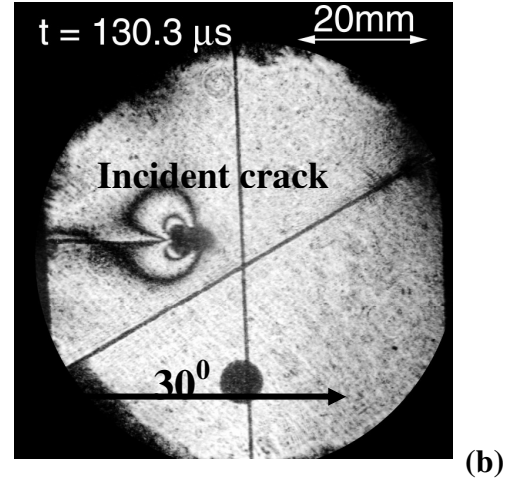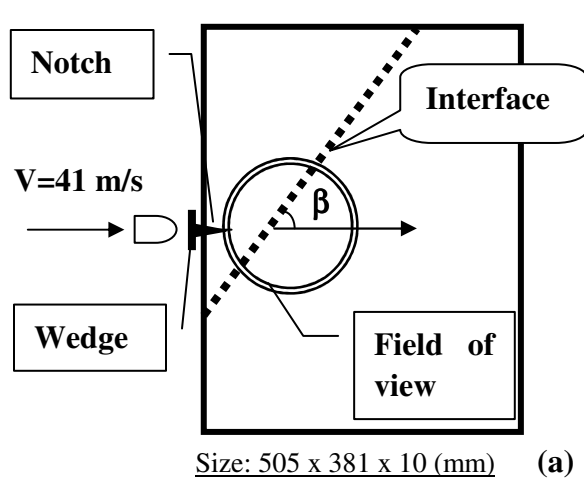
No interface debonding ($r_1 \approx 9.22 mm$)

(d) t = 156.3 μs   20mm

r_2
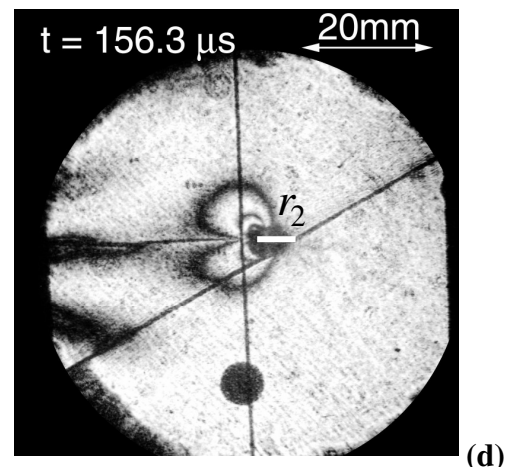
Difficult to judge ($r_2 \approx 6.86 mm$)

(e) t = 161.5 μs   20mm

r_3
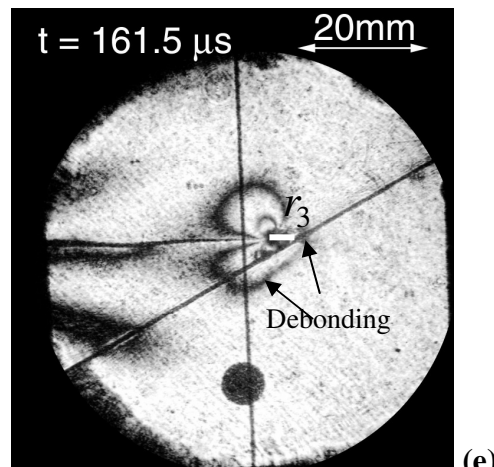
Debonding

Clear interface debonding ($r_3 \approx 4.92 mm$)

(f) t = 166.7 μs   20mm
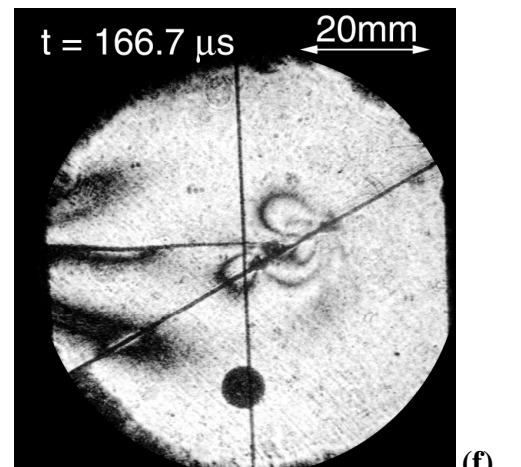
Figure 3.3, Dynamic crack propagation in a bonded Homalite-100 plate (k30hm384-1) and interface debonding ahead of the main mode I crack (interfacial angle 30^0).

(a)

(b)
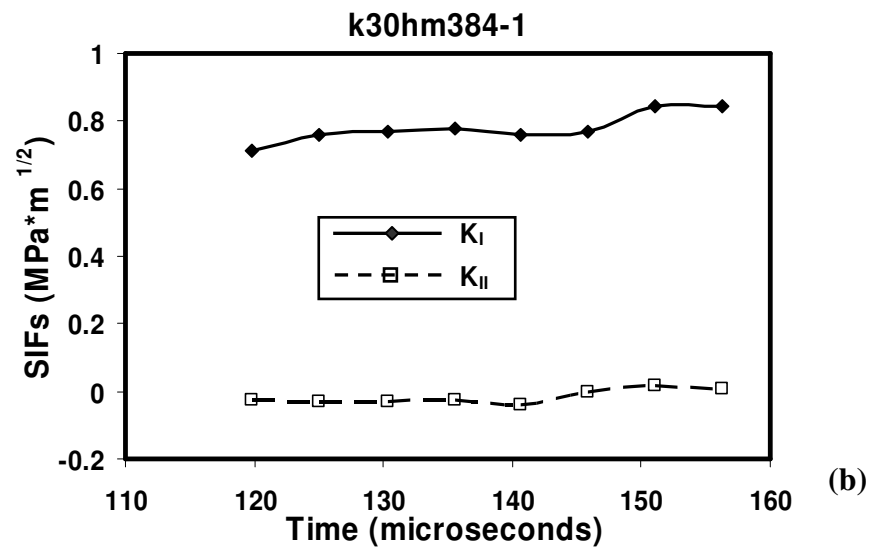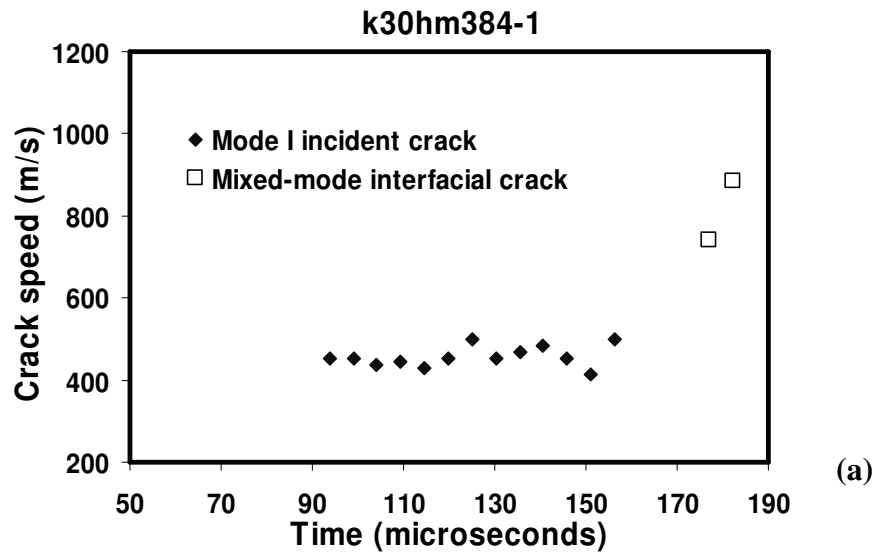
Figure 3.4, (a) Crack speed history of the incident and interfacial cracks; (b) dynamic stress intensity factor (SIFs) history of the incident crack (interfacial angle 30^0).
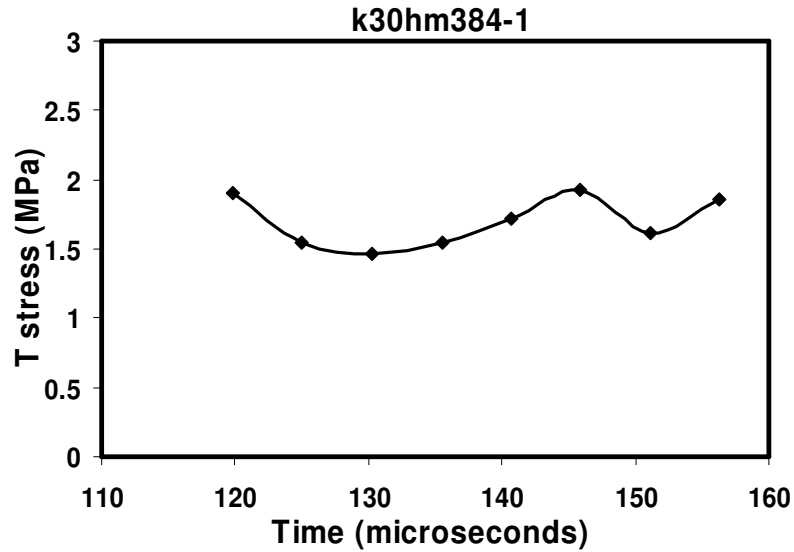
Figure 3.5, Non-singular T stress history of the incident crack (interfacial angle 30^0).

Predications of interfacial debonding initiation ahead of an incident crack

After fitting the stress intensity factors and the T stress of the incident crack, we can predict interfacial debonding initiation using the proposed criteria. Because it is very hard to record the exact moment of interface debonding in dynamic experiments, average values of the stress intensity factors (0.78 $MPa\sqrt{m}$) and the T stress (1.7 MPa) of the incident crack are used. The tensile and shear strengths of the interface were measured by Xu et al., (2003) and they were 6.75 MPa and 7.47 MPa, respectively. For case I (i.e., interface debonding initiates at the intersection point of the incident crack path and the interface), substitution of the above known parameters into equations (3.9) and (3.10) leads to the critical distances r_c=3.6 mm based on strength criterion I, and r_c=2.7mm based on strength criterion II. Similarly, if interface debonding initiates at the least

distance point, strength criterion I gives the least distance r_i=4.5 mm using equation (3.22) and criterion II leads to r_i=3.43 mm using equation (3.23). Based on equation (3.24), these least distances are converted to critical distances, i.e., r_c=9.0 mm for criterion I and r_c=6.86 mm for criterion II. As mentioned before, it is very hard to record the exact moment of interfacial debonding initiation, so direct measurements of the critical distance r_c are almost impossible. However, we can measure the distances between the incident crack tips and the intersection points at the moments, right before and right after interfacial debonding initiation as indicated in Figure 3.3. From the experimental record, at time t=151.1 μs, interfacial debonding initiation did not occur and the corresponding distance r_1 is equal to 9.22 mm. At time t=156.3 μs, we cannot determine whether interfacial debonding initiation occurred or not. As time evolved, clear interface debonding was indicated by two dots at t=161.5 μs and the corresponding distance r_3=4.92 mm. Based on these observations, we estimate that interfacial debonding initiation occurred in the range of 4.92 mm < r_c < 9.22 mm. By comparing direct experimental measurements to analytical predictions, one can easily find that for inclined interfaces, it is not appropriate to assume that interfacial debonding initiation occurs at the intersection point. The least distance assumption gives more reasonable estimations because all the strength criterion predictions based on this assumption are in the measurement range. In the following section, we will only use the least distance assumption for all predictions (i.e., equations (3.22) and (3.23)), and will determine which strength criterion is more reasonable.

Effects of the mechanics parameters of the incident crack and interfacial strengths

Figure 3.6 shows the influence of the stress intensity factor and the T stress of the incident mode I crack, on the critical distance r_c in case II, i.e., the debonding initiates at the least distance point. It is seen that as long as the stress intensity factor increases, the critical distance increases, and when the stress intensity factor is small enough, the critical distance approaches to zero as seen in Figure 3.6(a). Therefore, early interfacial debonding initiation can be suppressed if the stress intensity factor of the incident crack could be controlled as a small value. Xu et al., (2003) followed this principle using controlled impact speed and initial notch radius to lead to crack kinking at the interface, rather than early interface debonding. It is also found that the critical distance predicted using criterion I is always larger than that predicted using criterion II. The surprising result comes from the effect of the T stress as shown in Figure 3.6(b). The T stress is a constant stress along the incident crack path and is related to far-field loads. For a plate with a central crack, which is subjected to remote uniform applied stresses σ_{11}^{∞} and σ_{22}^{∞}, the T stress of the central crack is (Rice, 1974)

$$T = \sigma_{11}^{\infty} - \sigma_{22}^{\infty} \tag{3.25}$$
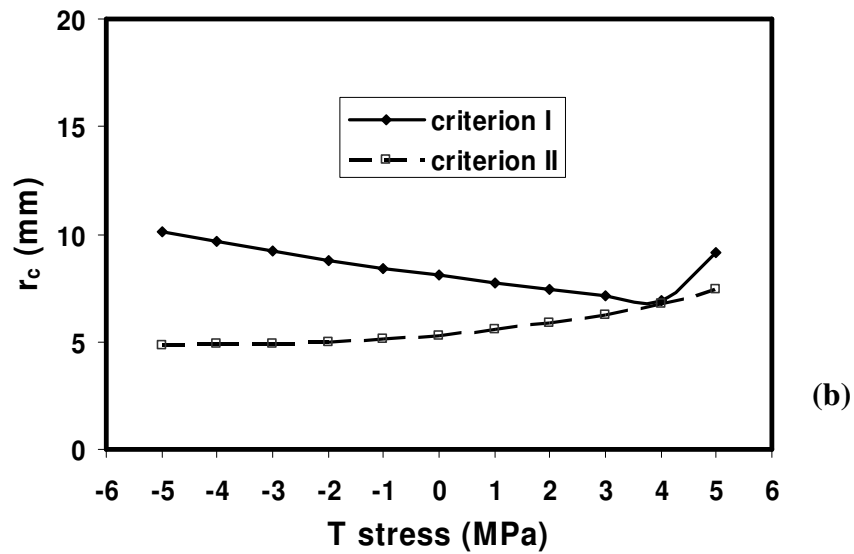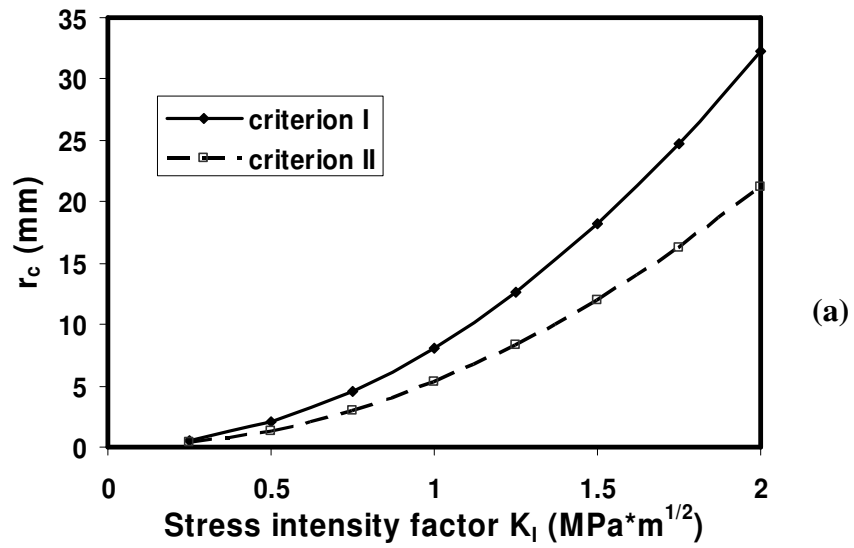
Figure 3.6, Variations of the critical distance r_c with (a) stress intensity factor K_I (T=0 MPa, V/Cs=0.4); and (b) T stress (K_I= 1.0 MPa*m$^{1/2}$, V/Cs=0.4) for a case of an interfacial angle β=30^0.

If the T stress is positive, it will lead to interface debonding easier and the critical distance r_c should increase because of the tensile stress acting at the interface. If the T stress is negative, the critical distance r_c should decrease. In Figure 3.6(b), predictions made by criterion II are in agreement with this trend, but there is some discrepancy for criterion I. When the T stress is negative, the critical distance increases with the increase of the absolute T stress values. Therefore, criterion II is more reasonable than criterion I, and we will use criterion II only in all other predictions.

(a)
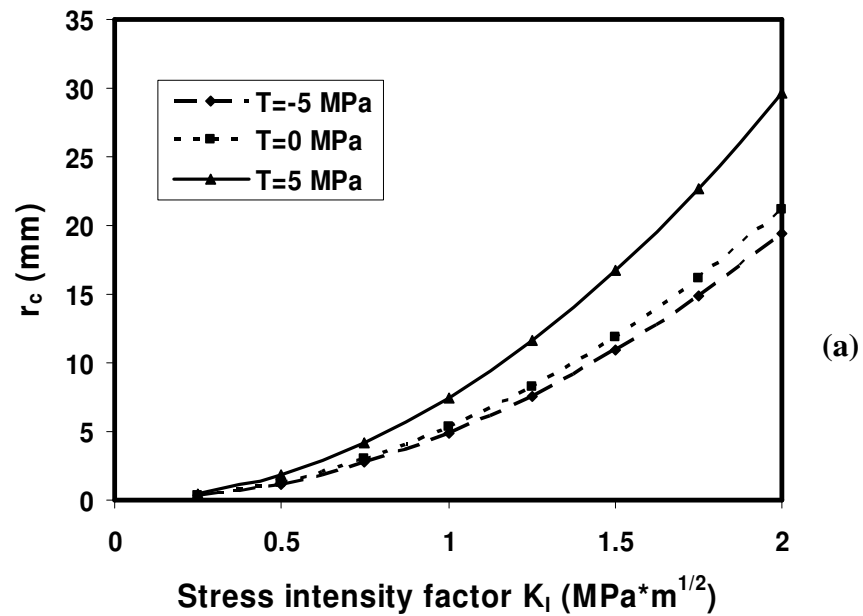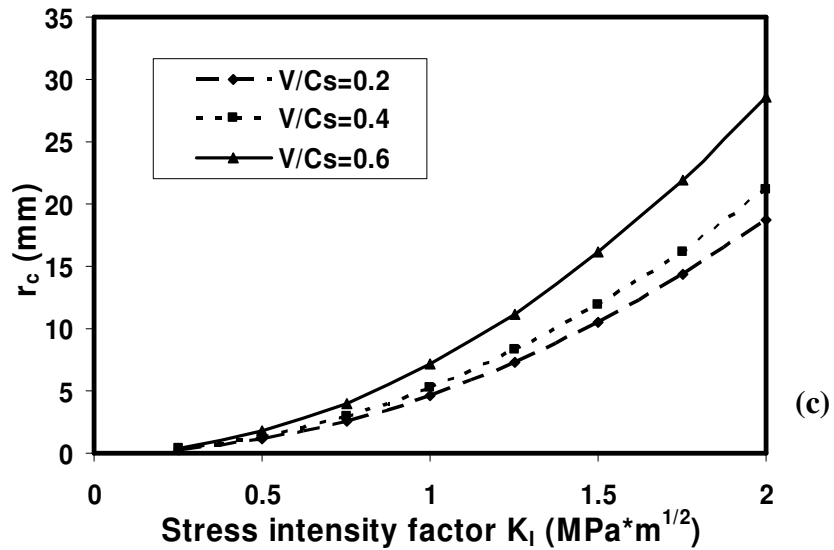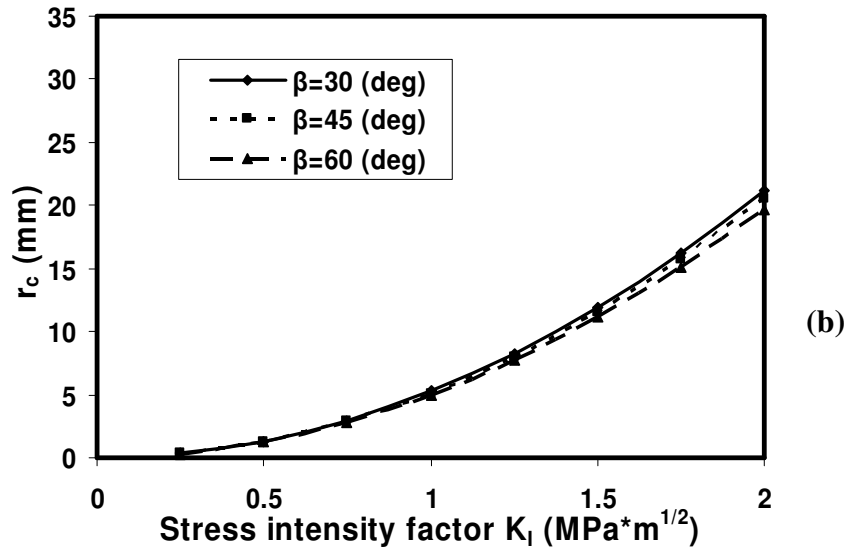
Figure 3.7, Variations of the critical distance r_c predicted using criterion II with the stress intensity factor K_I under the conditions of (a) V/Cs=0.4, $\beta=30^0$ for different levels of the T stresses; (b) V/Cs=0.4, T=0 MPa for different interfacial angles; (c) $\beta=30^0$, T=0 MPa for different crack tip speeds.
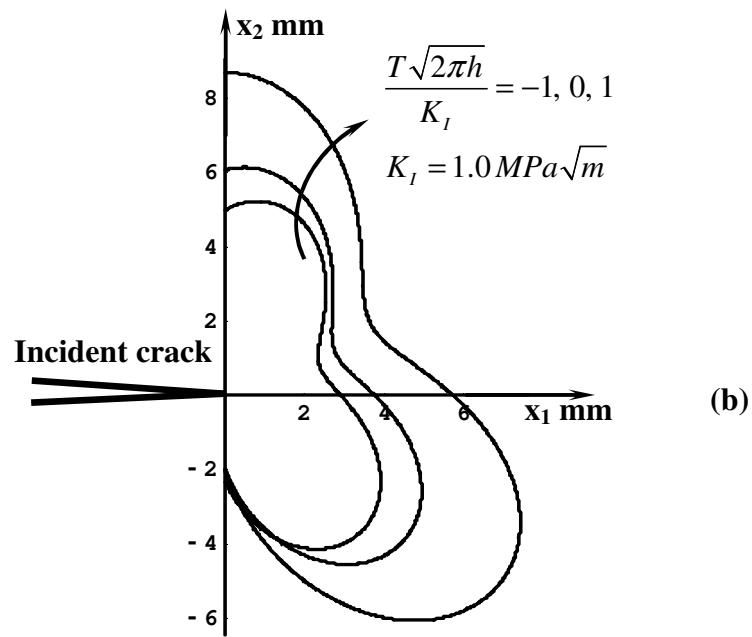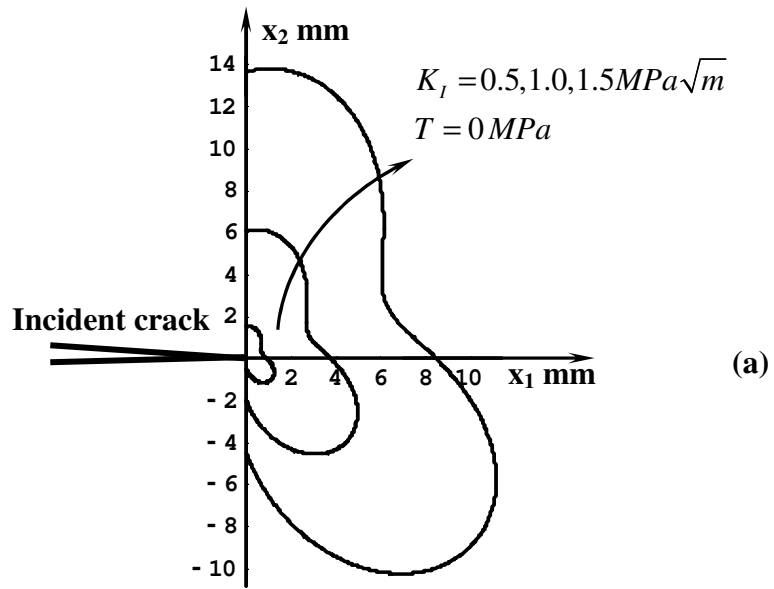
Figure 3.8, Effects of (a) the stress intensity factor and (b) the T stress on the shape of the failure envelope.
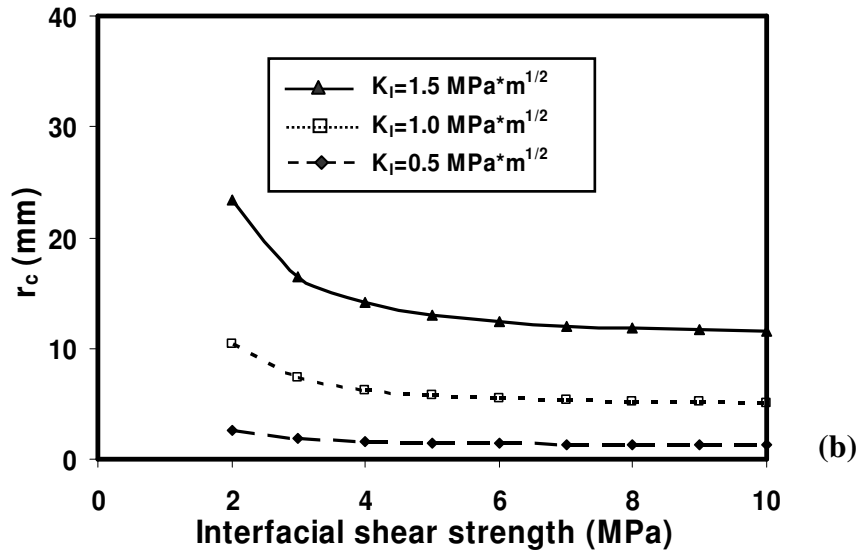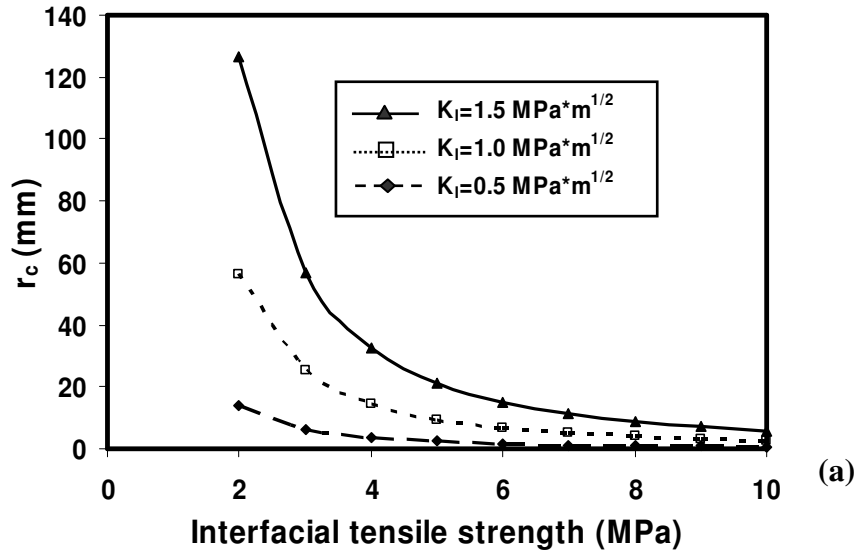
Figure 3.9, Variations of the critical distance r_c with (a) interfacial tensile strength (fixed shear strength τ_s=7.47 MPa); and (b) interfacial shear strength (fixed tensile strength σ_t=6.75 MPa) for different levels of stress intensity factors under the conditions of V/Cs=0.4, β=30^0, T=0 MPa.

Figure 3.7(a) further shows the critical distance variations with the stress intensity factor for different levels of the T stresses. For the same stress intensity factor and other parameters, the critical distance under T=5 MPa is much larger than that under T=-5 MPa. So changing the T stress (i.e., changing external loading along the incident crack path) is an efficient way to control interfacial debonding initiation. Meanwhile, interfacial angles and incident crack tip speeds also have some effects on interfacial debonding initiation. When the stress intensity factor of the incident crack is small, their effects can be neglected as seen in Figures 3.7(b)(c). However, when the stress intensity factor is in the higher range, smaller interfacial angles and higher incident crack tip speeds lead to larger critical distances as shown in Figures 3.7(b)(c).

As mentioned before, the stress intensity factor of the incident crack plays a critical role in leading to early interfacial debonding initiation and with the increase of the stress intensity factor, the critical distance increases significantly. This is also indicated by the shape change of the governing failure envelope as shown in Figure 3.8(a). The failure envelop represents two-dimensional distributions (based on equation (3.23)) of the critical distances using the measured interface strengths in section 3.5.2. As the stress intensity factor increases, the failure envelope moves far away from the crack tip. This indicates interfacial debonding initiation will occur more easily. The nonsymmetrical shape of the failure envelope results from the basic assumption of the right and inclined location of the interface. Figure 3.8(b) shows the T stress effect on the shape change of the governing failure envelope. Obviously, negative T stress tends to suppress interfacial

debonding initiation (small envelop), and positive T stress leads to early interfacial debonding initiation (large envelope).

Also, interfacial strength is an important parameter to govern interfacial debonding initiation based on our proposed criteria. To clarify its effect on interfacial debonding initiation, and to examine which interfacial strength is more critical, variations of the critical distances with the interfacial tensile and shear strengths are shown in Figure 3.9. Obviously, as increase of the interfacial tensile or shear strength, the critical distance decreases. Moreover, as shown in Figure 3.9(a), the critical distance decreases sharply with increase of the interfacial tensile strength. However, different shear strength values do not lead to much difference in the critical distances as seen in Figure 3.9(b). Therefore, the interfacial tensile strength is much more important than the interfacial shear strength to control interfacial debonding initiation in this case (a mode I incident crack). Although the above results are based on bonded polymer systems, they are expected to extend to bi-material systems. For example, high stress intensity factors of the incident cracks and low interfacial tensile strengths will obviously induce early interfacial debonding initiation in bi-material systems.

CHAPTER IV

CONVEX INTERFACE JOINTS WITH LEAST STRESS SINGULARITY IN
DISSIMILAR MATERIALS

Introduction

Dissimilar material joints/bonds have been extensively used in modern engineering

fields, such as adhesive joints of two kinds of dissimilar materials, fiber/matrix interfaces

of advanced composite materials, among others. It is found that the failure of these

material systems often initiates at the interface corners or free edges. The reason is that

very high stresses are developed near the free edges under external loading. Therefore,

reducing local stress levels near the free edges may result in higher joint strengths of

dissimilar materials. On the other hand, interfacial strength is a very important parameter

for material designs and evaluations. For example, in chapter III, it is found that

interfacial strength has a significant influence on interface debonding ahead of a primary

crack; and modern computational mechanics tools, such as cohesive zone modeling, need

interfacial strengths and toughnesses for specific mechanics simulations (Wappling et al.,

1998; Li et al., 2002; Roychowdhury et al., 2002; Roe and Siegmund, 2003; Tvergaard,

2004). However, researchers have shown that stress singularities (stresses tending to

infinity based on elasticity solutions) exist at the corners of bi-material interfacial joints

due to high material property mismatch (Williams, 1952; Bogy, 1971). The presence of

free-edge stress singularities at bi-material corners makes macro-scale interfacial strength

measurement a big challenge (Reedy and Guess, 1993; Akisanya and Fleck, 1997; Tandon, et al., 1999).

Hence, in order to evaluate intrinsic interfacial strengths or to improve load capacity of dissimilar materials, reduction or elimination of the free-edge stress singularities is essential. Very recently, Xu et al. (2004) have proposed a convex design for dissimilar material joints with reduced free-edge stress singularities. In their study, planar convex and straight-edged metal/polymer joints were tested under quasi-static loading conditions using in-situ photoelasticity. Their experimental results incorporating with finite element analysis show that a pair of specific convex joints can efficiently remove the free-edge stress singularities for most engineering material combinations. As a result, a quite uniform stress distribution along the interface is obtained.

However, it should be noticed that in their planar convex specimens, the free-edge stress singularity still exists at the straight free-edge along the width direction, although the stress singularity at the free-edge along the thickness direction is removed.   In order to solve this problem, a planar convex specimen could be "rotated" to form an axisymmetric convex configuration, just like a bamboo joint. This axisymmetric convex joint is obvious to provide more reasonable interfacial strength measurements but it still needs further validation. Besides, the dynamic response of the convex joint has not yet been studied in the previous work (Xu et al., 2004). Therefore, in this investigation, the planar convex interfacial design is extended to axisymmetric configurations, and both quasi-static and dynamic response of the new axisymmetric convex joint will be

evaluated. For comparison, conventional straight-edged joints of dissimilar materials commonly used in current test standards are taken as the baseline. Furthermore, to show the disappearance of the free-edge stress singularities in convex joints, the stress states across bi-material interfaces will be examined using finite element analysis. In the following section, before all experimental and numerical studies are expanded, detailed theoretical background will be reviewed for design guidance.

Theoretical background

Free-edge stress singularities in dissimilar material interfaces/joints

As illustrated in Figure 4.1(a), a butt-joint specimen was used to demonstrate the free-edge stress singularity in steel 4340 and Plexiglas (polymethyl methacrylate or PMMA) joints (Xu et al., 2002). Significant stress concentrations (physical phenomena) resulting from stress singularities (theoretical elasticity results) were found at the bi-material corners using the coherent gradient sensing (CGS) technique, which was developed by Tippur et al. (1991) for full-field mechanical-optical measurements. The CGS fringe patterns correspond to the gradients of $\sigma_{xx}+\sigma_{yy}$. It is indeed this stress concentration that leads to free-edge debonding, especially when the joint is subjected to dynamic loading.

Butt-joint tensile tests
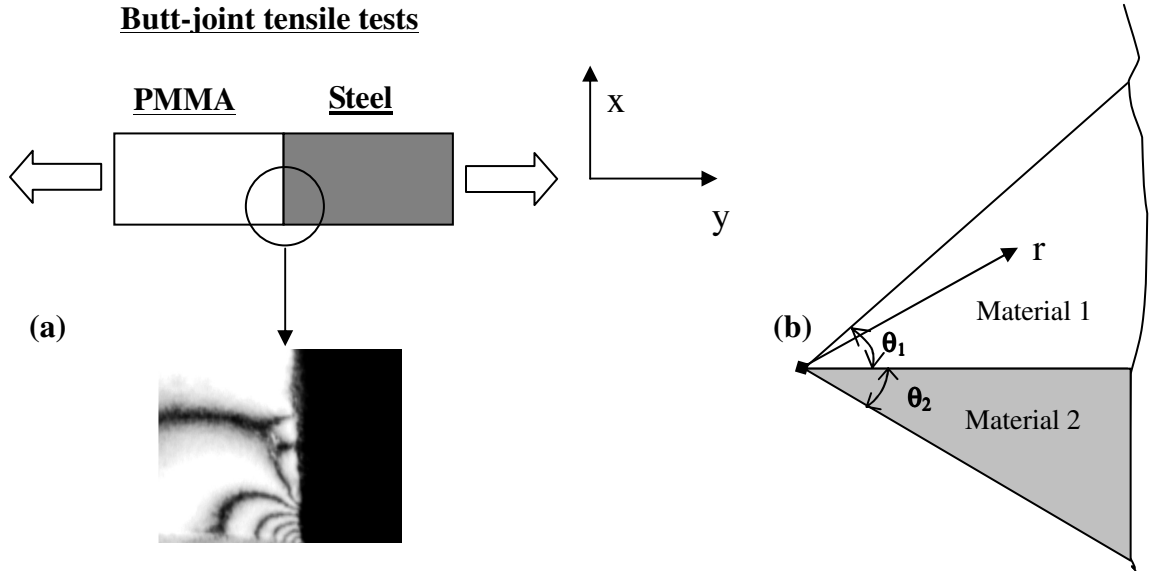
Figure 4.1, (a) Coherent gradient sensing (CGS) photographs showing strong stress concentrations (associated with fringe concentrations) at the free edges of bonded metal/polymer joints subjected to tensile loading (Xu et al., 2002); (b) Angular definition of a bi-material wedge.

For some specific bi-material corners or edges, Williams (1952), Bogy (1971), Hein and Erdogan (1971), Munz and Yang (1993), Pageau et al. (1996), and Akisanya and Meng (2003), to name a few, have shown that stress singularities exist. The asymptotic stress field of a bi-material corner can be expressed by

$$\sigma_{ij}(r,\theta) = \sum_{k=0}^{N} r^{-\lambda_k} K_k f_{ijk}(\theta) , \qquad (i, j = 1, 2, 3), \qquad (4.1)$$

where $f_{ijk}(\theta)$ is an angular function and K_k is also known as the "stress intensity factor". The fracture mechanics terminology "stress intensity factor" is used in interfacial mechanics to characterize a similar stress singularity problem. It should be noticed that,

for an interfacial fracture problem (assuming initial debonding), the stress singularity at a crack tip is intrinsic and cannot be removed. However, the stress singularity in an interfacial strength investigation (assuming perfect bonding) can be removed through appropriate designs (Chue and Liu, 2002; Xu et al., 2004). The stress singularity order λ may be real or complex. Here, we did not use other singularity order forms such as λ-1, because the value of λ can be easily ascertained by the readers. Also, it is conveniently compared to the singularity order -0.5 of a crack based on linear elastic fracture mechanics (LEFM). As seen from equation (4.1), the theoretical stress values will become infinite as r (defined in Figure 4.1(b)) approaches zero, if λ has a positive real part. This leads to a problem referred to as the "stress singularity problem". It is the presence of this stress singularity that leads to erroneous results in current interfacial strength measurements, besides being responsible for free-edge debonding or delamination in dissimilar material joints. However, if λ has a non-positive real part, then the stress singularity disappears. Bogy (1971) found that the stress singularity was purely determined by the material property mismatch and two joint angles of the bi-material corner θ_1, θ_2 (defined in Figure 4.1(b)). Generally, the material property mismatch can be expressed in terms of the Dundurs parameters α and β, which are two non-dimensional parameters computed from the elastic constants of two bonded materials (Dundurs, 1969):

66

$$\alpha = \frac{\mu_1 m_2 - \mu_2 m_1}{\mu_1 m_2 + \mu_2 m_1} \quad , \tag{4.2}$$

$$\beta = \frac{\mu_1(m_2 - 2) - \mu_2(m_1 - 2)}{\mu_1 m_2 + \mu_2 m_1} \quad . \tag{4.3}$$

Here, μ_1 is the shear modulus of material 1, μ_2 is the shear modulus of material 2, $m = 4(1 - \nu)$ for plane strain, ν is the Poisson ratio, and $m = 4/(1 + \nu)$ for plane stress. The stress singularity order is related to material and geometric parameters, and is determined by a characteristic equation of coefficients $A(\theta_1, \theta_2, p)$ through $F(\theta_1, \theta_2, p)$:

$$f(\theta_1, \theta_2, \alpha, \beta, p) = A\beta^2 + 2B\alpha\beta + C\alpha^2 + 2D\beta + 2E\alpha + F = 0, \tag{4.4}$$

where $p = 1 - \lambda$. A, B, C, D, E, and F have been defined by Bogy (1971). Therefore, varying these four independent parameters $(\theta_1, \theta_2, \alpha, \beta)$, one can obtain a negative real part of the stress singularity order λ. So the stress singularity will be removed and the stress distribution close to the free edge will become smooth.

Convex interfacial joints for the least free-edge stress singularity

The first step to establish a uniform stress state at the interface is to reduce or eliminate the stress singularity at the bi-material edge. If material 1 is a typical soft material and material 2 is a hard material as shown in Figure 4.1(b), a convex interfacial design with two joint angles $\theta_1 = 45^0$ and $\theta_2 = 65^0$ can remove free-edge stress singularities for a wide range of current engineering materials (Xu et al. 2004). This result is illustrated in Figure 4.2 showing the entire possible range of two Dundurs'

parameters. We can see that for this specific pair of joint angles, the stress singularity is

limited to a very small zone near $\alpha \cong 1$. These material joint combinations are quite rare

in engineering applications since they represent extremely high mismatch in Young's

moduli. In the following section, this specific angle combination is applied to

axisymmetric joint configurations. To demonstrate the zero stress singularity in

axisymmetric convex joints, both experimental and numerical investigations are

conducted to understand the mechanics insight.
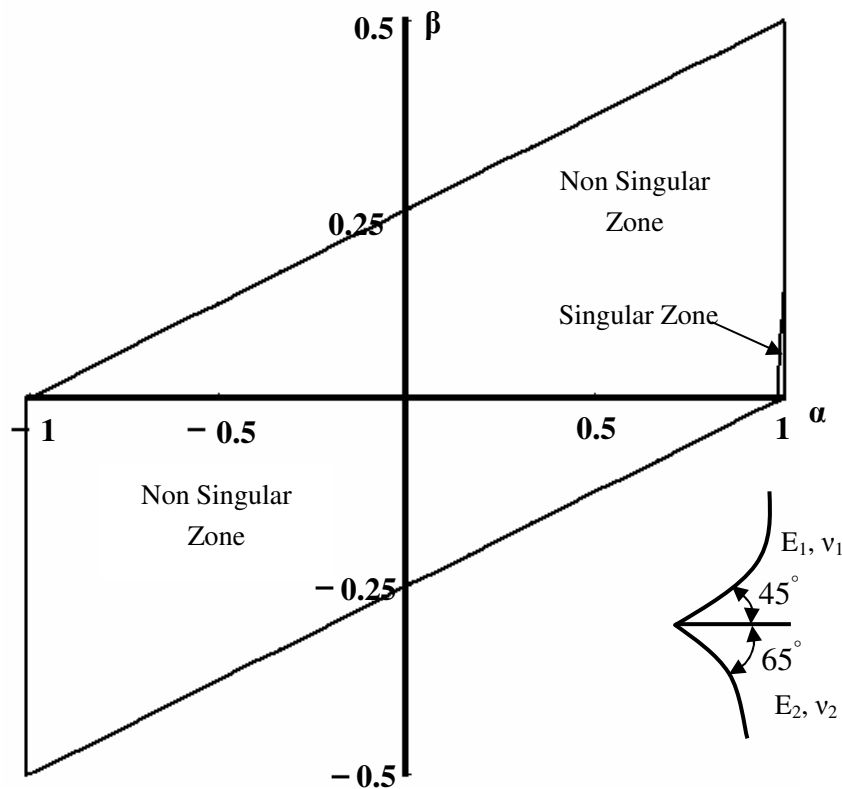
Figure 4.2, Stress singularity order λ as a function of two Dundurs parameters for a proposed pair of joint angles (45 and 65 degrees for soft and hard materials, respectively). A very small singular zone implies the given pair of angles is applicable for a wide range of engineering material combinations (Xu et al., 2004).
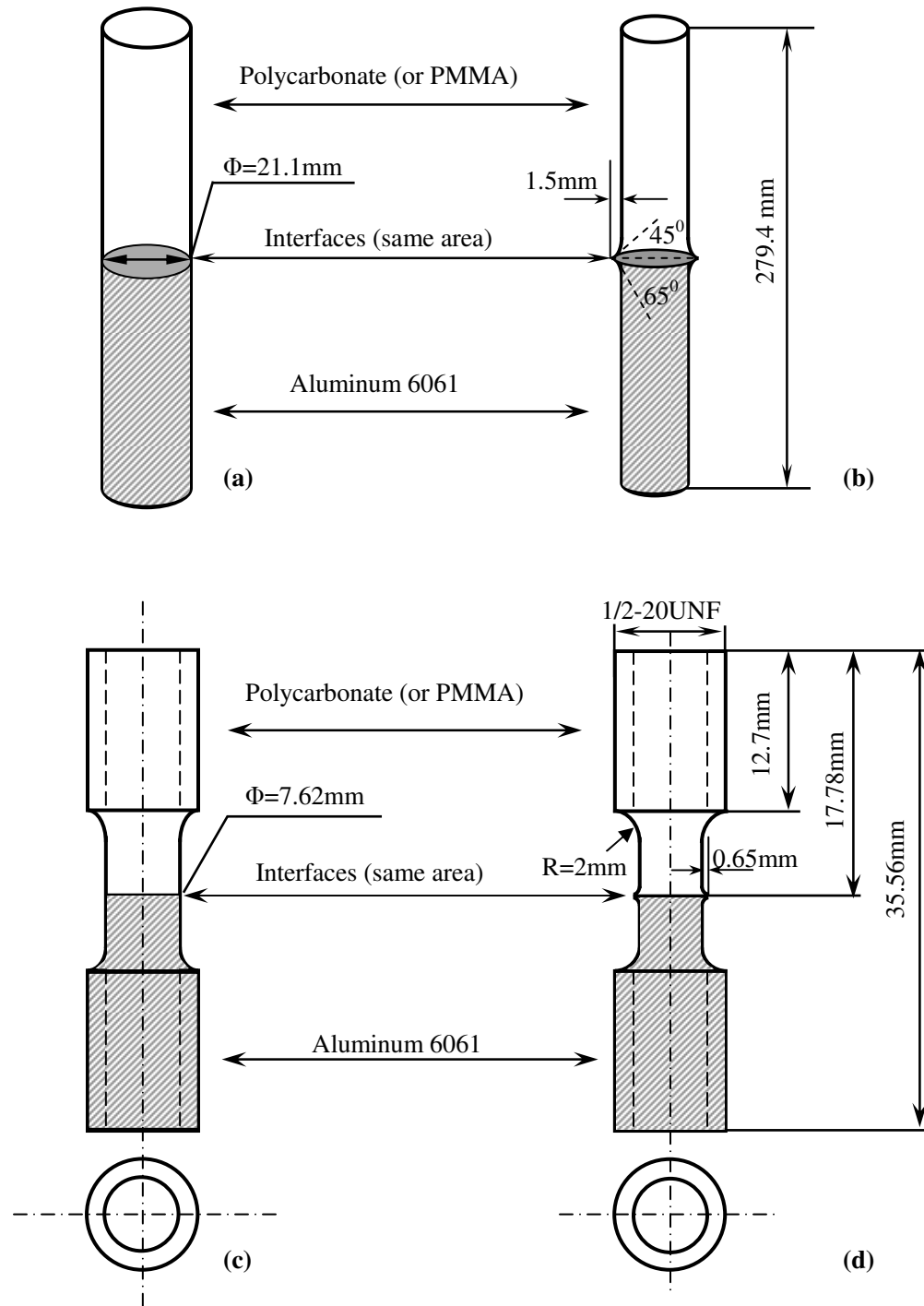
Figure 4.3, Schematic illustrations of (a) baseline and (b) convex specimens for quasi-static experiments; (c) baseline and (d) convex specimens for dynamic experiments.

Experimental investigation

Specimen design and preparation

Two types of specimens were designed and prepared for comparison, as seen in Figure 4.3. The straight-edged specimen is the baseline for comparison. Test materials were PMMA, polycarbonate, and aluminum. Two groups of material combinations were tested: (i) PMMA and aluminum; (ii) polycarbonate and aluminum. A commercial epoxy (Weld-on 10, Meyer Plastics Inc., Santa Ana, CA) was used as the bonding agent. The reason to choose this particular adhesive is that its properties are very close to those of PMMA or polycarbonate (Tippur et al., 1991). Hence, the possible involvement of a third material in a typical bi-material problem was removed. The adhesive had two components, A and B. They were mixed before bonding and cured at room temperature for at least four hours. Before the adhesive bonding, bonding areas were sand-blasted and cleaned using acetone. A special fixture was designed to bond these specimens. Alignment of these specimens was carefully examined during the bonding process. The quasi-static specimens were cylindrical with 21.1 mm in diameter (0.83 inch) and 279.4 mm in height (11 inches) as illustrated in Figures 4.3(a), (b). In order to make a fair comparison, the jointed interfacial areas of the straight and convex joints were the same (349.67 mm^2).

Dynamic experiments were conducted using a split Hopkinson tension bar. In a valid Hopkinson bar test, two important conditions must be met (Myers, 1994; Gama et al., 2004). First, the wave propagation within the tensile bar must be one-dimensional.

Second, the specimen must deform uniformly. The first condition can be satisfied by limiting the impact velocity and by using a proper length-to-diameter ratio of the tensile bar. To achieve dynamic stress equilibrium in the specimens, the loading pulse should travel back and forth inside the specimen more than three times (Chen et al., 1994; Ravichandran and Subhash, 1994; Yang and Shim, 2005). Hence, short and small specimens should be used in dynamic experiments to facilitate dynamic stress equilibrium (Chen et al., 2002). Figures 4.3(c) and (d) show the dimensions of two types of specimens used in dynamic tensile tests. The jointed interfacial area of both straight and convex joints for Hopkinson bar specimens was 45.6 mm^2. Preparation process of dynamic specimens was the same as that of static specimens.

Experimental techniques

Quasi-static experiments were conducted using a hydraulically driven materials test system (MTS 810). During a quasi-static tension test, the cylindrical specimen was placed between the two lubricated wedges installed in two grips. The main control mode was displacement control and the loading rate was 1 mm/minute. The loading history was recorded by a computer through a digital controller. The nominal static interfacial strength is defined by the failure load divided by the cross sectional area of the interface.

Split Hopkinson bars are mainly used to determine the dynamic stress-strain response of materials under high strain-rate conditions (Gilat and Cheng, 2000; Lee et al., 2000; Chen et al., 2002; Huh et al., 2002). In a Hopkinson experiment, the incident and

reflected pulses are recorded by a strain gauge attached to the incident bar, and the transmitted pulse is recorded by another strain gauge attached to the transmission bar (see Figure 4.4(a)). From the transmitted signal, one can also find the dynamic strength of the specimen corresponding to the peak value of the transmitted signal (Yokoyama, 2003; Wang and Ramesh, 2004). For the specimen with a bi-material interface, let ε_t denote the time-resolved axial strain in the transmission bar with cross sectional area A_t and Young's modulus E_t. Assuming that the incident and transmission bars are deformed uniformly and the specimen is under the condition of dynamic equilibrium, the force in the transmission bar can be obtained from the relation

$$F = A_t E_t \varepsilon_t . \tag{4.5}$$

So the maximum load that can be transferred by the specimen is

$$F_{\max} = A_t E_t (\varepsilon_t)_{\max} , \tag{4.6}$$

where $(\varepsilon_t)_{\max}$ is the peak value of the transmitted pulse. Therefore, based on the dynamic equilibrium condition, the nominal dynamic interfacial strength of the specimen can be expressed as

$$\sigma_t = \frac{F_{\max}}{A_I} = \frac{A_t}{A_I} E_t (\varepsilon_t)_{\max} . \tag{4.7}$$

Here, A_I is the cross sectional area of the bi-material interface.
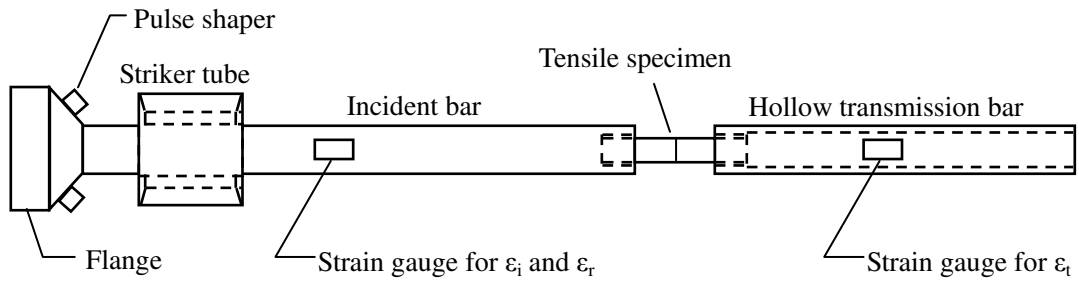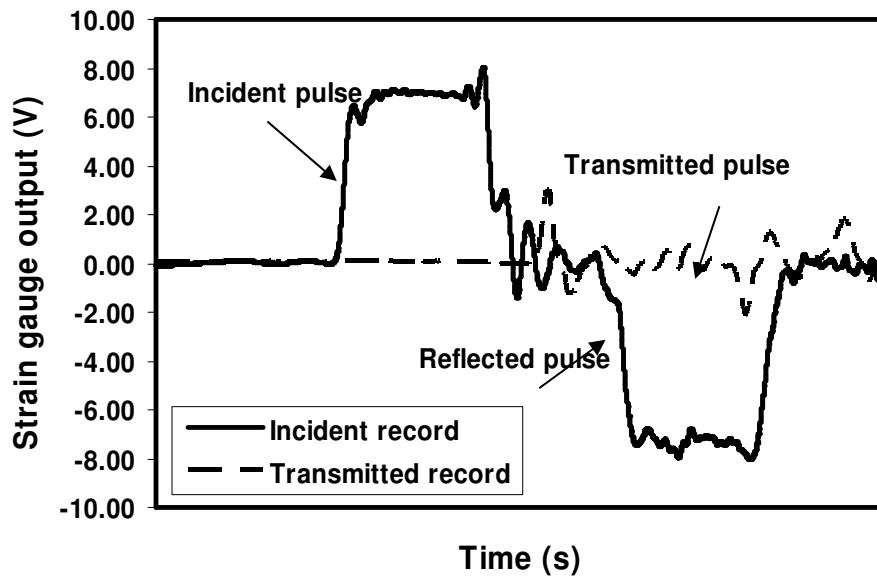
Figures 4.4, (a) Schematic illustration of a modified split Hopkinson tension bar (Chen et al., 2002); (b) A typical oscilloscope record of a dynamic tensile experiment.

In our dynamic experiments, a conventional split Hopkinson tension bar was modified to capture the weak signals transmitted from the low impedance specimens as described in Chen et al. (2002). Instead of the conventional steel transmission bar, a hollow circular tube made of high-strength aluminum alloy was used to increase the magnitude of a weak transmitted signal (see Figure 4.4(a)). The tensile specimen was held between the incident and transmission bars by thread connections to the bar ends. In this setup, the striker was a tube sliding outside the incident bar. The working principle of such a setup is well documented. A typical experimental record is shown in Figure 4.4(b). It can be seen that all signals are clearly recorded, which indicates the efficiency of the modification. It is also noticed that the incident and reflected signals are much higher than the transmitted signal.

Numerical analysis

Unlike planar specimens (Xu et al., 2004), photo-elasticity cannot be applied for real time measurements in axisymmetric configurations, therefore, numerical simulations are quite helpful for stress distributions. Elastic finite-element analysis (FEA) of the baseline and convex joint specimens under both static and dynamic loading was carried out using the commercial software Abaqus 6.4. Due to the similarity between the aluminum/polycarbonate and aluminum/PMMA joints, we only modeled the aluminum/polycarbonate joint subjected to static loading. The material constants of aluminum were chosen as Young's modulus E=71.1 GPa, Poisson's ratio v=0.33 and

density ρ=2780 kg/m^3, and for polycarbonate, E=2.4 GPa, v=0.34, ρ=1200 kg/m^3 (Xu and Sengupta, 2004). To simplify the analysis, an axisymmetric model was constructed using axisymmetric elements and the bonded interfaces were tied together in the numerical model. External load was applied at the polycarbonate end and the aluminum end was fixed.

A dynamic stress analysis was conducted for both straight and convex aluminum/PMMA joints. From the experimental record in Figure 4.4(b), we can see that the shapes of the incident and reflected signals are approximately rectangular. Furthermore, in this analysis, we focused on the effect of different joint shapes on the stress distributions across the interfaces. Hence, an external rectangular stress pulse of 1 MPa was directly applied at the aluminum end in the modeling while the PMMA end was fixed. The load duration time was set to be 5 μs and the total analysis time was 50 μs. Then the stress distribution across the joint interface was extracted from numerical simulations. The material properties of PMMA were E=5.6 GPa, v=0.35, ρ=1190 kg/m^3 (Singh et al., 1997; Kimberley and Lambros, 2004).

Results and discussion

Quasi-static test results

Four sets of static specimens were tested and each set had eight specimens. They were categorized into two groups for comparison. One group was the aluminum/PMMA

joint and the other was the aluminum/polycarbonate joint. The final failure strength results for aluminum/PMMA and aluminum/polycarbonate joints are shown in Table 4.1 and illustrated in Figure 4.5. For aluminum/PMMA joints, the average interfacial strength for the straight joint specimens is 11.35MPa. With the same cross sectional area, the average interfacial strength for the convex joints is 12.84 MPa, an increase by 13.13% over that of the straight joints. For aluminum/polycarbonate joints, the change in strengths is even larger. The average interfacial strength for the convex joints is around 22.36% higher than that of the straight joints. Therefore, the advantage of using convex joints to improve load transfer capacity is quite clear. The failure load capacity increase results from the elimination of free-edge stress singularities in the convex joint specimens, which will be discussed in the following numerical analysis. Another benefit of the new design is that for the same jointed interface area, the material volume of the convex configuration is reduced at least 18%. Besides failure load increasing, convex joints will lead to accurate interfacial strength measurements.

As interfacial mechanical properties are intrinsic in nature, they are solely determined by the atomic structure and chemistry of the interfacial region (Swadener et al., 1999). However, the interfacial strength based on the conventional measurements is not a material constant due to the free-edge stress singularities, according to some recent investigations (Reedy and Guess, 1993). This is also indicated by comparing the previous test results (Xu, et al., 2004) to the current test results as shown in Table 4.2. The two types of specimens used in previous investigation are illustrated in Figure 4.6(a), (b) and

the two types of specimens used in current investigation are shown in Figure 4.6(c), (d). For straight-edged aluminum/PMMA joints, the nominal tensile strengths of the different geometries are totally different (see the first row in Table 4.2), although they were bonded with the same adhesive. The nominal interfacial strength of the planar specimens is 5.9 MPa whereas that of the axisymmetric specimens is as high as 11.35 MPa. The same trend also existed in straight-edged aluminum/polycarbonate joints. The nominal interfacial strengths of the planar and axisymmetric specimens are 5.3 MPa and 8.9 MPa, respectively.

For convex-edged aluminum/PMMA joints, the average strength value is 10.1 MPa for planar specimens (Figure 4.6(b)) and 12.84 MPa for axisymmetric specimens (Figure 4.6(d)). The reason for some strength difference is straightforward: in planar convex specimens, the free-edge stress singularity still exists at the straight free-edge along the x-direction, although the stress singularity at the free-edge along the z-direction is removed. However, no singularities exist in axisymmetric convex specimens, which will be verified by the following numerical results. These results explain why the average strength of the axisymmetric convex specimen is higher than that of the planar convex specimen. On the other hand, we also notice that for convex aluminum/polycarbonate joints, the strength difference between the thick planar specimen and the axisymmetric specimen is quite large. Because for the thick planar specimens, the singular stresses at the straight edge along the x-direction (Figure 4.6(b)) play a major role in interfacial failure. Hence, the current axisymmetric convex specimens provide very reasonable

strength data and they are all much higher (at least twice) than the butt-joint specimens

(see Figure 4.1(a) or Figure 4.6(a)) used in current test standards.

Table 4.1. Static tensile test data for bi-material joints (Interface area: 349.67 mm^2)

Joint materials	Joint angles (metal-polymer)	Tensile strength (MPa)	Change of strength	Standard deviation (MPa)
Aluminum-PMMA	90^0-90^0 (baseline)	11.35	0%	2.53
Aluminum-PMMA	65^0-45^0	12.84	+13.13%	2.53
Aluminum-Polycarbonate	90^0-90^0 (baseline)	8.90	0%	2.39
Aluminum-Polycarbonate	65^0-45^0	10.89	+22.36%	1.32

Table 4.2. Comparison of interfacial tensile strengths using different configurations

Joint materials	Joint angles (metal-polymer)	Nominal interfacial tensile strength (MPa)	
		Planar specimens (Xu et al. 2004)	Axisymmetric specimens
Aluminum-PMMA	90^0-90^0 (baseline)	5.9 ± 1.2	11.35 ± 2.53
Aluminum-PMMA	65^0-45^0	10.1 ± 1.4	12.84 ± 2.53
Aluminum-Polycarbonate	90^0-90^0 (baseline)	5.3 ± 1.4 (thick specimens)	8.90 ± 2.39
Aluminum-Polycarbonate	65^0-45^0	5.6 ± 1.5 (thick specimens)	10.89 ± 1.32

Note: The thickness of thick specimens is 9mm and that of regular specimens is 6mm
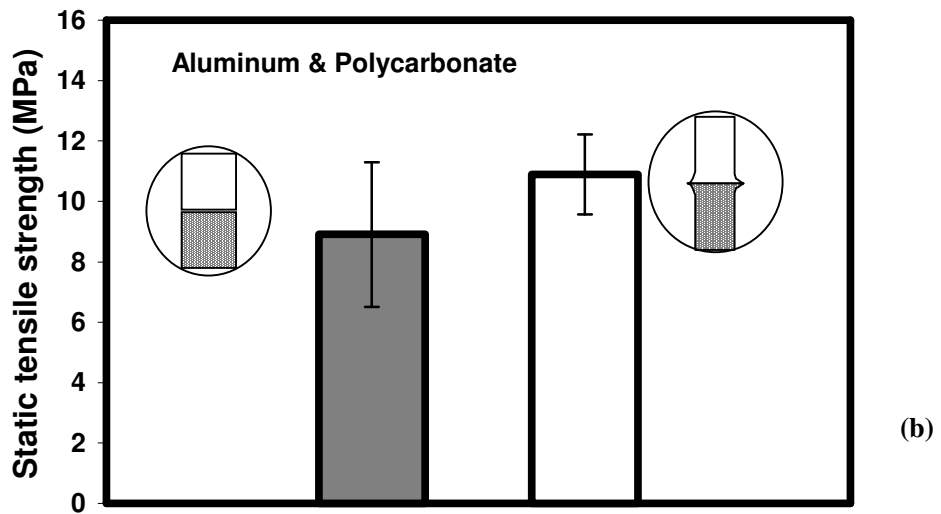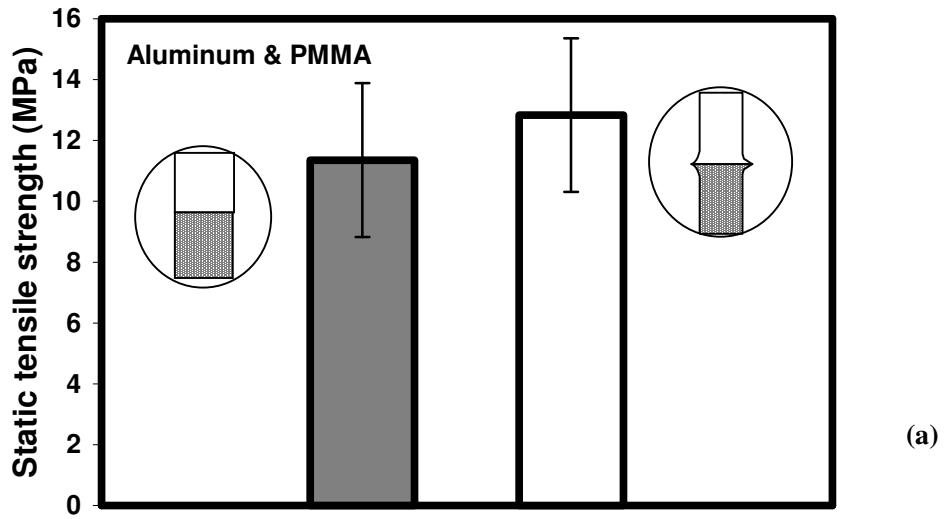
Figure 4.5, Bar charts depicting comparison of measured nominal static tensile strengths for baseline and convex shaped specimens: (a) aluminum/PMMA joints; (b) aluminum/polycarbonate joints.
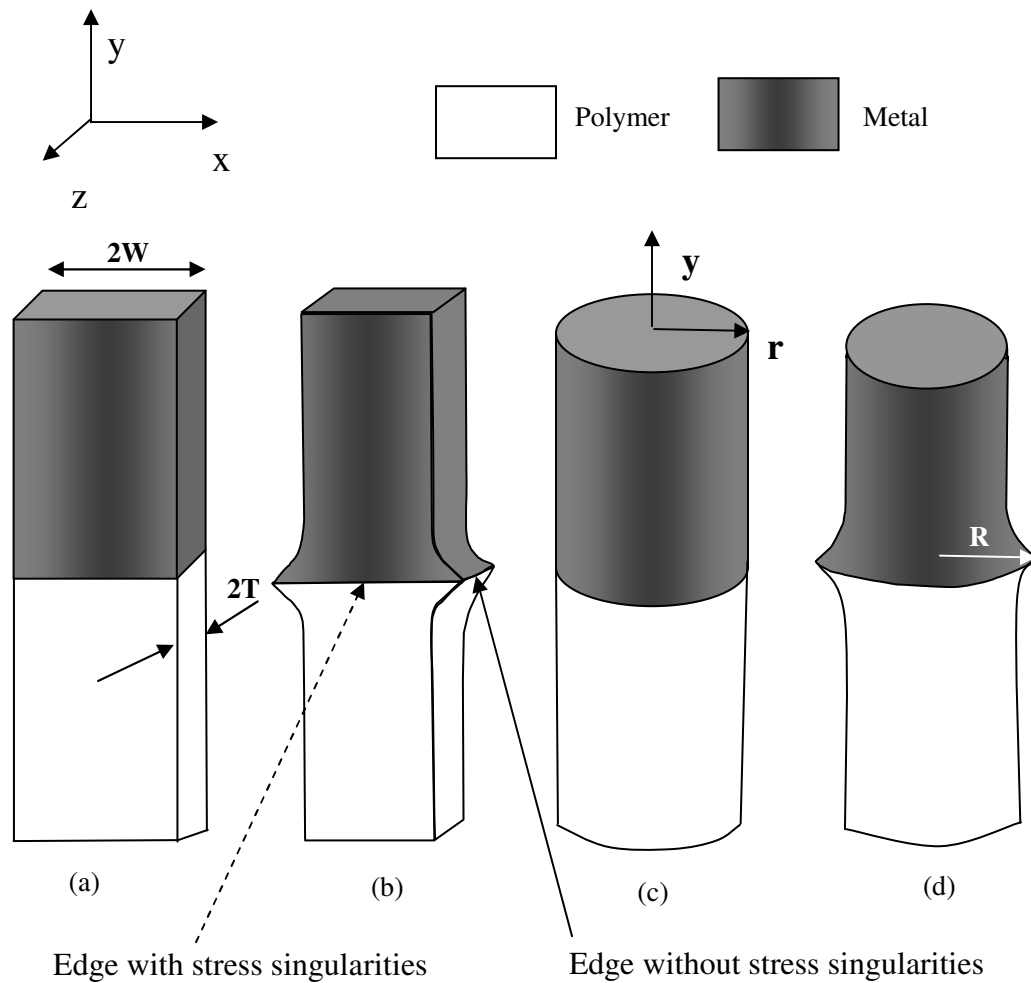
Figure 4.6, Schematic diagrams of metal-polymer joint specimens with (a) straight edges (baseline); (b) convex edges with least stress singularities; (c) axisymmetric straight joints (baseline); (d) axisymmetric convex joints with least stress singularities.

Dynamic test results

Four sets of dynamic specimens were prepared and each set had five specimens. Preliminary tests on axisymmetric straight and convex aluminum/polycarbonate joint specimens were conducted for system calibration and adjustment. Post-experiment

inspection clearly showed that failure of both straight and convex joints occurred at the interfaces. We did not measure the failure strengths of aluminum/polycarbonate joints since their transmitted pulse was very weak.   So only the data of axisymmetric straight and convex aluminum/PMMA joint specimens were recorded. The final test results of aluminum/PMMA joints are listed in Table 4.3 and illustrated in Figure 4.7. The average dynamic interfacial strengths of the straight and convex aluminum/PMMA joints are 25.64 MPa and 30.15MPa, much higher than their static counterparts due to the strain rate effect. With the same cross sectional area of different joint interfaces, the nominal interfacial strength of the convex joint increases by 17.59% over that of the straight joint, whereas its total material volume is reduced. These results indicate that the convex joint is also more efficient than the straight joint subjected to dynamic loading.

Table 4.3. Dynamic tensile test data of aluminum/PMMA joints (Interface area: 49.6mm^2)

| Joint angles (metal-polymer)	Dynamic tensile strength (MPa)	Change of strength	Standard deviation (MPa)
90^0-90^0 (baseline)	25.64	0%	4.77
65^0-45^0	30.15	+17.59%	5.71
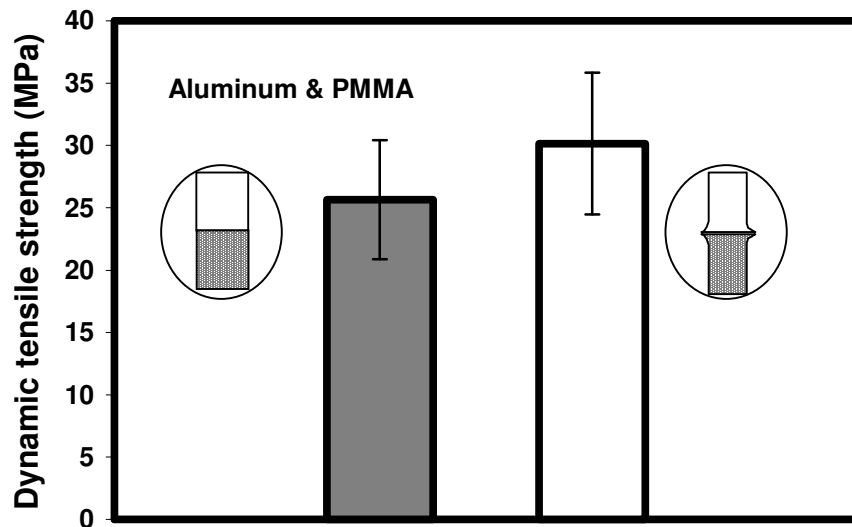
Figure 4.7, Bar charts depicting comparison of measured nominal dynamic tensile strengths for baseline and convex-shaped aluminum/PMMA joints.

Numerical simulations

Although experimental results show a significant increase in interfacial strengths of convex axisymmetric specimens, we are not sure that the free-edge stress singularities are removed without further analysis. Hence, numerical simulation is employed and the results are shown in Figures 4.8 and 4.9. As shown in Figure 4.6(c), y represents the axisymmetric axis, r refers to the location along the radius direction, and R is the radius of the joint interface. Also, σ_{app} denotes applied load and σ_{yy} is the interfacial normal stress.
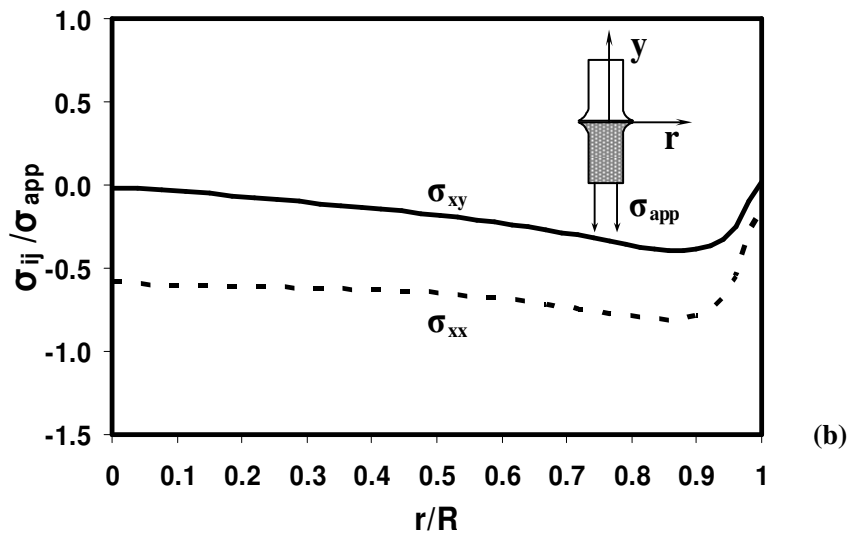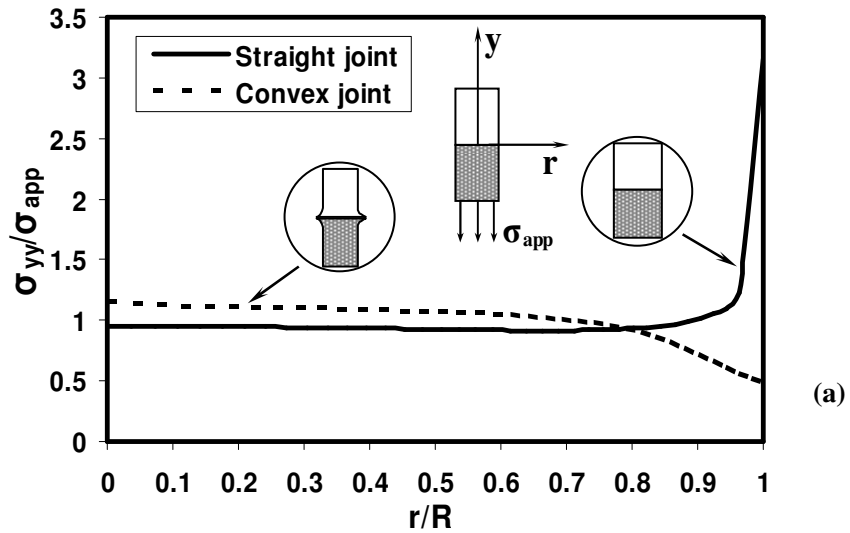
Figure 4.8, (a) Variations of the normalized stress component σ_{yy} for different joint types with the distance from specimen center; (b) Variations of the other normalized σ_{ij} of convex joints with the distance from specimen center.
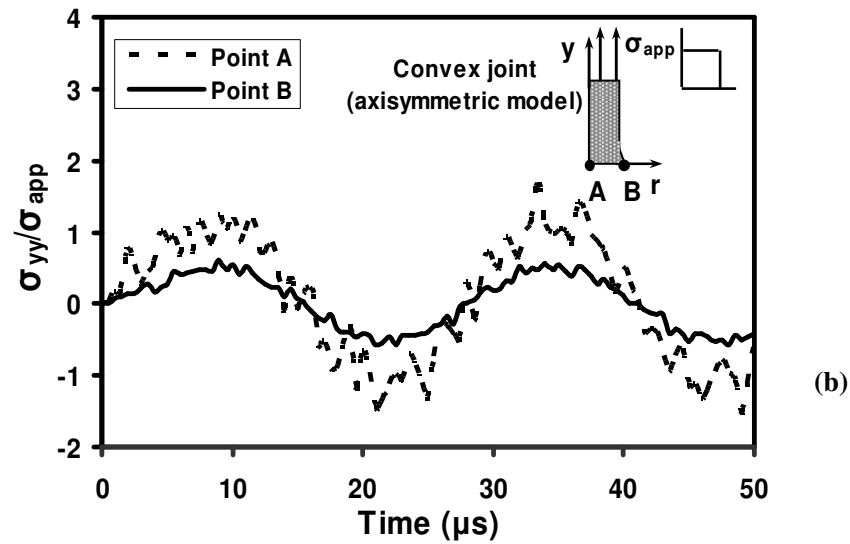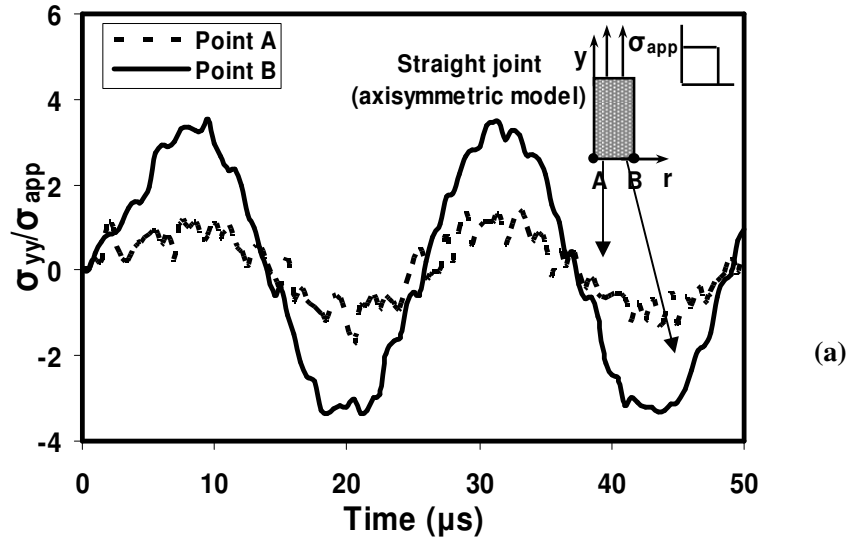
Figure 4.9, Comparison of stress history at the central point A and the edge point B for different joint types subjected to dynamic loading: (a) straight joints; (b) convex joints.

For tensile experiments, σ_{yy} is the critical stress component to cause interfacial failure. For different joint types under quasi-static loading, variations of the normalized σ_{yy} over external load σ_{app} with the distance from the interface center are shown in Figure 4.8(a). It is noticed that when r/R is in the range of 0.0-0.8, away from the free edges, the normal stress distribution is pretty uniform for both straight and convex joints. As r/R approaches one, the normal stress distribution becomes totally different for the two joint configurations. For straight-edged joints, σ_{yy} increases sharply and tends to infinity due to the free-edge stress singularity. However, for convex-shaped joints, the interfacial normal stress σ_{yy} decreases smoothly and reaches a finite value when r/R approaches one. The variations of other interfacial stress components of the convex joint are shown in Figure 4.8(b). All other stress components approach zero when r/R approaches one. The stress distribution change verifies the efficiency of the new convex joint in removing free-edge stress singularities. As a result, the convex joint could provide a reasonable way to accurately measure the intrinsic interfacial strengths of dissimilar materials. Secondly, the convex joint leads to higher load transfer capability with lower material volumes.

Dynamic stress analysis was also conducted for both straight and convex aluminum/PMMA joints. Under external dynamic loading, stress history of the central point A and the edge point B at the joint interface is shown in Figure 4.9. For straight-edged joints, the magnitude of the normalized stress component σ_{yy} at the edge point B is much larger than that at the central point A (see Figure 4.9(a)). These results indicate that high stresses develop at straight-edged joints, which theoretically result from

the free-edge stress singularity. However, as seen in Figure 4.9(b), for convex joints, the stress magnitude at the edge point B is less than that at the central point A, and compared to Figure 4.9(a), it is also less than the stress magnitude at the edge point B in straight-edged joints. Hence, the joint shape change leads to stress re-distributions at the joint interfaces so more uniform stress distribution is achieved at the interface. These results further explain the increase in dynamic interfacial strengths of convex joints.

CHAPTER V

SUMMARY

In the dynamic fracture mechanics analysis of failure mode transitions along weak interfaces, we make use of fitted dynamic stress intensity factors and the nonsingular T stresses of the incident cracks to obtain the stress intensity factors of the kinked cracks as functions of kinking angles and crack tip speeds. The T-stress of the incident crack has a small positive value but the crack path is still quite stable. In order to validate fracture mechanics predictions, the theoretical photoelasticity fringe patterns of the kinked cracks were compared with the recorded experimental fringes. Moreover, the mode-mixity of the kinked interfacial crack was found to depend on the kinking angle and the crack tip speed. A weak interface (interfacial strength or fracture toughness much less than that of the bulk material) will lead to a high mode-II component and a fast crack tip speed of the kinked mixed-mode crack.

Dynamic "Cook-Gordon mechanism" is also investigated experimentally and analytically in this work. After providing experimental evidence of interface debonding ahead of an incident dynamic crack, strength-based criteria are used to predict interfacial debonding initiation. Results indicate that a high stress intensity factor of the incident crack can easily cause interfacial debonding initiation, and a negative T stress can suppress interfacial debonding initiation. Moreover, interfacial tensile strength is much

more important than interfacial shear strength in controlling dynamic interfacial debonding initiation induced by a mode-I incident crack.

Since interface strengths play crucial roles in dynamic interface debonding initiation. In order to measure accurate interfacial strengths, we designed axisymmetric convex specimens of dissimilar material joints to eliminate free-edge stress singularities. An integrated experimental and numerical investigation shows that the axisymmetric convex joint not only produces more accurate interfacial strength measurements, but also improves the ultimate tensile load capacity of hybrid joints subjected to both static and dynamic loading. Meanwhile the material volume of the convex interfacial joint is reduced at least 18%.

APPENDIX

Functions $\Sigma_{ij}^{I}(\theta,v)$ that represent the angular variation of stress components for an instantaneous crack tip speed v are given by Freund (1990):

$$\Sigma_{11}^{I} = \frac{1}{D}\left\{(1+\alpha_s^2)(1+2\alpha_d^2-\alpha_s^2)\frac{\cos\frac{1}{2}\theta_d}{\sqrt{\gamma_d}} - 4\alpha_s\alpha_d\frac{\cos\frac{1}{2}\theta_s}{\sqrt{\gamma_s}}\right\} \tag{A1}$$

$$\Sigma_{12}^{I} = \frac{2\alpha_d(1+\alpha_s^2)}{D}\left\{\frac{\sin\frac{1}{2}\theta_d}{\sqrt{\gamma_d}} - \frac{\sin\frac{1}{2}\theta_s}{\sqrt{\gamma_s}}\right\} \tag{A2}$$

$$\Sigma_{22}^{I} = -\frac{1}{D}\left\{(1+\alpha_s^2)^2\frac{\cos\frac{1}{2}\theta_d}{\sqrt{\gamma_d}} - 4\alpha_s\alpha_d\frac{\cos\frac{1}{2}\theta_s}{\sqrt{\gamma_s}}\right\} \tag{A3}$$

where

$$\gamma_d = \sqrt{1-(v\sin\theta/c_d)^2}, \tan\theta_d = \alpha_d\tan\theta, \tag{A4}$$

$$\gamma_s = \sqrt{1-(v\sin\theta/c_s)^2}, \tan\theta_s = \alpha_s\tan\theta, \tag{A5}$$

$$D = 4\alpha_s\alpha_d - (1+\alpha_s^2)^2 \tag{A6}$$

$$\alpha_s = \sqrt{1-(v/c_s)^2}, \alpha_d = \sqrt{1-(v/c_d)^2}, \tag{A7}$$

$$c_s = \sqrt{\frac{\mu}{\rho}}, c_d = \sqrt{\frac{\kappa+1}{\kappa-1}}c_s, \tag{A8}$$

$$\kappa = \begin{cases} = 3-4\upsilon & \text{(plane strain)} \\ = \dfrac{3-\upsilon}{1+\upsilon} & \text{(plane stress)} \end{cases} \tag{A9}$$

where c_s and c_d are the shear wave and dilatational wave speeds of the material.

Similarly,

$$\Sigma_{11}^{II} = -\frac{2\alpha_s}{D}\left\{(1 + 2\alpha_d^2 - \alpha_s^2)\frac{\sin\frac{\theta_d}{2}}{\sqrt{\gamma_d}} - (1 + \alpha_s^2)\frac{\sin\frac{\theta_s}{2}}{\sqrt{\gamma_s}}\right\} \tag{A10}$$

$$\Sigma_{12}^{II} = \frac{1}{D}\left\{4\alpha_s\alpha_d\frac{\cos\frac{\theta_d}{2}}{\sqrt{\gamma_d}} - (1 + \alpha_s^2)^2\frac{\cos\frac{\theta_s}{2}}{\sqrt{\gamma_s}}\right\} \tag{A11}$$

$$\Sigma_{22}^{II} = \frac{2\alpha_s(1 + \alpha_s^2)}{D}\left\{\frac{\sin\frac{\theta_d}{2}}{\sqrt{\gamma_d}} - \frac{\sin\frac{\theta_s}{2}}{\sqrt{\gamma_s}}\right\} \tag{A12}$$

REFERENCE

Ahn, B.K., Curtin, W.A., Parthasarathy, T.A., and Dutton, R.E., 1998. Criterion for crack deflection/penetration for fiber-reinforced ceramic matrix composites. Composite Science and Technology, 58, 1775-1784.

Akisanya, A.R., and Fleck, N.A., 1997. Interfacial cracking from the free edge of a long bi-material strip. International Journal of Solids and Structures, 34, 1645-1665.

Akisanya, A.R., and Meng, C.S., 2003. Initiation of fracture at the interface corner of bi-material joints. Journal of the Mechanics and Physics of Solids, 51, 27-46.

Akisanya, A.R., and Meng, C.S., 2003. Initiation of fracture at the interface corner of bi-material joints. Journal of the Mechanics and Physics of Solids, 51, 27-46.

Anderson, T.L., 1995. Fracture Mechanics 2nd ed., CRC Press, Boca Raton.

Arata, J.J.M., Needleman, A., Kumar, K.S., and Curtin, W.A., 2000. Microcrack nucleation and growth in elastic lamellar solids. International Journal of Fracture, 105, 321-342.

Azhdari, A., and Nemat-Nasser, S., 1996. Energy-release rate and crack kinking in anisotropic brittle solids. Journal of the Mechanics and Physics of Solids, 44, 929-951.

Barber, A.H., Wiesel, E., and Wagner, H.D., 2002. Crack deflection at a transcrystalline junction. Composites Science and Technology, 62, 1957-1964.

Becker Jr., T.L., Cannon, R.M., and Ritchie, R.O., 2001. Finite crack kinking and T-stresses in functionally graded materials. International Journal of Solids and Structures, 38, 5545-5563.

Bogy, D.B., 1971. Two edge-bonded elastic wedges of different materials and wedge angles under surface tractions. Journal of Applied Mechanics, 38, 377-386.

Broberg, K.B., 1999. Cracks and Fracture, Academic Press, San Diego.

Chalivendra, V., and Rosakis, A. J., 2004. Private communication, Caltech.

Chao Y.J., Liu, S., and Broviak, B. J., 2001. Brittle fracture: variation of fracture toughness with constraint and curving under mode I conditions. Experimental Mechanics, 41, 232-241.

Chen, B., and Dillard, D.A., 2001. The effect of T stress on crack path selection in adhesively bonded joints. International Journal of Adhesion & Adhesives, 21, 357-368.

Chen, C.S., Krause, R., Pettit, R.G., Banks-Sills, L., and Ingraffea, A.R., 2001. Numerical assessment of T stress computation using p-version finite element method. International Journal of Fracture, 107, 177-199.

Chen, W., Subhash, G., and Ravichandran, G., 1994. Evaluation of ceramic specimen geometries used in split Hopkinson pressure bar. DYMAT Journal, 1, 193-210.

Chen, W., Lu, F., and Cheng, M., 2002. Tension and compression tests of two polymers under quasi-static and dynamic loading. Polymer Testing, 21, 113-121.

Chue, C.H., and Liu, C.I., 2002. Disappearance of free-edge stress singularity in composite laminates. Composite Structures, 56, 111-129.

Cook, J., and Gordon, J.E., 1964. A mechanism for the control of crack propagation in all brittle systems. Proc. Roy. Soc., 282A, 508-520.

Cotterell, B., and Rice, J.R., 1980. Slightly curved or kinked cracks. International Journal of Fracture, 16 (2), 155-169.

Dally, J.W., 1979. Dynamic photoelastic studies of fracture. Experimental Mechanics, 19, 349-61.

Davis, J.B., Kristoffersson, A., Carlstrom, E., and Clegg, W.J., 2000. Fabrication and crack deflection in ceramic laminates with porous interlayers. Journal of the American Ceramic Society, 83, 2369-2374.

Deng, X., 1994. An asymptotic analysis of stationary and moving cracks with frictional contact along bimaterial interfaces and in homogeneous solids. International Journal of Solids and Structures, 31, 2407-2429.

Dundurs, J., 1969. Discussion of edge-bonded dissimilar orthogonal elastic wedges under normal and shear loading by Bogy D.B.. ASME, Journal of Applied Mechanics, 36, 650-652.

Evans, A.G., and Zok, F.W., 1994. Review the physics and mechanics of fiber-reinforced brittle matrix composites.   Journal of Material Science, 29, 3857-3896.

Freund, L.B., 1990. Dynamic Fracture Mechanics, Cambridge University Press, New York.

Gama, B.A., Lopatnikov, S.L., and Gillespie, J.W.Jr., 2004. Hopkinson bar experimental technique: a critical review. Applied Mechanics Reviews, 57, 223-250.

Gao, H., and Chiu, C.H., 1992, Slightly curved or kinked cracks in anisotropic elastic solids. International Journal of Solids and Structures, 29, 947-972.

Gao, H., 1993. Surface roughness and branching instabilities in dynamic fracture, Journal of the Mechanics and Physics of Solid, 41, 457-486.

Gao, H., Huang, Y., Gumbsch, P., and Rosakis, A.J., 1999. On radiation-free transonic motion of cracks and dislocations.   Journal of the Mechanics and Physics of Solids, 47, 1941-1961.

Geubelle, P. H., and Kubair, D., 2001.   Intersonic crack propagation in homogeneous media under shear-dominated loading: numerical analysis.   Journal of the Mechanics and Physics of Solids, 49, 571-587.

Gilat, A., and Cheng, C.S., 2000. Torsional split Hopkinson bar tests at strain rates above 10(4)s(-1). Experimental Mechanics, 40, 54-59.

Guduru, P., Zehnder, A.T., Rosakis, A.J., and Ravichandran, G., 2001. Dynamic full-field measurements of crack tip temperatures. Engineering Fracture Mechanics, 68, 1535-1556.

Gupta, V., Argon, A.S., and Suo, Z., 1992. Crack deflection at an interface between two orthotropic materials.   Journal of Applied Mechanics, 59, s79-s87.

He, M.Y., Hsueh, C.H., and Becher, P.F., 2000. Deflection versus penetration of a wedge-loaded crack: effect of branch-crack length and penetrated-layer width. Composites Part B: Engineering, 31, 299-308.

He, M-Y., and Hutchinson, J.W., 1989. Crack deflection at an interface between dissimilar elastic materials. International Journal of Solids and Structures, 25, 1053-1067.

Hein, V.L., and Erdogan, F., 1971. Stress singularities in a two-material wedge. International Journal of Fracture Mechanics, 7, 317-330.

Huh, H., Kang, W.J., and Han, S.S., 2002. A tension split Hopkinson bar for investigating the dynamic behavior of sheet metals. Experimental Mechanics, 42, 8-17.

Hutchinson, J.W., and Suo, Z., 1992. Mixed mode cracking in layered materials. Advances in Applied Mechanics, 29, 63-191.

Jayadevan, K.R., Narasimhan, R., Ramamurthy, T.S., and Dattaguru, B., 2001. A numerical study of T-stress in dynamically loaded fracture specimens. International Journal of Solids and Structures, 38, 4987-5005.

Kalthoff, J.F., 1983.   On some current problems in experimental fracture. Workshop on dynamic fracture, W. G. Knauss, K. Ravi-Chandar, A. J. Rosakis ed., Pasadena. Caltech SM Report 83-12. 11-35.

Kerans, R.J., and Parthasarathy, T.A., 1999. Crack deflection in ceramic composites and fiber coating design criteria. Composites Part A: Applied Science and Manufacturing, 30, 521-524.

Kimberley J., and Lambros, J., 2004. Dynamic crack kinking from a PMMA/homalite interface. Experimental Mechanics, 44, 158-166.

Kobayashi, A.S. (ed.), 1987. Handbook on Experimental Mechanics, Society of Experimental Mechanics, Inc. Prentice-Hall, New Jersey.

Kobayashi, A.S., and Mall, S., 1978. Dynamic fracture toughness of homalite-100. Experimental Mechanics, 18, 11-18.

Korsunsky, A.M., 2001. Debonding of a weak interface in front of a through-thickness crack. International Journal of Fracture, 109, 35-40.

Kovar, D., King, B.H., Trice, R.W., and Halloran, J.W., 1997. Fibrous monolithic ceramics. Journal of the American Ceramic Society, 80, 2471-2487.

Lee, O.S., and Knauss, W.G., 1989. Dynamic crack propagation along a weakly bonded planes in a polymer. Experimental Mechanics, 29, 342-345.

Lee, O.S., Lee, J.Y., and Kim, G.H., 2000. High strain-rate deformation of composite materials using a split Hopkinson bar technique. Key Engineering Materials, 183, 307-312.

Lee, W., Howard, S.J., and Clegg, W.J., 1996. Growth of interface defects and its effect on crack deflection and toughening criteria. Acta Materialia, 44, 3905-3922.

Lee, W., Yoo, Y-H., and Shin, H., 2004. Reconsideration of crack deflection at planar interfaces in layered systems. Composites Science and Technology, 64, 2415-2423.

Lee, O.S., and Knauss, W.G., 1989. Dynamic crack propagation along a weakly bonded planes in a polymer. Experimental Mechanics, 29, 342-345.

Leevers, P.S., and Radon, J.C., 1982. Inherent stress biaxiality in various fracture specimen geometries. International Journal of Fracture, 19,311-325.

Leguillon, D., Lacroix, C., and Martin, E., 2000. Interface debonding ahead of a primary crack. Journal of the Mechanics and Physics of Solids, 48, 2137-2161.

Leguillon, D., Lacroix, C., and Martin, E., 2001. Crack deflection by an interface – asymptotic of the residual thermal stresses. International Journal of Solids and Structures, 38, 7423-7445.

Li, X-F., and Xu, L.R., 2006. T stresses across static crack kinking. ASME Journal of Applied Mechanics, in press.

Li, Z., Bi, X., Lambros, L., and Geubelle, P.H., 2002. Dynamic fiber debonding and frictional push-out in model composite systems: experimental observations. Experimental Mechanics, 42, 417-425.

Liu, C., Lambros, J., and Rosakis, A.J., 1993. Highly transient crack growth in a bimaterial interface: Higher order asymptotic analysis and optical experiments. Journal of the Mechanics and Physics of Solids, 41(12), 1887-1954.

Maleski, M.J., Kirugulige, M.S., and Tippur, H.V., 2004. A method for measuring mode I crack tip constraint under static and dynamic loading conditions. Experimental Mechanics, 44, 522-532.

Majumdar, B.S., Gundel, D.B., Dutton, R.E., Warrier, S.G., and Pagano, N.J., 1998. Evaluation of the tensile interface strength in brittle matrix composite systems. Journal of the American Ceramic Society, 81, 1600-1610.

Martin, E., Leguillon, D., and Lacroix, C., 2001. A revisited criterion for crack deflection at an interface in a brittle material. Composites Science and Technology, 61, 1671-1679.

Martin, E., Peters, P.W.M., Leguillon, D., and Quenisset, J.M., 1998. Conditions for matrix crack deflection at an interface in ceramic matrix composites. Materials Sciences and Engineering, A250, 291-302.

Martinez, D., and Gupta, V., 1994. Energy criterion for crack deflection at an interface between two orthotropic media. Journal of the Mechanics and Physics of Solids, 42(8), 1247-1271.

Melin, S., 2002. The influence of the T-Stress on the directional stability of cracks. International Journal of Fracture, 114,259-265.

Meyers, M.A., 1994. Dynamic behavior of materials. John Wiley, New York.

Munz, D., and Yang, Y.Y., 1993. Stresses near the edge of bonded dissimilar materials described by two stress intensity factors. International Journal of Fracture, 60, 169-177.

Pagano, J.J., 1998. On the micromechanical failure modes in a class of ideal brittle matrix composites: Part I- coated-fiber composites. Composites Part B, 29, 93-119.

Pageau, S.S., Gadi, K.S., Biggers, S.B., and Joseph, P.F., 1996. Standardized complex and logarithmic eigensolutions for n-material wedges and junctions. International Journal of Fracture, 77, 51-76.

Paulino, G.H., and Kim, J-H., 2004. A new approach to compute T stress in functionally graded materials by means of the interaction integral method. Engineering Fracture Mechanics, 71, 1907-1950.

Prakash, O., Sarkar, P., and Nicholson, P.S., 1995. Crack deflection in ceramic/ceramic laminates with strong interfaces. Journal of the American Ceramic Society, 78 (4): 1125-1127.

Qin, Q.H., and Zhang, X., 2000. Crack deflection at an interface between dissimilar piezoelectric materials. International Journal of Fracture, 102, 355-370.

Ravichandran, G., and Subhash, G., 1994. Critical appraisal of limiting strain rates for compression testing of ceramics in a split Hopkinson pressure bar. Journal of the American Ceramic Society, 77, 263-267.

Ravi-chandar, K., Lu, J., Yang, B., and Zhu, Z., 2000. Failure mode transitions in polymers under high strain rate loading. International Journal of Fracture, 101, 33–72,

Ramulu, M., & Kobayashi, A. S., 1985. Mechanics of crack curving and branching ---a dynamic fracture analysis. International Journal of Fracture, 27,187-201.

Reedy, E.D. Jr., and Guess, T.R., 1993. Comparison of butt tensile strength data with interface corner stress intensity factor prediction. International Journal of Solids and Structures, 30, 2929-2936

Rice, J.R., 1974. Limitations to small-scale yielding approximation for crack tip plasticity. Journal of the Mechanics and Physics of Solids, 22, 17-26.

Richardson, D.E., and Goree, J.G., 1993. Experimental verification of a new two parameter fracture model. Fracture Mechanics: Twenty-third Symposium. ASTM STP 1189, 738-750.

Roe, K.L., and Siegmund, T., 2003. An irreversible cohesive zone model for interface fatigue crack growth simulation. Engineering Fracture Mechanics, 70, 209-232.

Roham, S., Hardikar, K., and Woytowitz, P., 2004. Crack penetration and deflection at a bimaterial interface in a four-point bend test. Journal of Materials Research, 19, 3019-3027.

Rosakis, A.J., and Ravi-Chandar, K. 1986. On crack-tip stress state: An experimental evaluation of three-dimensional effects. International Journal of Solids and Structures, 22, 121-134.

Rosakis, A.J., Samudrala, O., and Coker, D., 1999. Cracks faster than shear wave speed. Science, 284, 1337-1340.

Rosakis, A. J., Samudrala, O., Singh, R. P. and Shukla, A., 1998. Intersonic crack propagation in bimaterial systems. Journal of the Mechanics and Physics of Solids, 46, 1789-1813.

Rousseau, C-E., and Rosakis, A. J., 2003. On the influence of fault bends on the growth of Sub-Rayleigh and intersonic dynamic shear ruptures. Journal of Geophysical Research, 108, 2411-2431.

Roychowdhury, S., Roy, Y., and Dodds, R.H. Jr., 2002. Ductile tearing in thin aluminum panels: experiments and analyses using large displacement, 3-D surface cohesive elements. Engineering Fracture Mechanics, 69, 983-1002.

Sanford, R.J., and Dally, J.W., 1979. A general method for determining mixed-mode stress intensity factors from isochromatic fringe patterns. Engineering Fracture Mechanics, 11, 621-633.

Selvarathinam, A.S., and Goree, J.G., 1998. T-stress based fracture model for cracks in isotropic materials. Engineering Fracture Mechanics, 60, 543-561.

Siegmund, T., Fleck, N.A., and Needleman, A., 1997. Dynamic crack growth across an interface. International Journal of Fracture, 85, 381-402.

Singh, R.P., Lambros, J., Shukla, A., and Rosakis, A.J., 1997. Investigation of the mechanics of intersonic crack propagation along a bimaterial interface using coherent gradient sensing and photoelasticity. Proceedings of the Royal Society of London, 453, 2649-2667.

Singh, R.P., and Shukla, A., 1996. Characterization of isochromatic fringe patterns for a dynamically propagating interface crack. International Journal of Fracture, 76, 293-310.

Swadener, J.G., Liechti, K.M., and de Lozanne, A.L., 1999. The intrinsic toughness and adhesion of a glass epoxy interface. Journal of the Mechanics and Physics of Solids, 47, 223-258.

Tandon, G.P., Kim, R.Y., Warrier, S.G., and Majumdar, B.S., 1999. Influence of free edge and corner singularities on interfacial normal strength: application in model unidirectional composites. Composites, Part B: Engineering, 30, 115-134.

Tippur, H.V., Krishnaswamy, S., Rosakis, A.J., 1991. A coherent gradient sensor for crack tip deformation measurements: analysis and experimental results. International Journal of Fracture, 48, 193-204.

Tvergaard, V., 2004. Predictions of mixed mode interface crack growth using a cohesive zone model for ductile fracture. Journal of the Mechanics and Physics of Solids, 52, 925-940.

Wang, H., and Ramesh, K.T., 2004. Dynamic strength and fragmentation of hot-pressed silicon carbide under uniaxial compression. Acta Materialia, 52, 355-367.

Wappling, D., Gunnars, J., and Stahle, P., 1998. Crack growth across a strength mismatched bi-material interface. International Journal of Fracture, 89, 223-243.

Warrier, S.G., Majumdar, B.S., and Miracle, D.B., 1997. Interface effects on crack deflection and bridging during fatigue crack growth of titanium matrix composites. Acta Materialia, 45, 4969-4980.

Washabaugh, P.G., and Knauss, W.G., 1994. A reconciliation of dynamic crack growth velocity and Rayleigh wave speed in isotropic brittle solids. International Journal of Fracture, 65, 97-114.

Williams, M.L., 1952. Stress singularities resulting from various boundary conditions in angular corners in extension. Journal of Applied Mechanics, 19, 526-528.

Williams, M.L., 1957. On the stress distribution at the base of a stationary crack. Journal of Applied Mechanics, 24, 109–114.

Xu., L. R., 2002. Ph.D. thesis, Graduate Aeronautical Laboratories, California Institute of Technology, Pasadena, CA.

Xu, L.R., Huang, Y.Y., and Rosakis, A.J., 2003. Dynamic crack deflection and penetration at interfaces in homogeneous materials: experimental studies and model predictions. Journal of the Mechanics and Physics of Solids, 51, 461-486.

Xu, L.R., and Rosakis, A.J., 2002. Impact failure characteristics in sandwich structures; Part I: basic failure mode selections, International Journal of Solids and Structures, 39, 4215-4235.

Xu, L.R., and Rosakis, A.J., 2002. Impact failure characteristics in sandwich structures; Part II: effects of impact speed and interfacial strength. International Journal of Solids and Structures, 39, 4237-4248.

Xu, L.R., and Rosakis, A.J., 2003. An experimental study of impact-induced failure events in homogeneous layered materials using dynamic photoelasticity and high-speed photography, Optics and Lasers in Engineering, 40, 263-288.

Xu, L.R., Rosakis, A.J., and Samudrala, O., 2002. Measurements of adhesive tensile and shear strengths with the aid of two optical techniques. Proceedings of the Society of Experimental Mechanics Annual Conference, San Diego, CA.

Xu, L.R., Kuai, H., and Sengupta, S., 2004(a). Dissimilar material joints with and without free-edge stress singularities: Part I. a biologically inspired design. Experimental Mechanics, 44,608-615.

Xu, L.R., and Sengupta, S., 2004(b). Dissimilar material joints with and without free-edge stress singularities: Part II. An integrated numerical analysis. Experimental Mechanics, 44, 616-621.

Xuan, W., Curtin, W. A., and Needleman, A., 2003. Stochastic microcrack nucleation in lamellar solids. Engineering Fracture Mechanics, 70, 1869-1884.

Yang, B., and Ravi-Chandar, K., 1999. Evaluation of elastic T-stress by the stress difference method. Engineering Fracture Mechanics, 64, 589-605.

Yang, L.M., and Shim, V.P.W., 2005. An analysis of stress uniformity in split Hopkinson bar test specimens. International Journal of Impact Engineering, 31, 129-150.

Yang, S., and Yuan, F.-G., 2000. Kinked crack in anisotropic bodies. International Journal of Solids and Structures, 37, 6635-6682.

Yokoyama, T., 2003. Experimental determination of impact tensile properties of adhesive butt joints with the split Hopkinson bar. Journal of Strain Analysis for Engineering Design, 38, 233-245.